# Folia Histochemica et Cytobiologica

Scientific quarterly devoted to problems of histochemistry, cytochemistry and cell & tissue biology

SC
SC

20 µm

Impact Factor:
1.698

VM
VIA MEDICA

# Folia Histochemica et Cytobiologica

Scientific quarterly devoted to problems of histochemistry, cytochemistry and cell & tissue biology

https://journals.viamedica.pl/folia_histochemica_cytobiologica

Vol. 59
No. 2
2021

## Official Journal of the Polish Society for Histochemistry and Cytochemistry

# POLISH SOCIETY FOR HISTOCHEMISTRY AND CYTOCHEMISTRY STATEMENT OF FOLIA HISTOCHEMICA ET CYTOBIOLOGICA EDITORIAL POLICY

Folia Histochemica et Cytobiologica is an international, English-language journal devoted to the rapidly developing fields of histochemistry, cytochemistry, cell and tissue biology.

The Folia Histochemica et Cytobiologica publishes papers that meet the needs and intellectual interests of medical professionals, basic scientists, college and university teachers and students. Prospective authors should read most recent issues of FHC to determine the appropriateness of a possible contribution. However, such an examination does not provide an infallible guide because editorial policy is always under review. Technical correctness is necessary, but it is not the only condition for acceptance. Clarity of exposition and potential interest of the readers are important considerations; it is the reader, not the author, who must receive the benefit of the doubt.

Folia Histochemica et Cytobiologica publishes review articles, original articles, short communications and proceedings of scientific congresses/symposia. Fields of particular interests include development and application of modern techniques in histochemistry and cell biology, cell biology and pathology, cell-microenvironment interactions, tissue organization and pathology.

Manuscripts announcing new theoretical or experimental results, or manuscripts questioning well-established and successful theories, are highly desirable and are a subject for evaluation by specialists. Manuscripts describing original research that clarifies past misunderstandings or allows a broader view of a subject are acceptable. Manuscripts that demonstrate new relations between apparently unrelated areas of fields of interests are appropriate. Manuscripts that show new ways of understanding, demonstrating, or deriving familiar results are also acceptable. Such manuscripts must provide some original cytobiological insight and not just a clever derivation.

Regularly, review or tutorial articles are published, often of a length greater than that of the average article. Most of these articles are a subject of a review; authors planning such articles are asked to consult with the editors at an early stage.

Most readers of a particular article will be specialists in the subject matter presented; the context within which the paper is presented should be established in the order given in Instructions for Authors. Manuscripts must be technically correct and must take proper cognizance of previous work on the same subject regardless of where it may have appeared. Such referencing is especially important for reminders of once well known ideas, proofs, or techniques that may have again become useful to readers. It is the responsibility of the author to provide adequate references; editors and referees will not do the literature search that should have been done by the authors. The references are a matter of review though.

Contributions considered include: Regular Articles (Papers), Short Communications, Review Articles, Conference Proceeding, Book Reviews and Technical Notes, which describe new laboratory methods or substantial improvements of the existing techniques. Regular articles should be about five journal pages or less in length. Short communications are usually confined to the discussion of a single concept and should be about two journal pages in length. Review articles are confined to a broad discussion and should contain the most recent knowledge about the subject.

Instructions concerning the preparation of manuscripts are given in the Information for Authors. Care in following those instructions will permit editors and referees to devote more time to thoughtful evaluation of contributions and will ultimately lead to a better, more interesting Journal.

Copying information, in part or in whole by any means is prohibited without a written permission from the owner.

Illustration on the cover: *Folliculo-stellate cells in the pars distalis of rat adenohypohysis were visualized by S-100 immunohistochemistry* (see: Omar A.I., Kamar S.S., pp. 95–107)

© Polish Society for Histochemistry and Cytochemistry

# Folia Histochemica
# et Cytobiologica

**Official Journal of the Polish Society for Histochemistry and Cytochemistry**

ORIGINAL PAPER

**VM**
**VIA MEDICA**

# Identification of circulating regulatory T lymphocytes with membrane markers — a new multiparameter flow cytometry protocol

**Agnieszka Piekarska[1]●, Michaël Pérès[2, 3]●, Magdalena Toton[4], Malgorzata Kulczycka[4], Krzysztof Lewandowski[5]●, François Vergez[2, 3]●**

[1]Department of Hematology and Transplantology, Medical University of Gdansk, Gdansk, Poland

[2]Cancer Research Center of Toulouse, Inserm UMR 1037, CNRS ERL 5294,
University of Toulouse, Oncopole, Toulouse, France

[3]Laboratoire de Génétique des Hémopathies, Institut Universitaire du Cancer Toulouse
— Oncopole, Toulouse, France

[4]Laboratory of Hematology, University Clinical Centre, Gdansk, Poland

[5]Department of Laboratory Medicine, Medical University of Gdansk, Gdansk, Poland

**Abstract**

**Introduction.** Regulatory T cells (Tregs) are a unique CD4$^+$ T cell subset involved in the regulation of immune responses. The traditional immunophenotype used to define Tregs includes CD4$^+$CD25$^{high}$ and the expression of the transcription factor Forkhead box protein 3 (FoxP3). A complex technique of intracellular staining, transient upregulation of FoxP3 in activated conventional T lymphocytes (Tcons), and the omission of naïve CD45RA$^+$ Tregs with downregulated FoxP3 activity but a demethylated *FOXP3* promoter region may lead to inaccurate quantification. In an attempt to meet the need for a reliable and simplified enumeration strategy, we investigated different membrane markers to capture the entire Treg compartment and to identify subpopulations of Tregs.
**Material and methods.** Analyses were performed on whole blood. Tested gating strategies were based on the expression of the following membrane antigens: CD45, CD3, CD4, CD25, CD127, CD26, CD6, CD39, CD71, HLA-DR, CD45RA and CD31. Double controls with FoxP3 were performed.
**Results.** The final enumeration panel consisted of the membrane markers CD45, CD3, CD4, CD25, CD127, CD26, CD39, CD45RA and CD31. A deep analysis of T cells with the CD4$^+$CD25$^+$CD127$^{low/-}$CD26$^{low/-}$CD45RA$^-$ immunophenotype revealed high expression of FoxP3 and/or CD39, while cells with the naïve immunophenotype, CD4$^+$CD25$^+$CD127$^{low/-}$CD26$^{low/-}$CD45RA$^+$, presented lower expression of suppressor markers. Antigen CD31 is considered to be a valuable membrane marker of thymus-derived Tregs.
**Conclusions.** The presented 9-color panel that can be easily applied in laboratories enables reliable enumeration of Tregs with additional information about the functionality, maturity and origin of T regulatory cells. *(Folia Histochemica et Cytobiologica 2021, Vol. 59, No. 2, 75–85)*

**Key words:** T regulatory cells; enumeration; flow cytometry; 9-color panel; CD31

**Correspondence address:** Agnieszka Piekarska, MD, PhD
Department of Hematology and Transplantology,
Medical University of Gdansk
Smoluchowskiego 17, 80–214 Gdansk, Poland
fax: +48 58 584 43 50
e-mail: agnieszka.piekarska@gumed.edu.pl

## Introduction

Regulatory T cells (Tregs) are a unique CD4$^+$ T cell subset involved in the regulation of immune responses. This subpopulation is fundamental for the development of immune tolerance after allogeneic hematopoietic cell transplantation (alloHCT) [1]. There are also many reports showing a correlation between clinical response to therapies applied in certain inflammatory conditions and increasing levels of circulating Tregs [2]. Extracorporeal photopheresis (ECP), offered to patients with graft-versus-host disease (GVHD) resistant to standard immunosuppressive therapy, is one of the best examples [3–5]. Among the complex mechanisms of immunomodulation promoted by ECP, the induction of Tregs seems to play a crucial role [6, 7]. In addition to the measurement of the clinical response to therapies influencing the expansion of Tregs, the evaluation of immunological status during treatment would give additional arguments for the maintenance or modification of immunosuppressive treatment [8–12]. Therefore, clinicians have highlighted the need for a reliable and accurate strategy for Treg enumeration and monitoring that can be applied in routine everyday practice [13].

The transcription factor Forkhead box protein 3 (FoxP3) is a traditional marker for the identification of Tregs with suppressor activity by flow cytometry. Given that FoxP3 is an intracellular molecule, its detection requires a complex technique of fixation and permeabilization, which may give inaccurate quantification owing to inevitable cell loss and reduced fluorescence of the antibody conjugates [14, 15]. DURAClone staining technology reduces pipetting errors and stabilization issues but it is not available in every laboratory [15, 16]. Moreover, flow cytometry may not be sensitive enough to detect all FoxP3 proteins, and activity below the level of detection is omitted. The results vary and may be difficult to compare among different laboratories or over time in the same laboratory. Moreover, quantification is imprecise because FoxP3 is transiently upregulated in activated effector T lymphocytes (conventional T cells; Tcons) [17]. CD127 antigen has been described as a surrogate marker of FoxP3 because there is an inverse correlation between CD127 and FoxP3 expression [16, 18]. However, it has also been demonstrated that T lymphocytes of phenotype CD25$^{high}$CD127$^{low/-}$ with FoxP3$^{low/-}$ are equally suppressive [19–21]. Additionally, naïve CD45RA$^+$ Tregs with downregulated FoxP3 activity have "hidden" but stable suppressor potential, as demonstrated by high levels of *FOXP3* mRNA and a demethylated *FOXP3* promoter region [22, 23]. Taking these data together, FoxP3 expression

is not always sufficient for the identification and enumeration of circulating functional Tregs in humans, and the expression of CD4$^+$CD25$^+$CD127$^{low/-}$ seems to be more accurate for this purpose [16, 24].

We aimed to investigate the membrane antigens that would give comparable and reliable enumeration of the entire Treg compartment and the identification of Treg functional subpopulations.

## Materials and methods

**Design of the marker molecules' panel.** The backbone panel contained antigens CD25 and CD127 and CD45RA, gated on CD45$^+$CD3$^+$CD4$^+$ cells. Antigens CD25 and CD127 are utilized to identify Tregs in many laboratories, but this simplified analysis seems to be insufficient [19, 20, 25]. Therefore, the tested panel was widened with the antigens CD26, CD6, CD39, CD31, and HLA-DR, and a double control with FOXP3, to better characterize the gated subgroups. The choice of CD26, CD6 and CD39 was justified because these specific surface markers were already tested for the isolation of Tregs by cell sorting, *e.g.*, for therapeutic purposes. The suppressor activity of those sorted cells was already validated [25–27]. The choice of antigens CD45RA and CD31 was designed to distinguish naïve Tregs from effector/memory Tregs, and thymus-derived (t)Tregs from induced, periphery-derived (p)Tregs [22, 28]. The expression levels of CD71 and HLA-DR were included as activation markers [29].

**Blood samples.** Twenty-one peripheral blood samples were collected from healthy volunteers into vacutainers with EDTA as an anticoagulant. The final panel was tested on blood samples from 10 patients treated for chronic GVHD after alloHCT. All analyses were performed on whole blood. The study was conducted in conformance with the latest Declaration of Helsinki ethical guidelines and was approved by the Bioethical Committee of the Medical University of Gdansk (decision number NKBBN/413/2016).

**Flow cytometry and sample analysis.** Samples comprising 200 $\mu$l of whole blood were incubated with the following antibodies/conjugates in various combinations depending on the staining protocol tested: CD3-BV421 (clone UCHT1), CD45-BV510 (clone H130) (both from BioLegend), CD4-PECy7 (clone SK3), CD25-PerCP Cy5.5 (clone M-A251) (both from Beckman-Coulter), CD26-FITC (clone M-A261), CD31-PE (clone WM59), CD39-PE-CF594 (clone TU66), CD39-PE-CF594 (clone TU66), CD39-APC (clone TU66), CD6-Alexa Fluor 647 (clone M-T605), CD45RA-Alexa Fluor 700 (clone HI100), CD127-APC-H7 (clone R3434), and CD3 Pacific Blue (clone UCRH1) (all from BD Biosciences). Incubation was followed by cell lysis with a solution of ammonium chloride and two washes
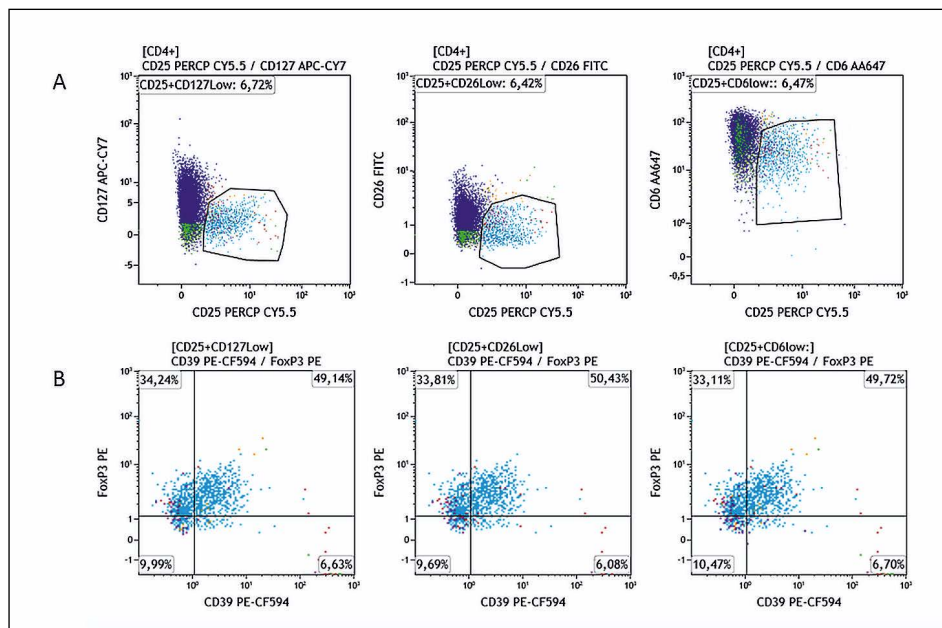
**Figure 1.** Comparison of three dot plots for initial Treg gating. **A.** Presentation of initial gating based on the CD25 expression and one of three negative Treg-associated markers (CD127 or CD26 or CD6); **B.** FoxP3 and CD39 expression of cells gated on CD25-positivity and negative Treg-associated markers (CD127 or CD26 or CD6)

before cell resuspension. Specimens with membrane staining proceeded to the acquisition step. Samples requiring intracellular staining were fixed and permeabilized with Fix/Perm Buffer and washed with the Perm Buffer from a FoxP3 staining kit (eBioscience). Staining with FoxP3-PE (clone PCH101; eBioscience) was performed in Perm Buffer before cytometer acquisition.

For the data obtained at the University of Toulouse (Toulouse, France), cells were acquired on 10-color Navios (Beckman Coulter). For the data obtained at the Medical University of Gdansk (Gdansk, Poland), cell acquisition was performed on a Becton Dickinson 12-color BD FACSLyric™. Data were analyzed with the use of Kaluza software (version 2.1).

**Statistical analysis.** Statistical data (absolute counts and percentages of gated cells within the quadrants) obtained from Kaluza software were copied into spreadsheets. Descriptive statistics, medians, and ranges were calculated using Statistica version 13.1 (StatSoft).

## Results

### One positive marker (CD25) and one negative selection marker (CD127 or CD26 or CD6) enable comparable initial gating

As the first step, we gated potential Tregs using combinations of one positive marker CD25$^+$ and one of the tested negative markers, CD26$^{low/-}$ or CD127$^{low/-}$ or CD6$^{low/-}$, within the CD45$^+$CD3$^+$CD4$^+$

cells (Fig. 1A). The median percentage of gated cells was 5.6% (range 2.7–11%). The level of expression of FoxP3 and CD39 was used to test different initial gating strategies. The rates of FoxP3$^+$ and/ /or CD39$^+$ cells were 80.8%, 87.5% and 85.2% in gates CD127$^{low/-}$, CD26$^{low/-}$ and CD6$^{low/-}$, respectively (Fig. 1B). The differences were not significant. Therefore, we decided to use a backbone panel based on the expression of CD25 and CD127, which has been already validated and approved in many laboratories.

### Almost overlapping high fluorescence intensity of FoxP3 and CD39 within the subpopulation CD45RA$^-$

In the next analysis, we compared the fluorescence intensities of FoxP3 and CD39 within the gated potential Tregs with the positive or negative expression of CD45RA. Treg gating was based on the three tested initial gating strategies described above. We found a high percentage of FoxP3$^+$ (50.3%; range 34.2– 57.4%) and CD39$^+$ cells (53.1%; range 45.9–58.9%) within gated CD45RA$^-$ cells. A low percentage of CD45RA$^+$ cells demonstrated the expression of FoxP3 or CD39 (3%; range 0.3–10.6%). The rates differed depending on the gating strategy but the differences were not statistically significant (data not shown graphically). This finding was additional proof that a panel based on the expression of CD25 and CD127 was a suitable backbone for further tests.

### The CD26$^{int/high}$ population is more suitable than the CD6$^{int/high}$ population for the exclusion of contamination with Tcons

As the next step, we performed a comparison of additional membrane staining with anti-CD26 and anti-CD6 antibodies to eliminate cells with the CD26$^{int/high}$ or CD6$^{int/high}$ phenotype, representing the Tcons, from the final enumeration. The CD26$^{int/high}$ population appeared to be more evident to exclude undesired cells than the CD6$^{int/high}$ population owing to a clear cut-off of Tcons from the final count. Moreover, the percentage of FoxP3$^-$CD39$^-$ cells was higher (26% *vs.* 16%) in gating based on CD26 membrane expression suggesting more adequate elimination of Tcons. The graphical presentation of this comparative gating is presented in Figure 2.

### CD39 is a valuable marker to replace FoxP3

In most analyses, we compared the expression of CD39 with FoxP3. Among the gated highly suppressive cells (CD25$^+$CD127$^{low/-}$CD26$^{low/-}$CD45RA$^-$) expressing CD39$^+$, 90.9% were also FoxP3$^+$. Moreover, 92.3% of the cells were either CD39$^+$ or FoxP3$^+$. In contrast, CD45RA$^+$ cells were a small subset within the gated CD25$^+$CD127$^{low/-}$CD26$^{low/-}$ cells characterized by low expression of FoxP3$^+$ and/or CD39. One example of the histograms is presented in Figure 3.

### CD31 is a valuable marker of thymus-derived Tregs (tTregs)

The next step was to define the origin of Tregs by the membrane expression of CD31$^+$ (tTregs *vs.* peripheral Tregs with extrathymic origin; pTregs) and to check the state of activation.

A higher number of CD31$^+$ Tregs was detected within the compartment of the naïve immunophenotype identified by the positive expression of antigen CD45RA. Among the naïve CD45RA$^+$ Tregs, CD31$^+$ cells were predominantly represented by a subgroup lacking the expression of CD39 (median 39.1%). CD31$^+$CD39$^+$ cells were detected in 1.4% of gated CD45RA$^+$ Tregs. However, the median rates of CD31$^+$CD39$^-$ and CD31$^+$CD39$^+$ within the CD45RA$^-$ cells were comparable: 9.2 and 8.7%, respectively.

The expression of the activation marker CD71 was weak in unstimulated lymphocytes. Therefore, we decided to proceed with HLA-DR (the late activation marker) staining. This staining was more apparent within the effector CD45RA$^-$ Tregs. Among CD4$^+$CD25$^+$CD127$^{low/-}$CD45RA$^-$HLA-DR$^+$ effector Tregs, 95% were CD39$^+$ cells and none were CD31$^+$ cells, in contrast to naïve CD4$^+$CD25$^{int/high}$CD127$^{low/-}$CD45RA$^+$ Tregs, which were all HLA-DR negative, with 95% of cells being CD39$^-$ and 41%

being CD31$^+$. The graphical presentation is shown in Figure 4. Anti-HLA-DR staining was used to check the activation status of gated Treg subsets but was not used for the final enumeration panel to simplify the analysis.

### Gating strategy to enumerate circulating Tregs

Using a gating strategy based on lymphocytes, CD25$^+$CD127$^{low/-}$ *versus* CD25$^+$CD26$^{low/-}$, we captured a similar number of cells within CD45$^+$CD3$^+$CD4$^+$ cells: 5.4% (range 3.2–10.7%) and 5.6% (range 3.1–11%), respectively. Moreover, the numbers of cells that were CD45RA$^+$, CD45RA$^-$, CD39$^+$ and CD31$^+$ within the gated population were comparable. However, the final strategy to count the whole compartment of Tregs uses the CD26$^{low/-}$ population within CD25$^+$CD127$^{low/-}$, from the gated CD45$^+$CD3$^+$CD4$^+$ cells, to exclude accidental contamination with activated Tcons more precisely. Lymphocytes are gated on a CD45/SS dot plot, then CD4$^+$ T cells (CD3$^+$CD4$^+$ cells) are gated on a CD3/CD4 dot plot. Tregs are initially identified as CD25$^+$CD127$^{low/-}$ on a CD25/CD127 dot plot. The next step is to exclude cells with intermediate or high expression of CD26 that is very obvious on a CD45RA/CD26 dot plot (among CD25$^+$CD127$^{low/-}$). The cells detected after the elimination of CD26$^+$ cells are taken to calculate the total number of Tregs. This gate is also a first step to identify different Treg subsets: two quadratic gates should be placed to discriminate effector/memory (CD45RA$^-$CD26$^{low/-}$) and naïve Treg (CD45RA$^+$CD26$^{low/-}$) cells on a CD45RA/CD26 dot plot. The next step to better characterize Treg subsets is to check CD31 and CD39 expression within these two gates. The graphical presentation of the gating strategy for the enumeration panel is presented in Figure 5.

The presented rates of total Tregs and Treg subsets were calculated from CD4$^+$ T cells. The numbers of total Tregs and Treg subsets are expressed as the percentage of the lymphocyte gate from the CD45/SS cytogram. Absolute values were calculated by multiplying these percentages by the number of lymphocytes in a microliter of blood, determined on a hematology analyzer.

With the use of our gating protocol, the median absolute count was 66.4 (range 22.8–162.7) cells/$\mu$l. The median rate within CD4$^+$ and the median absolute count of Tregs expressing CD39 was 2.4% (range 1–8.7%) and 18.5 (1.7–84.5) cells/$\mu$l, respectively.

A trial analysis of the panel performed in 10 patients with a moderate or severe form of chronic GVHD (cGVHD) showed a lower median percentage within CD4$^+$ cells and absolute values of Tregs: 5.1% (range 2.1–15.8%) and 33.6 (range 15.3–91.5) cells/$\mu$l,
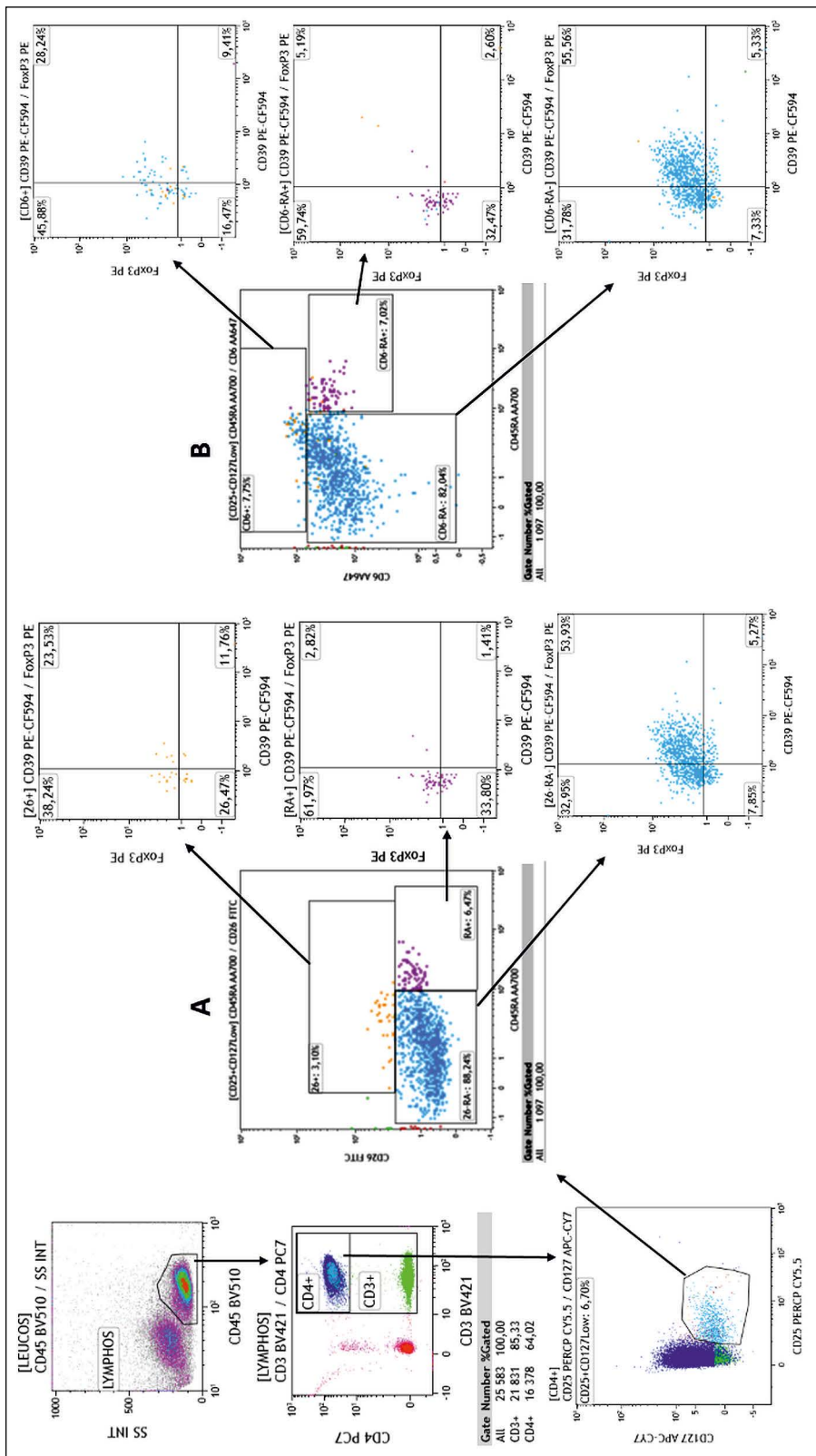
**Figure 2.** Comparison of two gating strategies based on the exclusion of CD26$^+$ or CD6$^+$ T-cells from the final Treg enumeration protocol. Lymphocytes are gated on a CD45/SS dot plot, then CD4$^+$ T cells (CD3$^+$CD4$^+$ cells) are gated on a CD3/CD4 dot plot. Tregs are initially identified as CD25$^+$CD127$^{low/-}$ on a CD25/CD127 dot plot. The next step is to exclude cells with intermediate or high expression of CD26 (**A**) on a CD45RA/CD26 dot plot (among CD25$^+$CD127$^{low/-}$) or with intermediate or high expression of CD6 (**B**) on a CD45RA/CD6 dot plot (among CD25$^+$CD127$^{low/-}$). The three quadratic gates represent the following: the upper gate includes Tcons by either high/intermediate expression of CD26 or CD6; the lower left includes memory/effector Tregs; and the lower right includes naïve Tregs. The comparative expression of CD31 and CD39 within these quadratic gates of two gating protocols is also provided.
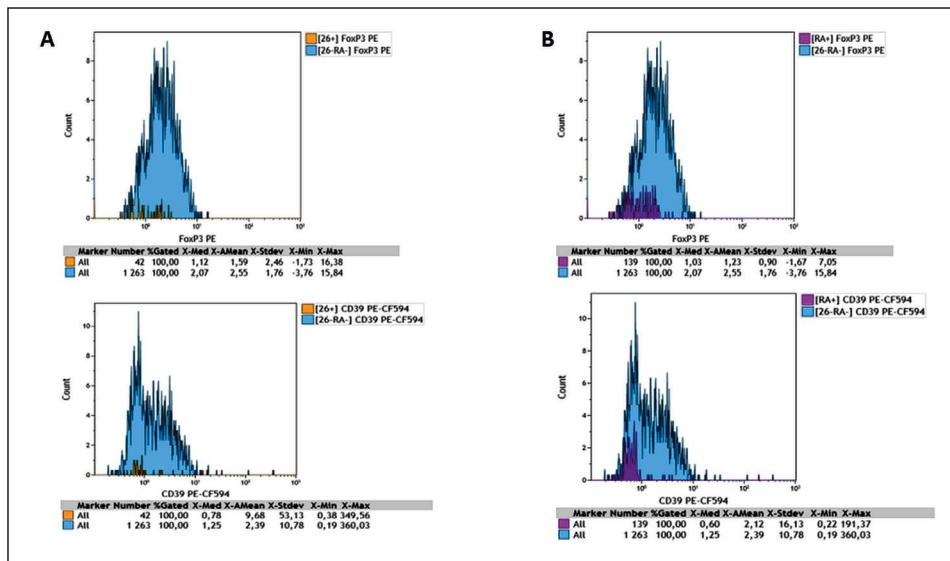
**Figure 3.** Comparison of FoxP3 and CD39 expression. **A.** Histograms showing comparable count of cells expressing FoxP3 and CD39 within a compartment of CD25$^+$CD127$^{low/-}$CD26$^{low/-}$CD45RA$^-$ (26-RA-) Tregs with a compartment of CD25$^+$CD127$^{low/-}$CD26$^{int/high}$CD45RA$^+$ (26+) T cons; **B.** Histograms showing comparable count of cells expressing FoxP3 and CD39 within a compartment of CD25$^+$CD127$^{low/-}$CD26$^{low/-}$CD45RA$^-$ (26-RA-) cells (memory/effector Tregs) with a compartment of CD25$^+$CD127$^{low/-}$CD26$^{low/-}$CD45RA$^+$ (RA+) cells (naïve Tregs).
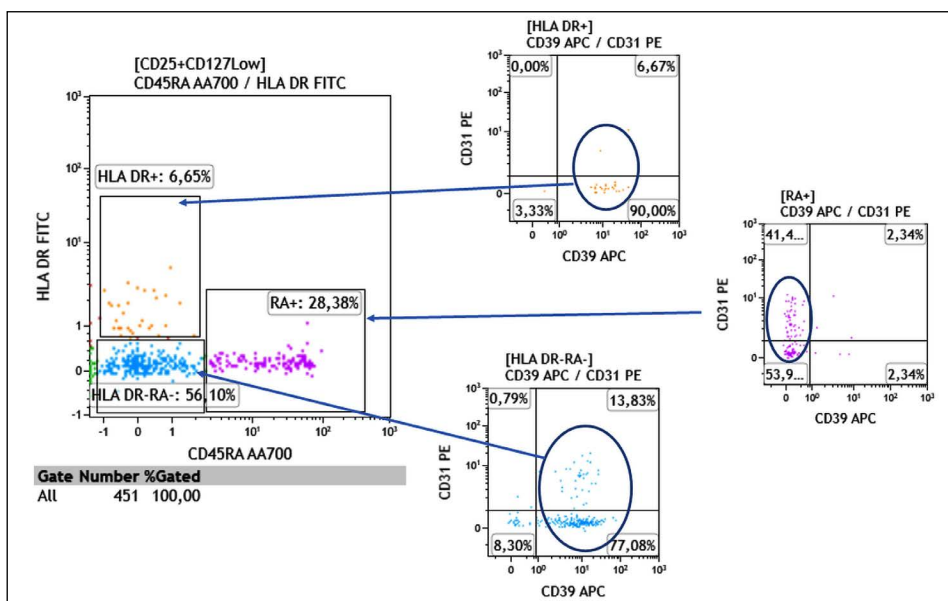


**Figure 4.** Expression of HLA-DR (the late activation marker) on Treg subsets. A left CD45RA/HLA-DR dot plot represents Tregs subsets gated from lymphocytes by the CD3$^+$CD4$^+$CD25$^+$CD127$^{low/-}$ immunophenotype. The three dot plots on the right present a comparison of CD31 and CD39 expression among naïve Tregs (CD45RA$^+$HLA-DR$^-$) and among effector//memory Tregs (CD45RA$^-$) with a positive late activation marker (HLA-DR$^+$) and with negative HLA-DR expression.

respectively. Differences between volunteers and the GVHD patients were especially visible in absolute values of Treg subsets. The summarized results for Tregs in healthy donors and patients with chronic GVHD are presented in Table 1.

## Discussion

Tregs are a small subset of CD4$^+$ T lymphocytes but they play a crucial role in maintaining the balance of the immune system. In transplant medicine, Tregs
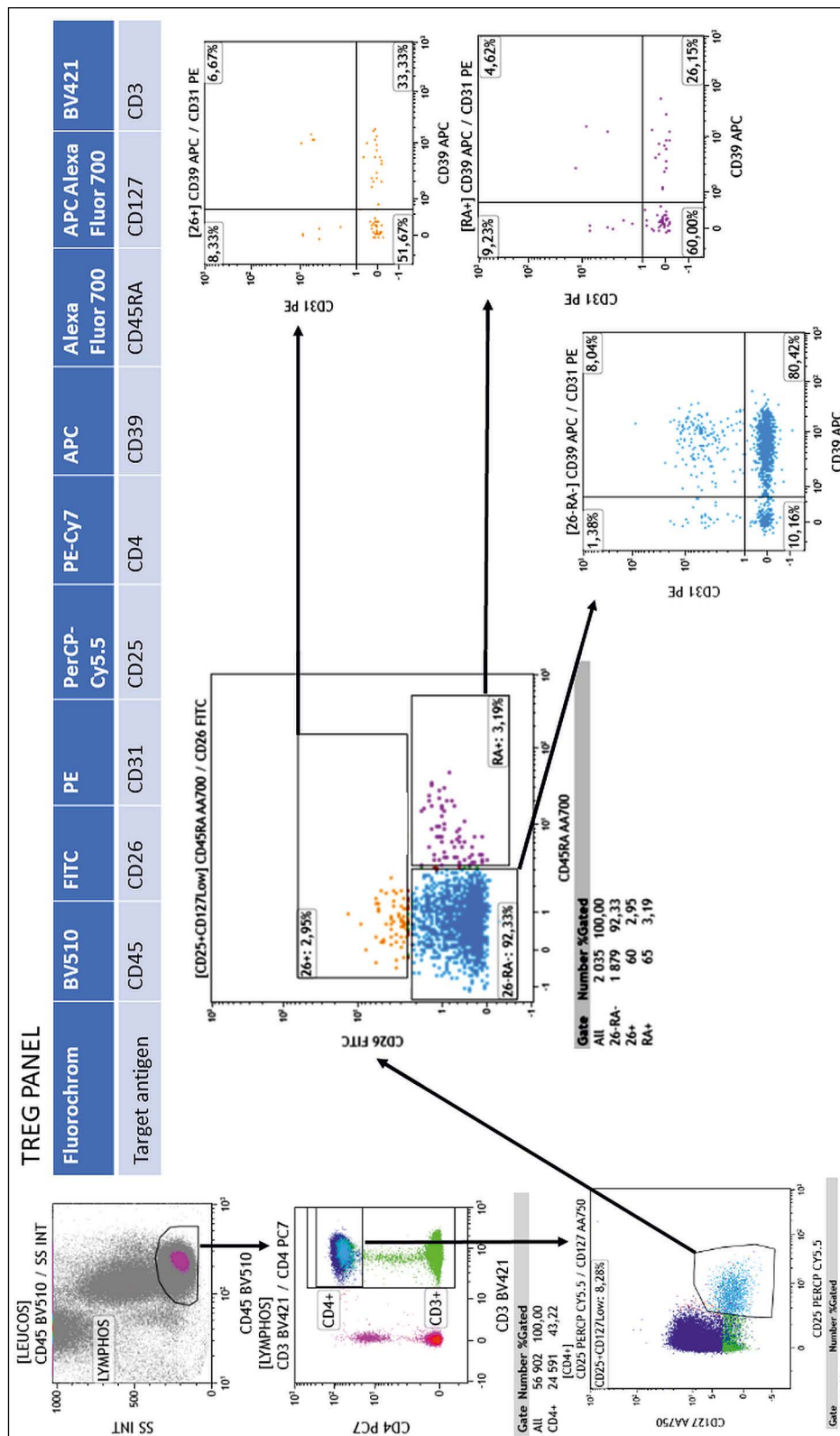
**Figure 5.** The enumeration panel and the final gating strategy. Lymphocytes are gated on a CD45/SS dot plot, then CD4$^+$ T cells (CD3$^+$CD4$^+$ cells) are gated on a CD3/CD4 dot plot. Tregs are initially identified as CD25$^+$CD127$^{low/-}$ on a CD25/ /CD127 dot plot. The next step is to exclude cells with intermediate or high expression of CD26 on a CD45RA/CD26 dot plot (among CD25$^+$CD127$^{low/-}$). The cells detected after the elimination of CD26$^+$ cells are taken to obtain the total number of Tregs. In the CD45RA/CD26 dot plot, the lower two quadratic gates are placed to discriminate effector/memory (CD45RA$^-$CD26$^{low/-}$) and naïve Tregs (CD45RA$^+$CD26$^{low/-}$). The next step to characterize Treg subsets is to check CD31 and CD39 expression within these two gates.

**Table 1.** Comparison of percentages and absolute values of Tregs in healthy donors and patients with chronic GVHD

| T regulatory cells | Phenotype within CD45+CD3+CD4+ | Healthy donors Median (range) | Patients with cGVHD Median (range) | Normal range | Units |
|---|---|---|---|---|---|
| **Total** | **CD25+CD127-/low** **CD26-/low** | 5.4 (3.2–10.7) 66.4 (22.8–162.7) | 5.1 (2.1–15.8) 33.6 (15.3–91.5) | 4–10.7 20–126.3 | % (in CD4+) cells/μl |
| Effector/ /Memory | CD25+CD127-/low CD26-/low **CD45RA-** | 3.8 (1.3–10.3) 43 (15.6–81.4) | 4.6 (2.1–14.7) 25.8 (15–63.6) | 2.4–8.7 14.3–88.3 | % (in CD4+) cells/μl |
| Naïve | CD25+CD127-/low CD26-/low **CD45RA+** | 1.4 (0.4–5.0) 16.9 (2.2–103.5) | 0.8 (0.04–2.0) 4.4 (0.2–28.0) | 0.4–4.5 2.3–54.0 | % (in CD4+) cells/μl |
| Highly suppressive | CD25+CD127-/low CD26-/low **CD39+** | 2.4 (1–8.7) 18.5 (1.7–84.5) | 2.7 (0.8–4.7) 15.7 (7.3–45.2) | | % (in CD4+) cells/μl |
| Thymus emigrants | CD25+CD127-/low CD26-/low **CD31+** | 1.5 (0.8–4.2) 16.3 (4.6–88) | 1.4 (0.3–4.2) 8.6 (1.2–29.5) | | % (in CD4+) cells/μl |

are responsible for the induction of the immuno-tolerance that preserves the transplanted organ or tissue. This T-cell subset prevents GVHD development after HCT [1, 30]. The identification of Tregs is beneficial for clinical purposes, *e.g.*, to monitor immune responses to immunomodulating therapies after HCT, to isolate and to sort viable regulatory cells for tolerance-inducing therapies or to eliminate tumor-infiltrating Tregs and activate anti-tumor immune responses. A growing need to find a reliable and accurate method to identify a Treg compartment inspired us to design a simple protocol that could be used in flow cytometry laboratories as a routine analytical procedure [13].

Tregs in humans are heterogeneous in both immunophenotype and function. They consist of subsets of highly suppressive, terminally differentiated effector or activated Tregs and naïve or resting Tregs with hidden suppressive potential [22, 31]. This population is also diversified according to its origin into natural tTregs and induced Tregs that differentiate upon exposure to an antigen under tolerogenic conditions in peripheral tissues (pTregs) [32–34]. There are also Tcons deprived of suppressive activity that secrete pro-inflammatory cytokines but, upon activation, they are able transiently to upregulate FoxP3 [17]. The nuclear localization of FoxP3 makes the permeabilization of cellular and nuclear membranes necessary for FoxP3 detection, and this may lead to inaccurate enumeration due to cell loss and the omission of cells with low FoxP3 fluorescence intensity [14]. During the last decade, several Treg-associated membrane markers have been identified, and their ability to isolate functional Tregs has been tested primarily in the context of cell sorting. Following these studies, some of the well-known surface antigens were chosen and tested by us in various combinations.

The CD25 antigen (alpha-chain for the interleukin (IL)-2 receptor) is a primary cell-surface marker for Tregs, but its high expression on CD4+ cells means that it cannot be used as the sole criterion to capture Tregs because even a pure CD4+CD25high population contains substantial contamination with proinflammatory T cells [35, 36]. Therefore, additional selective markers are needed. Tregs exhibit consistently low expression of CD127- alpha chain for the IL-7 receptor. The low/negative expression of CD127 antigen has been tested in combination with CD4 and CD25, showing high levels of FoxP3 and a strong correlation with T cells expressing CD4+CD25+FoxP3+ [16, 20, 24]. Moreover, CD4+CD25+CD127low/- cells expressing a low level of FoxP3 remain strongly suppressive [19]. Similarly, the low/negative CD6 expression is indicated to be another Treg-associated marker. Cells sorted by the CD4+CD25highCD127low/-CD6low/- immunophenotype showed high enrichment of FoxP3+ cells and high *in vitro* suppression activity [26]. The use of CD6 as a negative Treg marker was tested in our study in comparison with CD26 and gave comparable results. However, for the sake of simplicity, in the final enumeration strategy, the elimination of CD26+ cells appeared to be more apparent than that of CD6+ cells. In turn, the CD26 antigen is an extracellular peptidase that is upregulated in CD4+ effector T cells, in contrast to CD127, which is not upregulated upon activation [27]. Following this path, because negative/low CD26 expression enables distinction between activated Tcons and Tregs, CD26 was chosen for the final gating strategy. Another tested marker, the CD39 antigen, is ectonucleoside triphosphate diphosphohydrolase 1, which hydrolyzes extracellular ATP and ADP to AMP. CD39 is presented in the literature as defining a Treg subset with a frequency and expression level that correlate

with those of FoxP3 in CD4$^+$ T cells [25]. A comparison performed in our analyses confirmed the almost overlapping expression of FoxP3 and CD39 in cells selected by other cell-surface Treg-associated markers.

We found high expression of FoxP3 and CD39 within the CD45RA$^-$ subpopulation and low expression within the CD45RA$^+$ subpopulation, which is in agreement with data from the literature [22]. However, low expression of suppressive markers FoxP3 and CD39 did not deprive a naïve CD45RA$^+$ subset of the Treg compartment in our study. It was demonstrated that CD4$^+$CD127$^{low/-}$CD25$^+$CD45RA$^+$ cells have a stable TSDR (T-cell specific demethylation region) demethylated phenotype [22, 31]. Naïve Tregs express CD127 antigen at reduced levels and CD25 antigen at lower levels than memory Tregs express, which is why cells with intermediate expression of CD25 and low expression of CD127 were captured in our analyses [37].

Taking into account the expression of CD31 antigen, we intended to identify a Treg subpopulation that is especially interesting in the HCT setting. CD31 (platelet endothelial cell adhesion molecule; PECAM-1) was included as a marker to identify CD4$^+$ recent thymus emigrants (RTEs) that may persist in circulation expressing CD31. In a study by Douaisi *et al.*, most egress-capable mature CD45RA$^+$ single-positive (SP) CD4$^+$ thymocytes express CD31; however, FoxP3-expressing cells in the thymus are overrepresented within the CD31$^-$ semimature CD45RA$^-$CD4 SP subset displaying enhanced levels of activation markers, while among mature CD45RA$^+$CD4 SP thymocytes, the frequency of the FoxP3$^+$ cells is similar in CD31$^-$ and CD31$^+$ subsets [28]. It is hypothesized that CD31$^-$ semimature CD45RA$^-$CD4 SP thymocytes re-express CD31 upon the completion of their maturation and the acquisition of CD45RA, egressing from the thymus as RTEs. However, it cannot be excluded that a subset of CD31$^-$CD45RA$^+$CD4$^+$ thymocytes can egress from the thymus and become difficult to distinguish from the naïve peripheral CD31$^-$CD4$^+$ T cells. Generally, the expression of CD31 is downregulated upon T-cell receptor activation and cell division. To distinguish highly suppressive Tregs (effector/memory Tregs) from naïve or resting cells with suppressive potential, we used the membrane markers CD45RA, CD31, and CD39. Within cells with the naïve immunophenotype CD45RA$^+$ (basically CD39$^-$HLA-DR$^-$) we could identify CD31$^+$ tTregs that are RTEs and CD31$^-$ that would be extrathymic pTregs, but according to the data cited above, the thymic origin cannot be excluded. In turn, within CD4$^+$CD25$^+$CD127$^{low/-}$CD26$^{low/-}$ cells,

we identified effector highly suppressive Tregs defined as having the CD45RA$^-$CD31$^-$CD39$^+$ immunophenotype, and activated tTregs after the transition to CD45RA$^-$CD31$^+$CD39$^+$ effector cells, while cells with the CD45RA$^-$CD31$^-$CD39$^-$ phenotype could be a memory resting pool of pTregs or tTregs with a transiently downregulated suppressive marker. A deeper insight into the Treg subpopulation is especially exciting for transplantation physicians because highly activated CD45RA$^-$CD39$^+$FoxP3$^+$ Tregs traffic into tissues involved in cGVHD-related processes, where they play a suppressive function while naïve CD45RA$^+$ Tregs control cGVHD effectors [38]. Another interesting issue refers to a hypothesis that the maintenance of the naïve Treg compartment may be predominantly thymic-independent, with a strong role of IL-7 dependent signaling [39]. Clinical improvement following ECP or other Treg-enhancing immunomodulatory therapies in patients with GVHD supports this thesis. There are data showing that clinical amelioration correlates with increasing levels of Tregs, despite the debilitating alloimmune processes involving the thymus that occur in the course of GVHD [6–8, 12]. On a laboratory basis, shifts within the CD4$^+$ and Treg compartments could be efficiently evaluated with the use of our protocol in patients suffering from cGVHD who undergo immunomodulatory treatment. Eight of the 10 patients had been treated with ECP for more than 1 year, with partial remission of skin manifestations of GVHD at the time of our Treg analyses. Their results vary, but the median values are generally lower when compared with those of healthy volunteers, especially the naïve Tregs compartment. However, further tests in patients with cGVHD are required to record the shifts of Treg subsets upon treatment on the timeline.

The final results of Treg enumeration were presented as both a percentage of CD4$^+$ cells and an absolute count per microliter in whole blood. The literature suggests that it is essential to provide both values to show real differences [13]. After HCT, the Treg/CD4 ratio is reported to be altered in patients with severe GVHD and in cases of relapse, while the reconstitution of Tregs achieves the highest absolute numbers in patients without GVHD [40].

In summary, the final panel we propose gives the possibility of obtaining reproducible and comparable results when capturing an entire Treg compartment in whole blood. Moreover, it enables insight into Treg subsets. With the use of the additional cell-surface markers CD45RA and CD31, the panel gives additional information about the functionality, maturity and origin of Tregs.

## Authorship statement
AP — study concept and design, data analysis and interpretation, and writing the paper; MP — data analysis and interpretation, participation in drafting the text, and critical revision; MT and MK — data analysis and critical revision; KL — data analysis and interpretation, participation in drafting the text, and critical revision; FV — study supervision, data interpretation, and critical revision. All authors accepted the final content of the manuscript.

## Conflict of interest
The authors declare no conflict of interest.

## References

1. Trenado A, Charlotte F, Fisson S, et al. Recipient-type specific CD4+CD25+ regulatory T cells favor immune reconstitution and control graft-versus-host disease while maintaining graft-versus-leukemia. J Clin Invest. 2003; 112(11): 1688–1696, doi: 10.1172/JCI17702, indexed in Pubmed: 14660744.

2. Sakaguchi S, Yamaguchi T, Nomura T, et al. Regulatory T cells and immune tolerance. Cell. 2008; 133(5): 775–787, doi: 10.1016/j.cell.2008.05.009, indexed in Pubmed: 18510923.

3. Couriel DR, Hosing C, Saliba R, et al. Extracorporeal photochemotherapy for the treatment of steroid-resistant chronic GVHD. Blood. 2006; 107(8): 3074–3080, doi: 10.1182/blood-2005-09-3907, indexed in Pubmed: 16368882.

4. Gorgun G, Miller KB, Foss FM, et al. Extracorporeal photopheresis in chronic graft-versus-host disease. Bone Marrow Transplant. 2002; 29(9): 719–725, doi: 10.1038/sj.bmt.1703529, indexed in Pubmed: 12040467.

5. Rubegni P, Sbano P, Cevenini G, et al. CD4+CD25+ lymphocyte subsets in chronic graft versus host disease patients undergoing extracorporeal photochemotherapy. Int J Immunopathol Pharmacol. 2007; 20(4): 801–807, doi: 10.1177/039463200702000416, indexed in Pubmed: 18179753.

6. Biagi E, Di Biaso I, Leoni V, et al. Extracorporeal photochemotherapy is accompanied by increasing levels of circulating CD4+CD25+GITR+Foxp3+CD62L+ functional regulatory T-cells in patients with graft-versus-host disease. Transplantation. 2007; 84(1): 31–39, doi: 10.1097/01.tp.0000267785.52567.9c, indexed in Pubmed: 17627234.

7. Schmitt S, Johnson TS, Karakhanova S, et al. Extracorporeal photophoresis augments function of CD4+CD25+FoxP3+ regulatory T cells by triggering adenosine production. Transplantation. 2009; 88(3): 411–416, doi: 10.1097/TP.0b013e-3181aed927, indexed in Pubmed: 19667946.

8. Gao W, Lu Y, El Essawy B, et al. Contrasting effects of cyclosporine and rapamycin in de novo generation of alloantigen-specific regulatory T cells. Am J Transplant. 2007; 7(7): 1722–1732, doi: 10.1111/j.1600-6143.2007.01842.x, indexed in Pubmed: 17511761.

9. Jedlickova Z, Burlakova I, Bug G, et al. Therapy of sclerodermatous chronic graft-versus-host disease with mammalian target of rapamycin inhibitors. Biol Blood Marrow Transplant. 2011; 17(5): 657–663, doi: 10.1016/j.bbmt.2010.07.025, indexed in Pubmed: 20696263.

10. Teshima T. JAK inhibitors: a home run for GVHD patients? Blood. 2014; 123(24): 3691–3693, doi: 10.1182/blood-2014-04-570325, indexed in Pubmed: 24926071.

11. Zeiser R, Nguyen VuH, Beilhack A, et al. Inhibition of CD4+CD25+ regulatory T-cell function by calcineurin-dependent interleukin-2 production. Blood. 2006; 108(1): 390–399, doi: 10.1182/blood-2006-01-0329, indexed in Pubmed: 16522809.

12. Di Biaso I, Di Maio L, Bugarin C, et al. Regulatory T cells and extracorporeal photochemotherapy: correlation with clinical response and decreased frequency of proinflammatory T cells. Transplantation. 2009; 87(9): 1422–1425, doi: 10.1097/TP.0b013e3181a27a5d, indexed in Pubmed: 19424046.

13. Hardy MY, Vari F, Rossetti T, et al. A flow cytometry based assay for the enumeration of regulatory T cells in whole blood. J Immunol Methods. 2013; 390(1-2): 121–126, doi: 10.1016/j.jim.2012.07.004, indexed in Pubmed: 22824721.

14. Fazekas de St Groth B, Zhu E, Asad S, et al. Flow cytometric detection of human regulatory T cells. Methods Mol Biol. 2011; 707: 263–279, doi: 10.1007/978-1-61737-979-6_17, indexed in Pubmed: 21287341.

15. Pitoiset F, Barbié M, Monneret G, et al. A standardized flow cytometry procedure for the monitoring of regulatory T cells in clinical trials. Cytometry B Clin Cytom. 2018; 94(5): 621–626, doi: 10.1002/cyto.b.21622, indexed in Pubmed: 29316248.

16. Pitoiset F, Cassard L, El Soufi K, et al. Deep phenotyping of immune cell populations by optimized and standardized flow cytometry analyses. Cytometry A. 2018; 93(8): 793–802, doi: 10.1002/cyto.a.23570, indexed in Pubmed: 30168890.

17. d'Hennezel E, Piccirillo CA. Analysis of human FOXP3+ Treg cells phenotype and function. Methods Mol Biol. 2011; 707: 199–218, doi: 10.1007/978-1-61737-979-6_13, indexed in Pubmed: 21287337.

18. Seddiki N, Santner-Nanan B, Martinson J, et al. Expression of interleukin (IL)-2 and IL-7 receptors discriminates between human regulatory and activated T cells. J Exp Med. 2006; 203(7): 1693–1700, doi: 10.1084/jem.20060468, indexed in Pubmed: 16818676.

19. Klein S, Kretz CC, Krammer PH, et al. CD127(low/-) and FoxP3(+) expression levels characterize different regulatory T-cell populations in human peripheral blood. J Invest Dermatol. 2010; 130(2): 492–499, doi: 10.1038/jid.2009.313, indexed in Pubmed: 19940860.

20. Yu N, Li X, Song W, et al. CD4(+)CD25 (+)CD127 (low/-) T cells: a more specific Treg population in human peripheral blood. Inflammation. 2012; 35(6): 1773–1780, doi: 10.1007/s10753-012-9496-8, indexed in Pubmed: 22752562.

21. Hartigan-O'Connor DJ, Poon C, Sinclair E, et al. Human CD4+ regulatory T cells express lower levels of the IL-7 receptor alpha chain (CD127), allowing consistent identification and sorting of live cells. J Immunol Methods. 2007; 319(1-2): 41–52, doi: 10.1016/j.jim.2006.10.008, indexed in Pubmed: 17173927.

22. Arroyo Hornero R, Betts GJ, Sawitzki B, et al. CD45RA Distinguishes CD4+CD25+CD127-/low TSDR demethylated

regulatory T cell subpopulations with differential stability and susceptibility to tacrolimus-mediated inhibition of suppression. Transplantation. 2017; 101(2): 302–309, doi: 10.1097/TP.0000000000001278, indexed in Pubmed: 28118317.

23. Seddiki N, Santner-Nanan B, Tangye SG, et al. Persistence of naive CD45RA+ regulatory T cells in adult life. Blood. 2006; 107(7): 2830–2838, doi: 10.1182/blood-2005-06-2403, indexed in Pubmed: 16332974.

24. Nettenstrom L, Alderson K, Raschke EE, et al. An optimized multi-parameter flow cytometry protocol for human T regulatory cell analysis on fresh and viably frozen cells, correlation with epigenetic analysis, and comparison of cord and adult blood. J Immunol Methods. 2013; 387(1-2): 81–88, doi: 10.1016/j.jim.2012.09.014, indexed in Pubmed: 23058673.

25. Mandapathil M, Lang S, Gorelik E, et al. Isolation of functional human regulatory T cells (Treg) from the peripheral blood based on the CD39 expression. J Immunol Methods. 2009; 346(1-2): 55–63, doi: 10.1016/j.jim.2009.05.004, indexed in Pubmed: 19450601.

26. Garcia Santana CA, Tung JW, Gulnik S. Human treg cells are characterized by low/negative CD6 expression. Cytometry A. 2014; 85(10): 901–908, doi: 10.1002/cyto.a.22513, indexed in Pubmed: 25088497.

27. Salgado FJ, Pérez-Díaz A, Villanueva NM, et al. CD26: a negative selection marker for human Treg cells. Cytometry A. 2012; 81(10): 843–855, doi: 10.1002/cyto.a.22117, indexed in Pubmed: 22949266.

28. Douaisi M, Resop RS, Nagasawa M, et al. CD31, a valuable marker to identify early and late stages of T Cell differentiation in the human thymus. J Immunol. 2017; 198(6): 2310–2319, doi: 10.4049/jimmunol.1500350, indexed in Pubmed: 28159903.

29. Motamedi M, Xu L, Elahi S. Correlation of transferrin receptor (CD71) with Ki67 expression on stimulated human and mouse T cells: The kinetics of expression of T cell activation markers. J Immunol Methods. 2016; 437: 43–52, doi: 10.1016/j.jim.2016.08.002, indexed in Pubmed: 27555239.

30. Sprangers B, DeWolf S, Savage TM, et al. Origin of enriched regulatory T cells in patients receiving combined kidney-bone marrow transplantation to induce transplantation tolerance. Am J Transplant. 2017; 17(8): 2020–2032, doi: 10.1111/ajt.14251, indexed in Pubmed: 28251801.

31. Tanaka A, Sakaguchi S, Tanaka A, et al. Regulatory T cells in cancer immunotherapy. Cell Res. 2017; 27(1): 109–118, doi: 10.1038/cr.2016.151, indexed in Pubmed: 27995907.

32. Curotto de Lafaille MA, Kutchukhidze N, Shen S, et al. Adaptive Foxp3+ regulatory T cell-dependent and -independent control of allergic inflammation. Immunity. 2008; 29(1): 114–126, doi: 10.1016/j.immuni.2008.05.010, indexed in Pubmed: 18617425.

33. Horwitz DA, Zheng SG, Gray JD. Natural and TGF-beta-induced Foxp3(+)CD4(+) CD25(+) regulatory T cells are not mirror images of each other. Trends Immunol. 2008; 29(9): 429–435, doi: 10.1016/j.it.2008.06.005, indexed in Pubmed: 18676178.

34. Abbas AK, Benoist C, Bluestone JA, et al. Regulatory T cells: recommendations to simplify the nomenclature. Nat Immunol. 2013; 14(4): 307–308, doi: 10.1038/ni.2554, indexed in Pubmed: 23507634.

35. Dieckmann D, Plottner H, Berchtold S, et al. Ex vivo isolation and characterization of CD4(+)CD25(+) T cells with regulatory properties from human blood. J Exp Med. 2001; 193(11): 1303–1310, doi: 10.1084/jem.193.11.1303, indexed in Pubmed: 11390437.

36. Kleinewietfeld M, Starke M, Di Mitri D, et al. CD49d provides access to „untouched" human Foxp3+ Treg free of contaminating effector cells. Blood. 2009; 113(4): 827–836, doi: 10.1182/blood-2008-04-150524, indexed in Pubmed: 18941119.

37. Silva SL, Albuquerque AS, Serra-Caetano A, et al. Human naïve regulatory T-cells feature high steady-state turnover and are maintained by IL-7. Oncotarget. 2016; 7(11): 12163–12175, doi: 10.18632/oncotarget.7512, indexed in Pubmed: 26910841.

38. Imanguli MM, Cowen EW, Rose J, et al. Comparative analysis of FoxP3(+) regulatory T cells in the target tissues and blood in chronic graft versus host disease. Leukemia. 2014; 28(10): 2016–2027, doi: 10.1038/leu.2014.92, indexed in Pubmed: 24577531.

39. Silva SL, Sousa AE. Establishment and maintenance of the human naïve CD4 T-cell compartment. Front Pediatr. 2016; 4: 119, doi: 10.3389/fped.2016.00119, indexed in Pubmed: 27843891.

40. Willasch AM, Salzmann-Manrique E, Krenn T, et al. Advanced flowcytometric analysis of regulatory T cells: CD127 downregulation early post stem cell transplantation and altered Treg/CD3(+)CD4(+)-ratio in severe GvHD or relapse. J Immunol Methods. 2011; 373(1-2): 36–44, doi: 10.1016/j.jim.2011.07.018, indexed in Pubmed: 21839739.

ORIGINAL PAPER

**V M**
**VIA MEDICA**

# Immunohistochemical analysis of ghrelin expression in various types of adrenal tumors

Hanna Komarowska[1], Agnieszka Malinska[2], Zhanat Komekbai[3], Barbara Brominska[1], Katarzyna Bednarek-Rajewska[4], Marek Ruchala[1], Marcin Rucinski[2]

[1]Department of Endocrinology, Metabolism and Internal Medicine, Poznan University of Medical Sciences, Poznan, Poland
[2]Department of Histology and Embryology, Poznan University of Medical Sciences, Poznan, Poland
[3]West Kazakhstan Marat Ospanov Medical University, Aktobe, Kazakhstan
[4]Department of Clinical Pathology, Poznan University of Medical Sciences, Poznan, Poland

**Abstract**

**Introduction.** Ghrelin, originally isolated from the endocrine cells of the gastric mucosa, is also expressed in many peripheral tissues, including normal adrenals and adrenocortical tumors. It was shown that ghrelin stimulates proliferation and inhibits apoptosis of adrenocortical cells. In the current study, we compared ghrelin expression at the protein level in various adrenal tumors. We analyzed whether immunoreactive ghrelin could be considered as a potential marker for different types of adrenal tumors.

**Material and methods.** Study was carried out on 200 adrenal specimens arranged on microscope slide in tissue microarray format. We performed standardized immunohistochemical reactions with semiquantitative reaction intensity measurements.

**Results.** At the protein level, the expression of ghrelin was significantly reduced in adrenocortical adenocarcinoma in relation to the control group and pheochromocytoma as well as cancer-adjacent normal adrenal tissue. In contrast, a relatively high ghrelin expression was found in pheochromocytoma compared to all analyzed groups, with the exception of cancer-adjacent normal adrenal tissue.

**Conclusions.** The ghrelin expression profile at the protein level may be associated with the type of adrenal tumor. In this context, our results suggest that adrenal immunoreactive ghrelin may be considered as a sensitive and specific marker for differentiating adrenocortical carcinoma from adrenocortical adenoma and pheochromocytoma. *(Folia Histochemica et Cytobiologica 2021, Vol. 59, No. 2, 86–94)*

**Key words:** ghrelin; immunohistochemistry; adrenal tumors; adrenal cortex; adrenal medulla

## Introduction

The management of adrenal tumors is quite challenging, mainly due to their growing frequency, diagnostic complexity, and limited availability of treatment option

for adrenocortical carcinoma (ACC). In patients without *premortem* suspicion of adrenal disease, the prevalence of adrenal tumors at autopsy is found to be as high as 32%. The occurrence of adrenal incidentaloma (AI) in computed tomography series is approximately 5% [1], whereas about 80% of cases are benign adenomas. More complex lesions such as adrenocortical carcinoma (ACC) or pheochromocytoma are rarely diagnosed at a rate of about 5% each, while 2% of AI turns out to be metastases [1, 2]. Other lesions including ganglioneuroma, neuroblastoma, myelolipoma, cysts, or inflammatory tumors are detected occasionally.

**Correspondence address:** Hanna Komarowska, MD, PhD
Department of Endocrinology, Metabolism
and Internal Medicine, Poznan University of Medical Sciences,
Przybyszewskiego 49, 60–355 Poznan, Poland
e-mail: hkomar@ump.edu.pl
phone: +4861 869 1330; fax: 61 869 1682

Most of the adrenal tumors remain hormonally inactive. However, depending on the level of hormonal activity, these tumors may cause various symptoms. Patients with active adrenal tumors or suspected malignancies are usually referred for adrenalectomy [1].

ACC is a rare, highly aggressive cancer. It has an incidence of about 0.7–2 new cases *per* million *per* year. ACC is more frequently detected in 40–60 years old people [3]. The diameter of this tumor usually ranges from 5 to 20 cm [3]. ACC is diagnosed using Weiss criteria with Aubert's modifications [4]. Pathological assessment is crucial for the correct diagnosis of ACC, but it is difficult to perform. Moreover, the frequency of misdiagnoses is relatively high. For instance, in a large consecutive series consisting of 300 cases tested in Italy, 26 (13%) were misdiagnosed. The most common problem encountered in the diagnosis of ACC is the differentiation pheochromocytoma from ACC. Other diagnostic pitfalls include metastases from other primary cancers, primary tumors of adrenal soft tissue, and adrenal adenomas [5–7]. Due to these reasons, there is a high demand for the identification of ACC markers.

Ghrelin is the ligand of growth hormone secretagogue receptor type 1 (GHS-R1) [8]. It was first identified by Kojima *et al.* as a 28-amino acid peptide, having an n-octanoyl moiety in serine 3 position [8]. Ghrelin is generated from the preproghrelin precursor during post-translational cleavage. Ghrelin is predominantly secreted by endocrine cells of the gastric mucosa, but its expression was also found in many other organs, including the small and large intestine, hypothalamus, pituitary, adrenal glands, testes, ovaries, thyroid gland, liver or lungs [8–14]. The main role of ghrelin is to regulate energy homeostasis and secretion of growth hormone. Thus far, many studies have confirmed the physiological and pathological effects of ghrelin on various organs [15–18]. Ghrelin and its receptors (GHS-R1a and GHS-R1b) were found in human adrenal glands [19]. Ghrelin does not influence the secretion of adrenal steroid hormones [20]. However, it increases the proliferation and decreases the apoptosis of adrenocortical cells [21, 22]. The ghrelin mRNA level in the human adrenal glands was evaluated in previous studies, using mainly the qPCR technique [9, 10, 23].

Currently, 13 alternative splice transcript variants of the ghrelin gene are described in the NCBI database; however, not all of them are translated into protein. Individual variants of the ghrelin gene also differ in the length of the 3' and 5' untranslated regions, which determine the stability of these transcripts [24, 25]. Therefore, it can be assumed that the expression of ghrelin at the mRNA level may not correlate with that at the protein level. Due to the aforementioned facts, our study aimed to compare the expression of ghrelin at the protein level in various adrenal tumors using the immunohistochemical (IHC) technique with a tissue microarray (TMA) containing 200 human adrenal samples. We also analyzed whether immunoreactive ghrelin can be considered as a potential marker for different types of adrenal tumors. To the best of our knowledge, this study is the first to evaluate the ghrelin protein level in a relatively large group of tissues derived from various adrenal tumors.

## Materials and methods

**Tissue material.** The unstained adrenal gland disease spectrum (adrenal cancer progression) tissue microarray (TMA) slide (AD2081) was purchased from US Biomax, Inc. (Rockville, MD, USA). This histological slide contained 200 cores of adrenal gland tissue specimens, which included 20 samples of adrenocortical adenocarcinoma, 6 neuroblastoma, 2 ganglioneuroma, 60 pheochromocytoma, and 84 adrenocortical adenoma (ACA), in addition to 12 samples of normal tissue adjacent to ACC and 16 biopsy samples of normal adrenal tissue. Since we used the commercially available TMA slide, our study did not require the approval of local bioethics commission. Research complies with the Declaration of Helsinki.

**Immunohistochemical analyses.** For the IHC analyses, we employed the StreptABComplex/HRP method modified by biotinylated tyramine (Dako Catalysed Signal Amplification System, Peroxidase, K1500; Dako, Copenhagen, Denmark). Briefly, after deparaffinization, the sections were rehydrated in decreasing concentrations of ethanol and rinsed in phosphate-buffered saline (PBS). Antigen expression was enhanced by heat-induced epitope retrieval (HIER) treatment of tissue samples. The slides were placed in Target Retrieval Solution, Citrate pH 6.1 (S2369; Dako), steamed for 5 min, and then allowed to cool to room temperature (RT) in the buffer for 20 min. After rinsing in PBS, the endogenous activity of peroxidase was blocked by treating the sections with 10% hydrogen peroxide for 10 min, while the nonspecific-binding sites were blocked by incubating with 10%t normal goat serum in PBS for 30 min at RT (ab7481: Abcam). Following this step, the sections were incubated with a mouse monoclonal anti-ghrelin antibody (1:100, ab57222; Abcam) overnight at 4°C. Then, the tissue samples were rinsed and incubated with a biotinylated goat anti-mouse antibody (1:300; Dako) for 60 min at RT before incubation with streptavidin-horse radish peroxidase conjugate. The peroxidase reaction was developed using diaminobenzidine (S3000; Dako). Then, the specimens were lightly counterstained with Mayer's hematoxylin, dehydrated, and mounted. The sections incubated with nonimmune

IgG1 (X 0931; Dako) as well as those in which the primary or secondary antibody was omitted were treated as negative controls. To determine the consistency of antibodies reactivity, commercially available serial sections obtained from the human gastric fundus (NBP2-30204; Novus Biologicals, Centennial, CO, USA) were used as external positive controls. The whole slide was digitalized with a Mirax-Midi slide scanner (Zeiss, Jena, Germany). The IHC staining was analyzed and documented at a high magnification using CaseViewer 2.3 (64-bit version) for Windows (3D Histech Ltd., Budapest, Hungary).

**Semiquantitative evaluation of ghrelin protein expression.**
The expression of ghrelin protein was analyzed using the densitometric method. First, the blue-violet stain produced by hematoxylin was removed from the scanned slide, retaining only the brown stain of the appropriate IHC reaction, using Adobe Photoshop ver. 21.1.0 (Adobe Inc., San Jose, CA, USA). The image thus prepared was subjected to densitometric analysis using ImageJ software (ImageJ 1.5q, Wayne Rasband, National Institutes of Health, Bethesda, MD, USA) according to The Open Lab Book protocol (https://theolb.readthedocs.io/en/latest/imaging/measuring-cell-fluorescence-using-imagej.html) adapted to the TMA format. Using this software, the integrated density from each of the TMA specimens was calculated, with the fixed diameter covering 8800 pixels/specimen. The signal of the background was also determined and subtracted from that of the measured specimens.

**Statistical analysis.** All the statistical analyses were performed using the R programming language environment supported by the "ggplot2" library for graph drawing. Densitometric values determined from each of the studied groups were presented as a boxplot, with the values of median and interquartile range (IQR), and the densitometric data from individual patients were superimposed on the appropriate boxplots and displayed as dots. Comparisons between the groups were carried out using Kruskal-Wallis test followed by Dunn *post hoc* test. The differences between the groups were indicated using the letter annotation, where different letters indicate significant ($p < 0.05$) differences between the compared groups. To evaluate the applicability of ghrelin as a potential biomarker for the differentiation of different types of adrenal tumors, we used the receiver operating characteristic (ROC) curve plot generated in the "pROC" library [26].

## Results

To investigate the ghrelin's expression in various types of adrenal tumors and normal adrenal gland tissues, we used the commercially available adrenal gland disease spectrum (adrenal cancer progression)

tissue array. The same experimental conditions were applied to all the samples, allowing for standardized IHC reactions and more reliable semiquantitative measurements. The expression analysis was carried out on 200 adrenal specimens described in the Material and Methods section. The general profile of the stained specimens is presented in Figure 1. Within the entire tissue array, the anti-ghrelin IHC staining of different intensities, ranging from relatively weak to strong, was observed.

To assess semiquantitatively expression of ghrelin at the protein level, we performed densitometric analysis using ImageJ software. The integrated density values obtained for individual patients assigned to appropriate groups are presented in Figure 2. Statistical analysis performed using the nonparametric Kruskal-Wallis test revealed a very low p-value (p = 6.48e 13), indicating significant differences between the compared groups. The subsequent Dunn *post hoc* test showed that the expression of ghrelin at the protein level was significantly lower by 30% in adrenocortical adenocarcinoma (median [IQR] = 78.56 [80.2–65.1]) in relation to the control group (median [IQR] = 110.87 [118.45–99.44]) as well as both pheochromocytoma (median [IQR] = 133.4 [147.56–109.77]) and cancer-adjacent normal adrenal tissue (median [IQR] = 118.26 [126.35–97.93]). A relatively low level of ghrelin expression was also observed in neuroblastoma (median [IQR] = 90.36 [98–82.92]), compared to ACC, pheochromocytoma, and cancer-adjacent normal adrenal tissue. By contrast, a relatively high level of ghrelin expression was found in pheochromocytoma, in which the expression was significantly higher by 20% in relation to the control group. The expression of ghrelin in the pheochromocytoma was also significantly higher than all the other analyzed groups, except for cancer-adjacent normal adrenal tissue. Due to its small number, the ganglioneuroblastoma group was excluded from the statistical analyses.

Although no statistically significant difference was observed in ghrelin expression between the normal adrenal and cancer-adjacent normal adrenal tissue, it should be noted that there was a markedly stronger anti-ghrelin reaction in tumor-adjacent normal adrenal tissue with respect to tumor cells (Figs. 3G and 3H), which confirmed the previously reported results. In the detailed analysis of ghrelin expression at high magnification, we observed a strong cytoplasmic expression of ghrelin within the adrenal cortex and chromaffin parenchymal cells compared to the relatively weakly stained connective tissue and vascular endothelium. Strong nuclear staining was observed in several ACA and pheochromocytoma samples.
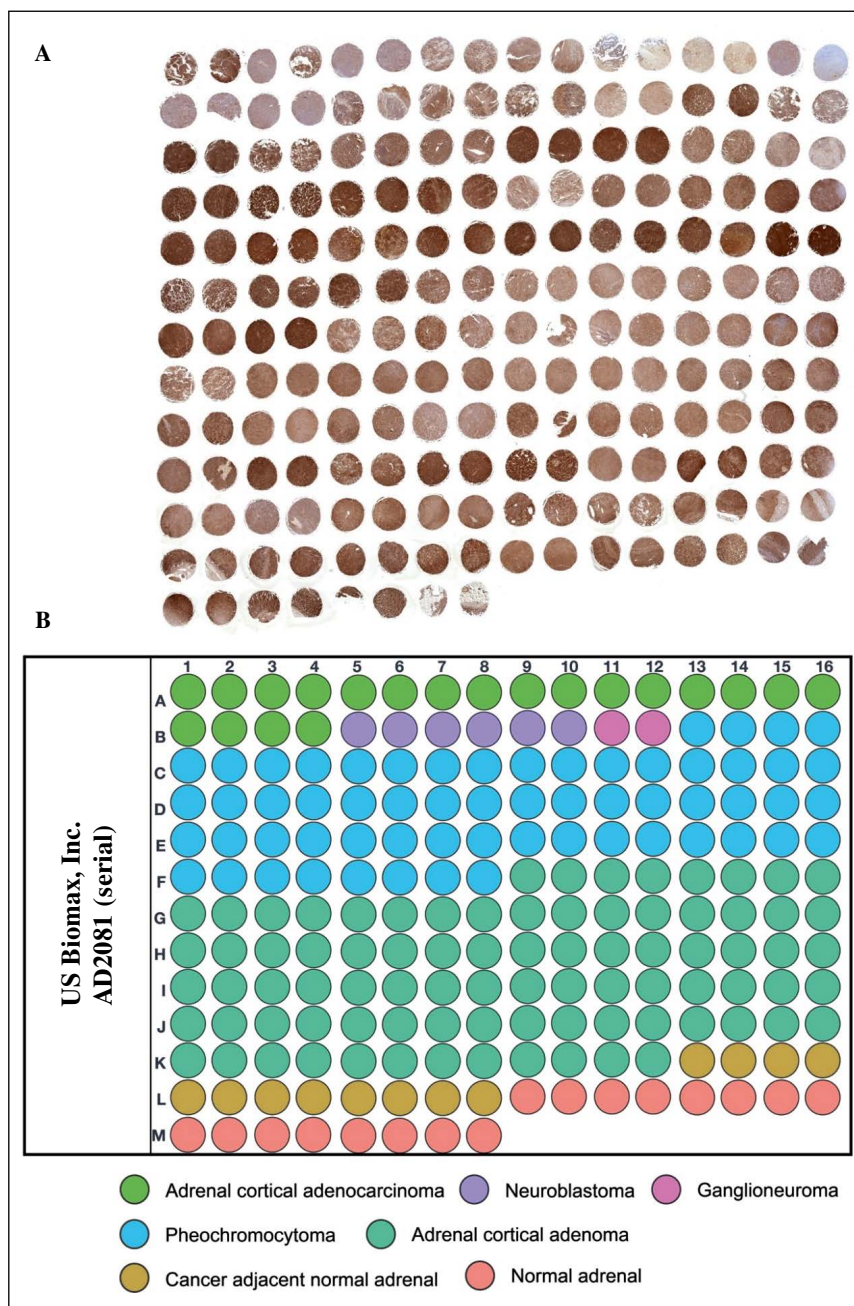
**Figure 1.** Analysis of ghrelin expression in adrenal gland disease spectrum (adrenal cancer progression) tissue microarray (TMA) slide. This histological slide contained 200 cores of adrenal gland tissue specimens, which included 20 samples of adrenocortical adenocarcinoma (ACC), 6 neuroblastoma, 2 ganglioneuroma, 60 pheochromocytoma, and 84 adrenocortical adenoma (ACA), and 12 samples of normal tissue adjacent to ACC and 16 biopsy samples of normal adrenal tissue. **A.** The general profile of the stained specimens. **B.** TMA map showing the relevant groups marked in appropriate colors.

The ROC curve analysis showed that ghrelin expression could be considered as a potential biomarker for differentiating ACC from normal adrenal tissue, and ACC from other adrenal tumors. The cut-off integrated density values used for differentiating between the compared groups were as follows: ACC *vs.* normal adrenal tissue = 91.7 (specificity 95% and sensitivity 81.2%), ACC *vs.* ACA = 82.4 (specificity 85% and sensitivity 92.9%), and ACC *vs.* pheochromocytoma = 91.7 (specificity 95% and sensitivity 90%). All the compared groups were also characterized by a high area-under-curve (AUC) value as shown in Figure 4.

## Discussion

Thus far, only a few studies have examined the expression of ghrelin in adrenal tumors [23, 27, 28]. In the study of Barzon *et al.*, as well as our previous study [27,
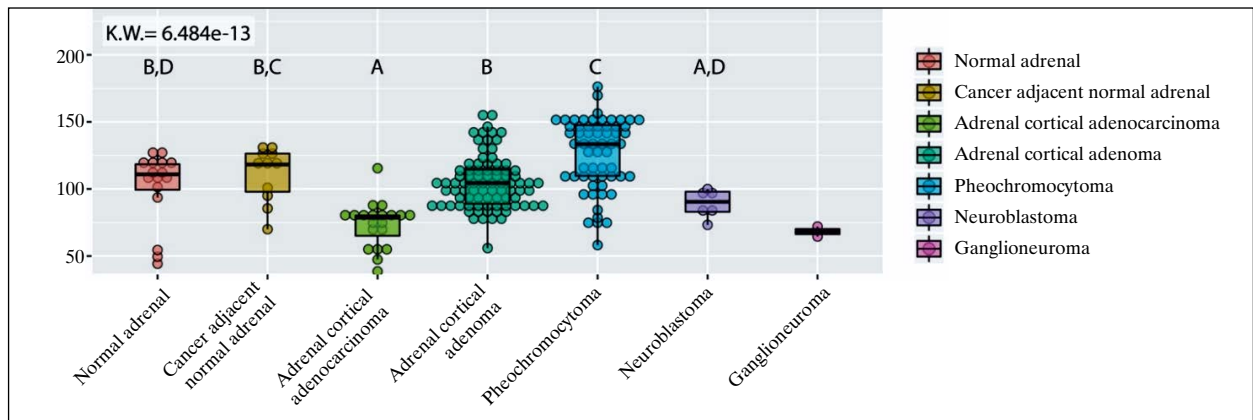
**Figure 2.** Densitometric analysis of ghrelin expression in adrenal gland disease spectrum (adrenal cancer progression) tissue array slide. Each of the groups was presented as a boxplot, with the values of median and IQR. Densitometric data from individual patients were superimposed on the appropriate boxplots and displayed as dots. Comparisons between the groups were carried out using Kruskal-Wallis followed by Dunn *post hoc* test. The differences between the groups were indicated using the letter annotation, where different letters indicate significant (p < 0.05) differences between the compared groups.
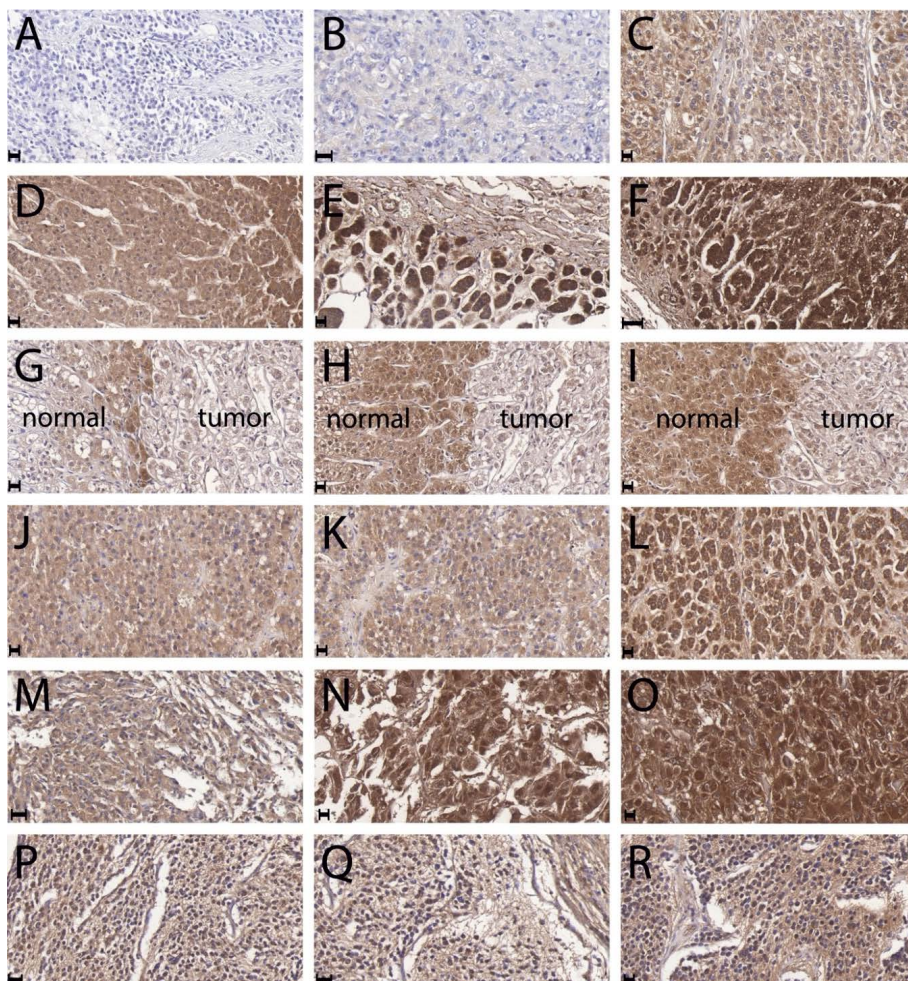


**Figure 3.** Representative images of ghrelin immunohistochemical reactivity in **(A–C)** ACC, **(D–F)** normal adrenal tissue, **(G–I)** tumor-adjacent normal tissue, **(J–L)** ACA, **(M–O)** pheochromocytoma, and **(P–R)** neuroblastoma. The left column shows the weakest expression from each group; the middle column presents the medium expression of the analyzed protein, and the right column shows the strongest expression. Abbreviations as for Figure 1. Scale bar: 20 $\mu$m.
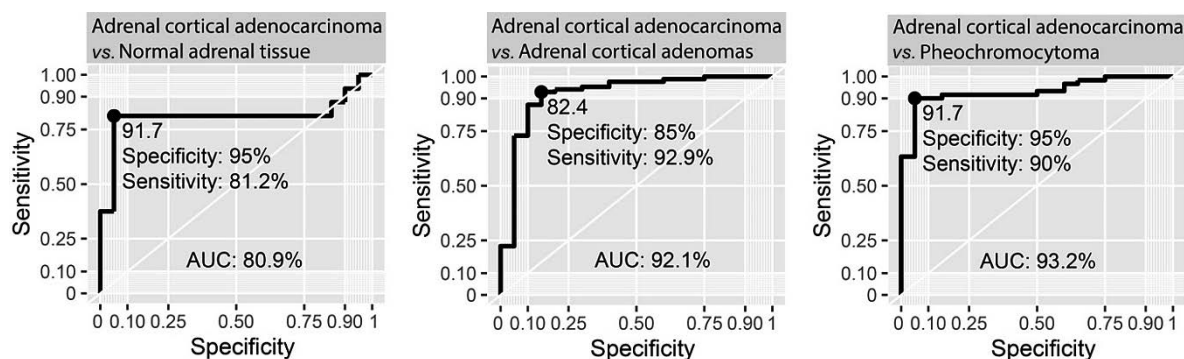
**Figure 4.** ROC analysis of the use of ghrelin immunoreactivity as a biomarker for differentiating ACC from normal adrenal tissue, ACC from ACA, and ACA from pheochromocytoma. The cut-off values used for differentiation, specificity, sensitivity, and the AUC values are shown in each of the graphs. Abbreviations as for Figure 1.

28], ghrelin expression was tested only at the mRNA level. Ueberberg *et al.* [23] investigated the expression of ghrelin at the level of both mRNA and protein in adrenal adenoma, pheochromocytoma, and healthy adrenal tissue, while Raghay *et al.* [10] studied its expression in the adrenal medulla and pheochromocytoma. To our knowledge, our present study is the first in which the expression of ghrelin at the protein level was evaluated in ACC compared with other tumors derived from the adrenal cortex or medulla. Ghrelin is synthesized in normal human adrenal glands [23]. This result was also confirmed in our current study; however, we found low immunoreactivity of ghrelin protein in ACC compared with normal adrenals, ACA, and pheochromocytoma. Based on the ROC curves, we suggest that ghrelin may serve as a potential immunohistochemical marker of ACC due to its high sensitivity and specificity. It should be noted that during the histopathological examination, the diagnosis of ACC can be very difficult. In such a scenario, ghrelin immunostaining may form a valuable prognostic marker for distinguishing malignant and aggressive ACC from benign ACA and pheochromocytoma.

Various hypotheses can be proposed to explain the low expression of ghrelin in ACC. First, there may be a mutation in the ghrelin gene that would cause disturbances in the protein expression. If the high immunoreactivity of ghrelin is assumed to be due to the presence of binding sites (*i.e.* ghrelin receptors) in the examined tissues, then the low immunoreactivity could be linked to a decrease in the number of receptors — negative feedback-based defense downregulation.

Furthermore, ghrelin acts as a stimulatory factor for adrenocortical proliferation [20–23, 28]. Therefore, it can be assumed that locally produced ghrelin could stimulate adrenal tumor cell proliferation *via*

auto or paracrine way. However, due to the low expression of ghrelin in ACC this mechanism appears unlikely.

The role of ghrelin splice variants in carcinogenesis was also previously described [29]. Different posttranslational cleavage sites of ghrelin precursor may lead to the formation of new peptides with other functions. Thus, one of the splice variants that our IHC method has not identified might be involved in the etiopathogenesis of ACC.

In our previous work [28], we evaluated the mRNA expression of ghrelin in adrenal tumors. However, our current results are quite surprising — the mRNA expression of ghrelin was the highest and the protein expression was the lowest in ACC. Furthermore, in pheochromocytomas, we found low mRNA expression, whereas the highest protein expression. Nonetheless, our results were not unpredictable. Ghelardoni *et al.* compared the gene and protein expression of ghrelin in different human tissues and observed that the protein expression was discordant with the gene expression. The authors suggested that different tissues may significantly differ in their rate of ghrelin mRNA translation or posttranslational events [11]. The regulation of posttranscriptional and translational processes and protein degradation can contribute as much to variations in protein concentration as transcription and transcript degradation [30].

Perhaps, the low expression of ghrelin protein results from the epigenetic regulation of gene expression by circulating microRNAs (miRNAs). miRNAs are small (30–32)-nucleotide noncoding RNA that act as regulators of posttranscriptional stability and/ /or translation of RNA (mRNA) [31]. Certain types of miRNAs are more expressed in ACC tissues than in ACA [31–33]. It is assumed that miRNAs might

interfere with translation or enhance the degradation of ghrelin.

Alternative splicing of preproghrelin mRNA is complicated and can lead to the formation of many variants of mRNA and, consequently, proteins. Over a dozen transcript variants of the human preproghrelin gene exist, but it is not known if they are all transcribed into protein. The lack of relationship between RNA expression and protein formation may be due to changes in processing during translation, post-translation, and protein degradation. New peptides resulting from alternative splicing may perform different functions than ghrelin. For instance, in breast cancer, the ghrelin variant In1-ghrelin was reported to be overexpressed and to promote basal proliferation in the breast cancer cell line [32]. In addition, an increase in the risk of breast cancer was associated with the polymorphisms of ghrelin gene [29].

Ghrelin gene-derived splice variants are overexpressed in breast cancer, which suggests that an imbalance in the ghrelin system's regulation may be associated with the pathogenesis of breast tumor [33]. Perhaps, a similar mechanism is involved in the development of adrenal tumors.

We can also assume that if low mRNA expression is associated with high protein levels, we are dealing with a very stable transcript, which implies that a small amount of transcripts will give us a large amount of protein. On the other hand, if there are many unstable, easily degraded transcripts, the protein level will remain low.

An additional interesting observation is the nuclear ghrelin immunostaining in ACC. Similar reactions have previously been observed in human normal and polycystic ovaries and in the rat testes [12, 34]. The authors conclude that the nuclear expression of ghrelin suggests its particular role in the intracellular regulation, where ghrelin could control the expression of other genes, acting as a specific transcription factor [35].

Thus far, no data have been published regarding the IHC analysis of ghrelin in ACC, but our observations are in line with the studies on different cancer types. Aydin *et al.* evaluated the immunoreactivity of ghrelin in gastric adenocarcinoma and mucoepidermoid carcinoma of the salivary glands. They found that negative ghrelin immunostaining can differentiate tumors from normal tissues [36]. Similarly, in renal cell carcinoma and oral squamous cell carcinoma, the ghrelin protein expression was frequently lower than that in normal tissues or was even absent [37, 38]. Ghrelin expression has also been associated with better outcomes in various malignancies. For example, patients with breast cancer expressing ghrelin have

a lower risk of death compared to those lacking ghrelin expression in tumors [33]. It seems that reduced ghrelin immunoexpression is associated with an increased risk of malignancy of some lesion.

Data on the expression of ghrelin protein in pheochromocytoma are scared. In the present study, we showed that ghrelin expression was significantly lower in ACC than pheochromocytoma. Ueberberg *et al.* investigated ghrelin expression in 43 ACA (17 functional and 16 nonfunctional) and 13 pheochromocytomas. They found that ghrelin protein was expressed in 54–87% of ACA and 0% of pheochromocytoma samples tested [23]. In turn, Raghay *et al.* evaluated the expression of ghrelin protein using two types of antibodies — goat and rabbit [10]. The authors used goat antibody to evaluate ghrelin immunoexpression in both human normal medulla and pheochromocytomas. Ghrelin immunoexpression was observed in the medulla. Chromaffin cells were immunostained with ghrelin, whereas the neurons were negative. The five human pheochromocytomas studied showed positivity for goat anti-ghrelin with focal or diffuse immunostaining patterns. The intensity of immunoreactivity varied between different tumors and also between different cells of the same tumor. However, when rabbit antibodies were used, no reaction was found in the normal medulla and pheochromocytomas. The authors suggested that the difference could be due to the fact that rabbit antibody can recognize only the mature peptide form having 28 amino acids, whereas goat antibody can detect all ghrelin forms — precursors, proghrelin, and mature form [10]. Ueberberg *et al.* used rabbit antibody while we performed tests with a goat antibody, which may be the reason for the different results observed in the case of pheochromocytomas. Both results suggest that in pheochromocytoma, mature ghrelin is not produced or is rapidly degraded. Pheochromocytoma is the only adrenal tumor in which the effect of ghrelin on the secretory activity of the tumor has been confirmed [39, 40]. Nanmoku *et al.* observed stimulatory ghrelin's effect on dopamine secretion in rat pheochromocytoma PC 12 cells [40]. It is unlikely that ghrelin directly affects the production and secretion of adrenocortical hormones [20], but some reports suggest that ghrelin stimulates dopamine secretion in pheochromocytomas [40]. The difference associated with protein expression in pheochromocytomas, may be related to its effect on dopamine secretion.

In our study, the lowest immunoexpression of ghrelin protein was noted in ganglioneuroblastoma, which might be attributed to the origin of this tumor. However, due to the small size of this group, the data

obtained are difficult to be discussed. There no data on this subject in the available literature.

In conclusion, the histopathological diagnosis of ACC is often difficult. Our research suggests that ghrelin immunoreactivity may be considered as a sensitive and specific marker for differentiating ACC from ACA and pheochromocytoma. However, further research is required to determine the causes of differential ghrelin expression in adrenal tumors.

## Financial disclosure

## Author Contribution
Conceptualization, HK, AM and Marcin R; Data curation, HK, BB, K B-R and Marek R; Formal analysis, Marcin R; Funding acquisition, AM and ZK; Investigation, HK, BB and K B-R; Methodology, HK, ZK and Marcin R; Project administration, AM and ZK; Resources, AM and ZK; Software, Marcin R; Supervision, HK, AM and Marcin R; Validation, HK, AM and Marek R; Visualization, HK, BB and K B-R; Writing — original draft, HK, BB and K B-R; Writing — review & editing, HK, AM, ZK, Marek R and Marcin R. All authors approved the version to be published and agreed to be accountable for all aspects of the work in ensuring that questions related to the accuracy or integrity of any part of the work are appropriately investigated and resolved.

## Conflicts of interest

The authors declare no conflict of interest.

## References

1. Dietrich CF, Correas JM, Dong Yi, et al. WFUMB position paper on the management incidental findings: adrenal incidentaloma. Ultrasonography. 2020; 39(1): 11–21, doi: 10.14366/usg.19029, indexed in Pubmed: 31786909.

2. Lenders JWM, Eisenhofer G. Update on modern management of pheochromocytoma and paraganglioma. Endocrinol Metab (Seoul). 2017; 32(2): 152–161, doi: 10.3803/EnM.2017.32.2.152, indexed in Pubmed: 28685506.

3. Fassnacht M, Dekkers O, Else T, et al. European Society of Endocrinology Clinical Practice Guidelines on the management of adrenocortical carcinoma in adults, in collaboration with the European Network for the Study of Adrenal Tumors. Eur J Endocrinol. 2018; 179(4): G1–G46, doi: 10.1530/EJE-18-0608, indexed in Pubmed: 30299884.

4. Aubert S, Wacrenier A, Leroy X, et al. Weiss system revisited: a clinicopathologic and immunohistochemical study of 49 adrenocortical tumors. Am J Surg Pathol. 2002; 26(12): 1612–1619, doi: 10.1097/00000478-200212000-00009, indexed in Pubmed: 12459628.

5. Duregon E, Volante M, Bollito E, et al. Pitfalls in the diagnosis of adrenocortical tumors: a lesson from 300 consultation cases. Hum Pathol. 2015; 46(12): 1799–1807, doi: 10.1016/j.humpath.2015.08.012, indexed in Pubmed: 26472162.

6. Komarowska H, Bednarek-Rajewska K, Kański M, et al. Epithelioid angiomyolipoma mimicking adrenal cortical carcinoma: A diagnostic pitfall. Oncol Lett. 2015; 10(4): 2130–2134, doi: 10.3892/ol.2015.3543, indexed in Pubmed: 26622807.

7. Komarowska H, Bromińska B, Janicka-Jedyńska M, et al. Adrenal Incidentaloma: Nothing Is Ever as It Seems. Am J Med. 2020; 133(9): 1048–1050, doi: 10.1016/j.amjmed.2019.12.039, indexed in Pubmed: 32001227.

8. Kojima M, Hosoda H, Date Y, et al. Ghrelin is a growth-hormone-releasing acylated peptide from stomach. Nature. 1999; 402(6762): 656–660, doi: 10.1038/45230, indexed in Pubmed: 10604470.

9. Ueberberg B, Unger N, Saeger W, et al. Expression of ghrelin and its receptor in human tissues. Horm Metab Res. 2009; 41(11): 814–821, doi: 10.1055/s-0029-1233462, indexed in Pubmed: 19670151.

10. Raghay K, García-Caballero T, Bravo S, et al. Ghrelin localization in the medulla of rat and human adrenal gland and in pheochromocytomas. Histol Histopathol. 2008; 23(1): 57–65, doi: 10.14670/HH-23.57, indexed in Pubmed: 17952858.

11. Ghelardoni S, Carnicelli V, Frascarelli S, et al. Ghrelin tissue distribution: comparison between gene and protein expression. J Endocrinol Invest. 2006; 29(2): 115–121, doi: 10.1007/BF03344083, indexed in Pubmed: 16610236.

12. Komarowska H, Waśko R, Iwanik K, et al. Ghrelin ovarian cell expression in patients with polycystic ovary syndrome: an immunohistochemical evaluation. Horm Metab Res. 2006; 38(12): 783–788, doi: 10.1055/s-2006-956506, indexed in Pubmed: 17163351.

13. Gnanapavan S, Kola B, Bustin SA, et al. The tissue distribution of the mRNA of ghrelin and subtypes of its receptor, GHS-R, in humans. J Clin Endocrinol Metab. 2002; 87(6): 2988, doi: 10.1210/jcem.87.6.8739, indexed in Pubmed: 12050285.

14. Andrusiewicz M, Komarowska H, Skibińska I, et al. Expression of ghrelin and ghrelin functional receptor GHSR1a in human pituitary adenomas. Pol Arch Intern Med. 2017; 127(3): 163–169, doi: 10.20452/pamw.3967, indexed in Pubmed: 28377557.

15. Komarowska H, Jaskula M, Stangierski A, et al. Influence of ghrelin on energy balance and endocrine physiology. Neuro Endocrinol Lett. 2012; 33(8): 749–756, indexed in Pubmed: 23391977.

16. Akalu Y, Molla MD, Dessie G, et al. Physiological Effect of Ghrelin on Body Systems. Int J Endocrinol. 2020; 2020: 1385138, doi: 10.1155/2020/1385138, indexed in Pubmed: 32565790.

17. Tokudome T, Otani K, Miyazato M, et al. Ghrelin and the heart. Peptides. 2019; 111: 42–46, doi: 10.1016/j.peptides.2018.05.006, indexed in Pubmed: 29791869.

18. Angel CZ, Iguacel I, Mullee A, et al. Appetite-regulating hormones-leptin, adiponectin and ghrelin-and the development of prostate cancer: a systematic review and exploratory meta-analysis. Prostate Cancer Prostatic Dis. 2020; 23(1): 11–23, doi: 10.1038/s41391-019-0154-1, indexed in Pubmed: 31147627.

19. Carraro G, Albertin G, Abudukerimu A, et al. Growth hormone secretagogue receptor subtypes 1a and 1b are ex-

pressed in the human adrenal cortex. Int J Mol Med. 2004; 13(2): 295–298, doi.org/10.3892/ijmm.13.2.295, indexed in Pubmed: 14719137.

20. Andreis P, Malendowicz L, Trejter M, et al. Ghrelin and growth hormone secretagogue receptor are expressed in the rat adrenal cortex: evidence that ghrelin stimulates the growth, but not the secretory activity of adrenal cells. FEBS Letters. 2003; 536(1-3): 173–179, doi: 10.1016/s0014-5793(03)00051-6.

21. Mazzocchi G, Neri G, Rucinski M, et al. Ghrelin enhances the growth of cultured human adrenal zona glomerulosa cells by exerting MAPK-mediated proliferogenic and antiapoptotic effects. Peptides. 2004; 25(8): 1269–1277, doi: 10.1016/j.peptides.2004.05.011, indexed in Pubmed: 15350694.

22. Delhanty PJD, van Koetsveld PM, Gauna C, et al. Ghrelin and its unacylated isoform stimulate the growth of adrenocortical tumor cells via an anti-apoptotic pathway. Am J Physiol Endocrinol Metab. 2007; 293(1): E302–E309, doi: 10.1152/ajpendo.00377.2006, indexed in Pubmed: 17405826.

23. Ueberberg B, Unger N, Sheu SY, et al. Differential expression of ghrelin and its receptor (GHS-R1a) in various adrenal tumors and normal adrenal gland. Horm Metab Res. 2008; 40(3): 181–188, doi: 10.1055/s-2007-1004574, indexed in Pubmed: 18246525.

24. Hosoda H, Kojima M, Matsuo H, et al. Purification and characterization of rat des-Gln14-Ghrelin, a second endogenous ligand for the growth hormone secretagogue receptor. J Biol Chem. 2000; 275(29): 21995–22000, doi: 10.1074/jbc.M002784200, indexed in Pubmed: 10801861.

25. Seim I, Jeffery PL, Thomas PB, et al. Multi-species sequence comparison reveals conservation of ghrelin gene-derived splice variants encoding a truncated ghrelin peptide. Endocrine. 2016; 52(3): 609–617, doi: 10.1007/s12020-015-0848-7, indexed in Pubmed: 26792793.

26. Robin X, Turck N, Hainard A, et al. pROC: an open-source package for R and S+ to analyze and compare ROC curves. BMC Bioinformatics. 2011; 12: 77, doi: 10.1186/1471-2105-12-77, indexed in Pubmed: 21414208.

27. Barzon L, Pacenti M, Masi G, et al. Loss of growth hormone secretagogue receptor 1a and overexpression of type 1b receptor transcripts in human adrenocortical tumors. Oncology. 2005; 68(4-6): 414–421, doi: 10.1159/000086983, indexed in Pubmed: 16020971.

28. Komarowska H, Rucinski M, Tyczewska M, et al. Ghrelin as a potential molecular marker of adrenal carcinogenesis: In vivo and in vitro evidence. Clin Endocrinol (Oxf). 2018; 89(1): 36–45, doi: 10.1111/cen.13725, indexed in Pubmed: 29682767.

29. Dossus L, McKay JD, Canzian F, et al. Polymorphisms of genes coding for ghrelin and its receptor in relation to anthropometry, circulating levels of IGF-I and IGFBP-3, and breast cancer risk: a case-control study nested within the European Prospective Investigation into Cancer and Nutrition (EPIC).

Carcinogenesis. 2008; 29(7): 1360–1366, doi: 10.1093/carcin/bgn083, indexed in Pubmed: 18375957.

30. Vogel C, Marcotte EM. Insights into the regulation of protein abundance from proteomic and transcriptomic analyses. Nat Rev Genet. 2012; 13(4): 227–232, doi: 10.1038/nrg3185, indexed in Pubmed: 22411467.

31. Ambros V. The functions of animal microRNAs. Nature. 2004; 431(7006): 350–355, doi: 10.1038/nature02871, indexed in Pubmed: 15372042.

32. Gahete MD, Córdoba-Chacón J, Hergueta-Redondo M, et al. A novel human ghrelin variant (In1-ghrelin) and ghrelin-O-acyltransferase are overexpressed in breast cancer: potential pathophysiological relevance. PLoS One. 2011; 6(8): e23302, doi: 10.1371/journal.pone.0023302, indexed in Pubmed: 21829727.

33. Grönberg M, Nilsson C, Markholm I, et al. Ghrelin expression is associated with a favorable outcome in male breast cancer. Sci Rep. 2018; 8(1): 13586, doi: 10.1038/s41598-018-31783-x, indexed in Pubmed: 30206250.

34. Łukaszyk A, Rafińska L, Sawiński P, et al. Immunohistochemical and hybridocytochemical study on ghrelin signalling in the rat seminiferous epithelium. Folia Histochem Cytobiol. 2009; 47(3): 415–423, doi: 10.2478/v10042-009-0097-9, indexed in Pubmed: 20164026.

35. Buyse J, Janssen S, Geelissen S, et al. Ghrelin modulates fatty acid synthase and related transcription factor mRNA levels in a tissue-specific manner in neonatal broiler chicks. Peptides. 2009; 30(7): 1342–1347, doi: 10.1016/j.peptides.2009.04.015, indexed in Pubmed: 19409434.

36. Aydin S, Ozercan IH, Dagli F, et al. Ghrelin immunohistochemistry of gastric adenocarcinoma and mucoepidermoid carcinoma of salivary gland. Biotech Histochem. 2005; 80(3-4): 163–168, doi: 10.1080/10520290500387847, indexed in Pubmed: 16298902.

37. Dagli AF, Aydin S, Karaoglu A, et al. Ghrelin expression in normal kidney tissue and renal carcinomas. Pathol Res Pract. 2009; 205(3): 165–173, doi: 10.1016/j.prp.2008.10.002, indexed in Pubmed: 19054628.

38. Alnema MM, Aydin S, Ozkan Y, et al. Ghrelin and obestatin expression in oral squamous cell carcinoma: an immunohistochemical and biochemical study. Mol Cell Biochem. 2010; 339(1-2): 173–179, doi: 10.1007/s11010-009-0381-1, indexed in Pubmed: 20047070.

39. Obara-Moszyńska M, Kedzia A, Chmielnicka-Kopaczyk M. Expression of ghrelin in human fetal adrenal glands and paraadrenal nerve ganglions. Folia Histochem Cytobiol. 2009; 47(1): 25–28, doi: 10.2478/v10042-009-0023-1, indexed in Pubmed: 19419933.

40. Nanmoku T, Takekoshi K, Ishi K, et al. Effect of Ghrelin on catecholamine secretion in rat pheochromocytoma PC12 cells. Endocr Res. 2003; 29(1): 17–21, doi: 10.1081/erc-120018673, indexed in Pubmed: 12665315.

ORIGINAL PAPER

**VM**
**VIA MEDICA**

# Does repeated gold-nanoparticles administration affect pars distalis hormonal and folliculo-stellate cells in adult male albino rats?

Abeer Ibraheem Omar[1], Samaa Samir Kamar[1, 2]

[1]Department of Histology and Cell Biology, Faculty of Medicine, Cairo University, Cairo, Egypt

[2]Department of Histology, Armed Forces College of Medicine, Cairo, Egypt

**Abstract**

**Introduction.** Worldwide, nanoparticles especially gold-nanoparticles (Au-NPs) are widely used in medicine, cancer treatment and cosmetic industry. They are easily conjugated with different biomedical and biological agents and effortlessly absorbed with few side effects. The pars distalis of the pituitary gland is considered as the maestro of the endocrine peripheral glands since it secrets trophic hormones that controls their functions. 5–10% of the non-granular pars distalis cells are folliculo-stellate cells (FSCs) that support the granular cells' functions. The aim of the study was to explore the histological and the biochemical effects of repeated exposure to Au-NPs on the pars distalis in adult male albino rats with highlighting the impact on FSCs.

**Material and methods.** Thirty-six adult male albino rats were divided equally into control group and Au-NPs group (received 40 $\mu$g/kg/day of 11 $\pm$ 2 nm spherical Au-NPs orally for 2 weeks). Then, rats were euthanized and deposition of Au-NPs in pars distalis was investigated. Biochemical investigations and histological studies including hematoxylin and eosin staining, periodic acid Schiff's reaction, immunohistochemistry (IHC) for S-100, connexin 43 (Cx43) and Cytochrome-C (Cyt-C) as well as electron-microscopic and morphometric studies were carried out.

**Results.** The Au-NPs group demonstrated structural disorganization in the pars distalis, inflammation, congestion and increased extracellular PAS-positive colloid deposition due to the accumulation of Au-NPs. A significant increase in the immunoreactivity of S-100, Cx43 and Cyt-c, along with a significant increase in TNF-$\alpha$, MDA, and bFGF content in the pituitary homogenates, was noted as compared to the control group. Ultrastructurally, degenerative changes were observed in the secretory cells. FSCs showed proliferation and increased phagocytic activity.

**Conclusions.** Repetitive exposure of adult male albino rats to Au-NPs prompted the accumulation of these nanoparticles in the pars distalis that was accompanied by cellular degeneration and dysfunction of the secretory cell and proliferation of FSCs. Thus, monitoring of the pars distalis hormonal levels might be useful for early detection of some hazardous effects possibly associated with the use of gold-nanoparticles. (*Folia Histochemica et Cytobiologica 2021, Vol. 59, No. 2, 95–107*)

**Key words:** gold-nanoparticles; rat; pars distalis; folliculo-stellate cells; connexin 43; cytochrome-c; IHC; electron microscopy

**Correspondence address:** Samaa Samir Kamar
Department of Histology and Cell Biology,
Faculty of Medicine, Cairo University, El Manial,
11559, Cairo, Egypt
phone: +02 01008909069
e-mail: Dr_samaakamar@yahoo.com

## Introduction

Nanoparticles are materials that are naturally present or can be engineered from carbon or other elements like silver and gold. They have characteristic tiny sizes (less than 100 nanometers) with high surface

area to volume ratio. Such unique minute size gives them physical, electrical and optical properties. So, they are widely used in different industries like cosmetics, beverages and food packaging [1]. Moreover, their ability to enter the mammalian body through inhalation, ingestion or cutaneous absorption was proved [2]. As well, they are capable of modifying the drugs' pharmacokinetics and pharmacodynamics affecting the distribution of the drugs in different tissues [3].

Among the nanoparticles, gold nanoparticles (Au-NPs) are widely used for labelling, imaging (pacemakers and stents), implants and delivery in medicine, pharmacy and cosmetic industry [4, 5]. In addition, Au-NPs are promisingly used as a vehicle for the chemotherapeutic agents in the treatment of cancers for better targeting of the cancer cells and use of smaller chemotherapies' doses with fewer side effects [6]. Moreover, Au-NPs are used in photothermolysis of cancer cells [7]. Furthermore, they can be utilized to spot and limit growth of certain microorganisms [8] and to be formulated in vaccines for certain diseases depending on their adjuvant characteristics and induction of a humoral immune response [9]. The wide use of Au-NPs depends on their unique ability to be conjugated with various types of biological, biophysical and biomedical agents such as drugs, vaccines, proteins, DNA, RNA and others [2]. Additionally, they can be absorbed easily with fewer hazardous effects than other nanoparticles [10] and can control the drug release inside the target cells [11].

It was previously documented that single and repeated systemic administration of the nanoparticles is followed by their presence in large amounts in liver and spleen and in small quantities in other organs such as brain, heart, lungs, and kidneys [12, 13]. As well, repeated oral intake and intraperitoneal injections of Au-NPs was recorded to be followed by its appearance in numerous mice tissues [12]. Of note, the matter of safety of these nanoparticles becomes an important health issue that can should be first resolved based on *in vivo* experiments.

The pituitary gland, the master endocrine gland, is considered as an intermediate body between hypothalamus and peripheral endocrine organs [14]. It is divided into two parts, the adenohypophysis that comprises the pars distalis, pars intermedia and pars tuberalis and the neurohypophysis that includes the pars nervosa, infundibular stem and median eminence. The pars distalis occupies the major part of the gland (70%) where it synthesizes and secretes trophic hormones that control the function of peripheral endocrine glands and other cell types [15].

The pars distalis cells are divided into hormonal (granular) and non-hormonal (agranular) cells, each representing about 50% of the total cell number. The hormonal cells, also called chromophils, are classified into acidophils and basophils (40% and 10% of the pars distalis cells, respectively) [16]. The acidophils are of two types: somatotrophs secrete growth hormone (GH) and mammotrophs secrete prolactin (PRL). The basophils comprise thyrotrophs secreting thyrotropin-stimulating hormone (TSH), gonadotrophs secreting follicle-stimulating hormone (FSH) and luteinizing hormone (LH) and corticotrophs secreting mainly adrenocorticotropin (ACTH) and to lesser extent melanotropin (MSH) and lipotropin (LPH) [17].

The non-hormonal cells, also called chromophobes, include the recently degranulated cells, the actively hormone-secreting cells or folliculo-stellate cells (FSCs) which represent 5–10% of all anterior pituitary cells [18]. FSCs are star-shaped cells that surround colloid-filled follicles representing cellular debris. Their processes interdigitate with the hormonal cells contacting them and the other FSCs *via* gap junctions [19]. Thus, they were proved to support the endocrine cells and are thought to maintain their functions through paracrine secretion of interleukin-6 (IL-6) and growth factors: vascular endothelial growth factor (VEGF) and basic fibroblast growth factor (bFGF). Moreover, they probably participate in the control of the transport of the hypothalamic stimulatory and inhibitory factors to the pituitary secretory cells and the conveyance of the hormonal products of these cells to the peripheral tissues. The FSCs have phagocytic ability for the cellular debris and apoptotic bodies of the endocrine cells and can act as stem cells for these cells [14, 18].

Most of the studies tracked the effect of systemic administration and distribution of NPs in liver, spleen, lung, kidney, heart, and brain after repeated doses [4, 12]. However, for our knowledge, the distribution and the potential consequences associated with the Au-NPs on the pars distalis of the pituitary gland during their clinical application and drug-delivery have not been examined before despite its major role in the control of endocrine homeostasis. Thus, this work was carried out to explore the histological and the biochemical effects of repeated oral Au-NPs administration on the pars distalis of the pituitary gland (the endocrine regulator) in adult male albino rats with special emphasis on FSCs.

## Materials and methods

**Materials.** Citrate capped-gold nanoparticles (Au-NPs) was purchased from Nano Tech Egypt for Photo-Electronics (6th

October City, Egypt) as a purple solution of 200 μg Au-NPs/ml of sodium citrate. The following primary rabbit polyclonal antibodies were used: anti- S-100 (Cat. No. ab11428, Abcam, Branford, CT, USA), anti-connexin43 (anti-Cx43) (Cat. No. bs-0651R, Bioss Antibodies Inc., Woburn, MA, USA), anti-Cytochrome-C (anti-Cyt-C) (Cat. No. ab90529, Abcam).

**Animals.** Thirty-six adult male Wistar albino rats (~200 g) were used in this study. They were housed in the laboratory animal house unit, Faculty of Medicine, Cairo University, Cairo, Egypt, and treated according to the guidelines granted by the Institutional Animal Care and Use Committee (IACAUC), Cairo University, Cairo, Egypt (Approval No. CU-III-F-48-20). The rats were kept under the same environmental conditions (ordinary rat chow and water ad libitum, 24 ± 1°C and normal light//dark cycle) for 48 hours before starting the experiment to acclimatize to the new environmental conditions and relief any kind of stress.

**Experimental design.** The rats were equally divided into two groups, 18 rats each:
**Group I** (control group): the animals were subdivided into two subgroups (9 rats each): group Ia: received no treatment (control group) and group Ib: each rat received a single oral daily dose of 1 ml sodium citrate *via* a gastric tube for two weeks (sham-operated group).
**Group II** (Au-NPs group): each rat was given a daily oral dose of Au-NPs (40 μg/kg/day) from the purchased solution in 1 ml sodium citrate, *via* a gastric tube for two weeks [20].

**Citrate capped-gold nanoparticles preparation.** Au-NPs were prepared according to previously described methodology [21]. This occurred by citrate reduction of $Au^{3+}$ ions in chloroauric acid ($HAuCl_4$) to neutral citrate capped gold atoms. By the increase in gold atoms formation, the solution came to be supersaturated and the gold atoms were increasingly precipitated in the form of sub-nanometer particles. Filtration of the citrate capped Au-NPs colloidal solution was done through 0.45 μm Millipore syringe filters and the filtrate was kept at pH 7 using NaOH diluted solution ($10^{-7}$ M) and then stored at 4°C.

Ten ml of a prepared 1 nM of citrate-capped Au-NPs in 1 L of NaOH solution were centrifuged at 13,500 rpm for 10 min. The resultant pellet was then re-suspended in 1.2 mM sodium citrate to prepare a solution of 200 μg Au-NPs/ml. Spectrophotometry and transmission electron microscopy (TEM) were used to identify the Au-NPs. By spectrophotometry, the Au-NPs revealed strong light absorption in the visible region of the optical spectrum with a maximum absorbance at 520 nm [4]. JEOL JEM-2100 microscope (Jeol, Tokyo, Japan) was utilized at high resolution at 200 kV to clarify the shape and the size of Au-NPs (Fig. 1A, B).
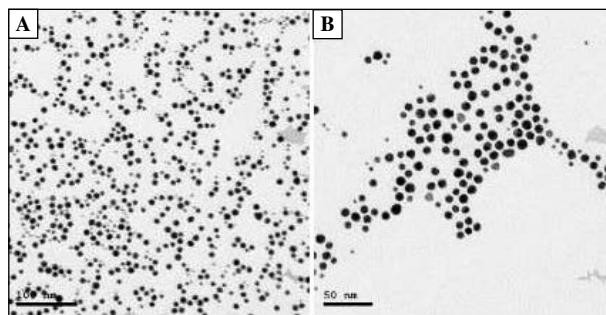


**Figure 1 A, B.** Ultrahigh magnification of TEM images of citrate capped gold nanoparticles (NanoTech Egypt for Photo-Electronics, Egypt) (Scale bars 100 and 50 nm).

Statistical analysis of the Au-NPs size was done by measuring the core diameter of 200 particles from different micrographs at high magnification, mainly at 50000×. The mean size (± SD) of the synthesized Au-NPs were 11 ± 2 nm spherical particles.

**Sample collection.** After 2 weeks in the animal house, blood samples were collected from tail veins and delivered to centrifuge tubes to be centrifuged for 20 min. The serum was separated from the samples and stored at 4°C for further use.

All rats were euthanized using intraperitoneal injection of ketamine (90 mg/kg)/xylazine (15 mg/kg). Then, the animals of each control group (Ia and Ib) and Au-NPs group were equally divided into 3 sets (*i.e.* each set had 3 rats from each control subgroup and 6 rats from Au-NPs group). The rats of the first and the second sets were perfused intracardially by 10% formol saline while the rats of the third set were perfused by 2.5% glutaraldehyde at 4°C. The skulls were opened and the pituitary glands were dissected. The pituitary glands of the 1st set were used for measuring the accumulated Au-NPs and the biochemical investigations, those of the 2nd set were used for the preparation of paraffin blocks and those of the 3rd set were used for the preparation of resin blocks for TEM.

**Measurement of Au-NPs accumulation by Inductively Coupled Plasma Mass Spectrometry (ICP-MS).** Measurements of the content of Au-NPs in the pituitary glands were done at the National Institute of Laser Enhanced Sciences, Cairo University, Cairo, Egypt, using ICP-MS technique [22]. Concisely, the whole collected wet gland was heated at 50°C in 75% $HNO_3$ overnight (the volume of the acid was 10 times the volume occupied by the gland). Dilution of the digested product (200 times) with deionized water followed by its overnight storage at 50°C was done. Filtration using a 0.45 μm filter was accomplished before analysis in ICP-MS (Perkin Elmer: Elan 6100, PerkinElmer Inc., Wellesley, MA, USA).

**Biochemical investigations.** *Serum hormones levels.* At the Biochemistry Department, Faculty of Medicine, Cairo University, Cairo, Egypt, prolactin (PRL), LH and FSH were measured in the serum using rat-specific ELISA kits (MBS727546, MBS2509833, and MBS2021901, respectively; MyBioSource, San Diego, CA, USA). Values were expressed as mlU/mL and ng/mL.

***Pituitary homogenates and Enzyme-Linked ImmunoSorbent Assay (ELISA).*** Homogenates of the pituitary glands were prepared in a following way. The whole glands of each group were divided into segments, which were homogenized in 10% ice-cold phosphate-buffered saline (PBS, pH 7.4) for 10 min in a glass manual homogenizer. The homogenate was centrifuged at 10,000 *g* for 20 min at 4°C. The resulting supernatant was used for ELISA according to the manufacturer's instructions of each kit data sheet to measure the content of (i) Tumor necrosis factor-$\alpha$ (TNF-$\alpha$) and (ii) B cell lymphoma-2 (Bcl-2) using ELISA kits supplied by Abcam (ab100785 & ab227899, respectively). The content of malondialdehyde (MDA), catalase, and bFGF was measured using ELISA kits supplied by MyBioSource (MBS738685, MBS765803 & MBS2509327, respectively). Values were expressed *per* mg protein.

**Histological studies.** *Light microscopic studies.* The paraffin blocks of the pituitary glands in the 2nd set of animals were cut in 6 $\mu$m-thick sections and stained with hematoxylin and eosin (H&E) and by Periodic Acid Schiff's (PAS) reaction [23].

***Immunohistochemistry.*** The immunohistochemical stainings were performed to detect: (i) S-100 protein, a marker for FSCs that appears as a cytoplasmic and/or a nuclear reaction; (ii) Connexin 43 (Cx43), a marker for FSCs gap junctions that appears at the site of connexin43 protein, and (iii) Cytochrom-C (Cyt-C), a marker for apoptosis that appears as a cytoplasmic reaction in the apoptotic cells.

Immunostaining using avidin-biotin technique was carried out as described previously [24]. In short, antigen was retrieved by boiling slides for 10 min in 10 mM citrate buffer pH 6 (Cat. No. 005000, Thermo Fisher Scientific, Waltham, MA, USA). Sections were left to cool for 20 min at room temperature, then they were incubated overnight with the primary antibodies in a humidity chamber using the following dilutions: 1:50 for anti-S100, 1:200 for anti-Cx43; and 1 $\mu$g/ml for anti-Cyt-C. Immunostaining was completed using Ultravision One Detection System (Cat. No. TL-060-HLJ, Thermo Fisher Scientific). Counterstaining was carried out using Lab Vision Mayer's hematoxylin (Cat. No. TA-060-MH, Thermo Fisher Scientific). Negative control sections were prepared by the same process after omitting the primary antibodies.

***Electron microscopy.*** The sectioning, staining and examination of the ultrathin sections were carried out at the Electron Microscopy Unit, Faculty of Agriculture, Cairo University, Cairo, Egypt. The pituitary glands of the 3rd set of rats were cut into small fragments (0.5–1.0 mm³), prefixed in 2.5% glutaraldehyde for 2 h then post-fixed in 1% osmium tetroxide in 0.1 M phosphate buffer at pH 7.4 and left at 4°C for 2 h. Dehydration in ascending grade of ethanol then propylene oxide, as a solvent for resin infiltration, were used. The gradual introduction of the liquid resin was followed by embedding in epoxy resin to obtain resin blocks. Ultrathin (60–90 nm) sections were cut using a Leica Ultracut ultramicrotome (Glienicker, Berlin, Germany). They were stained with uranyl acetate followed by lead citrate and examined by TEM JEOL JEM-1400 (Jeol).

FSCs and their processes were digitally colored blue, using Adobe Creative Cloud Photoshop CC 2020 (Adobe Inc., San Jose, CA, USA), for their proper recognition.

**Morphometry.** Serial non-overlapping fields, at a magnification of 200×, from each group were used to measure the mean area percent (%) of PAS positive reaction and S-100, Cx43 and Cyt-C immunoreactivity. Leica Qwin-500 LTD-software image analysis computer system (Leica, Cambridge, UK) was used for image analysis.

**Statistical analysis.** The morphometric and biochemical measurements were expressed as mean ± standard deviation (SD) and were analyzed with Statistics for Windows SPSS version 21 software (IBM Corp., New York, NY, USA) using *t*-test for independent-samples. The results were considered statistically significant when the P-value was < 0.05.

## Results

No deaths or abnormal behaviors were observed in any of the experimental animals. Since similar histological and biochemical results were found in the two control subgroups, they were collectively called control group (group I).

### Content of Au-NPs in the pituitary
The ICP-MS revealed complete absence of Au-NPs in the pituitary glands of control group; however, in the Au-NPs group, their mean content was 0.17 ± 0.02 mg/L of the solution prepared for ICP-MS.

### Biochemical results
Serum hormones levels. Group II revealed a significant decrease in the mean values of serum PRL, LH, FSH, and the tissue Bcl-2 when compared to control group (Table 1).

**Table 1.** The serum levels of LH, FSH, PRL, TNF-$\alpha$, Bcl-2, MDA, bFGF and catalase measured by ELISA (mean ± SD)

| Parameters/Groups | Control | Au-NPs |
|---|---|---|
| LH [mIU/mL] | 19.3 ± 1.1 | 10.1 ± 0.9* |
| FSH [ng/mL] | 52.4 ± 3.5 | 39.8 ± 1.8* |
| PRL [ng/mL] | 8.2 ± 0.9 | 5 ± 1* |
| TNF-$\alpha$ [pg/mg protein] | 14.1 ± 1.3 | 68.7 ± 3.6* |
| Bcl-2 [pg/mg protein] | 192.5 ± 6.6 | 101.9 ± 5.7* |
| MDA [nmol/mg protein] | 26.3 ± 1.4 | 113.9 ± 4.2* |
| Catalase [mIU/mg protein] bFGF [pg/mg protein] | 108.2 ± 3 38.5 ± 2.1 | 115.4 ± 2.8 92.7 ± 2.9* |

*Significantly different from the control group, $p < 0.05$, n = 6

Pituitary homogenate ELISA results revealed a significant increase in the mean content of TNF-$\alpha$, MDA, and bFGF and no change in the mean value of catalase *versus* group I (Table 1).

### Morphological changes and cellular apoptosis in the pars distalis of Au-NPs group

Examination of the H&E-stained control pituitary sections revealed normal histological architecture where the gland showed pars distalis, pars intermedia and pars nervosa (Fig. 2A). The hypophyseal cleft was present between the pars distalis on one side and the pars intermedia and nervosa on the other side (Fig. 2B).

The pars distalis parenchyma was made of irregular cords of cells with capillaries in-between. These cells include chromophobes or chromophils. The chromophobes were pale polyhedral cells with central rounded vesicular nuclei. The basophils seemed fewer than acidophils and had basophilic cytoplasm and rounded vesicular nuclei whereas the acidophils were more abundant and smaller in size than basophils. They had acidophilic cytoplasm and rounded vesicular nuclei (Fig. 2C).

In the Au-NPs group, the pars distalis H&E-stained sections revealed structural disorganization and intensive cellular damage (Fig. 2D). Most of the cells were shrunken with deeply eosinophilic cytoplasm. Additionally, the nuclei appeared shrunken, darkly stained and some of them demonstrated chromatin margination or fragmentation (Fig. 2E). Moreover, there were mononuclear inflammatory cell infiltration and dilated congested blood vessels with extra-vascular exudation (Fig. 2F).

### Decreased PAS-reactivity in basophils and increased extracellular colloid PAS-reactivity in Au-NPs-treated rats

There was positive intracellular PAS reaction in the control group sections demonstrating the basophils (Fig. 2G). Moreover, extracellular positive PAS reaction was detected in rounded or oval masses (colloid) between the cells (Fig. 2G). In group II sections, the intracellular reaction was severely diminished while the extracellular reaction became more obvious (Fig. 2H). However, there was no change in the mean area percent of PAS reaction in Au-NPs group in comparison to the control group (Fig. 2I).

### Increased proliferation of FSCs in Au-NPs group

Sections of the pars distalis control group showed S-100 positive immunoreaction in the FSCs and their processes. These cells appeared encircling follicles which were faintly immunoreactive. In addition, their processes extended in-between the surrounding secretory cells (Fig. 3A). Such positive reaction was radically increased in group II with statistically significant increase in its mean area percent as compared to the control rats (Fig. 3B, C).

### Increased distribution of gap junctions in the anterior pituitary of Au-NPs group

The Cx43 positive immunoreactivity detected in the control sections (Fig. 3D) became widely spread in the sections of Au-NPs treated rats with significantly increase mean area percent (Fig. 3E, F).

### Increased apoptosis in adenohypohysis of rats treated with Au-NPs

Cells with Cyt-C positive immunoreactivity were few in the control sections (Fig. 3G). However, in Au-NPs sections, Cyt-C immunoreaction was abundantly widespread with statistically significant increase in its mean area percent in Au-NPs group *versus* the control group (Figs. 3H, I).

### Increased immunoreactivity of connexin 43 in Au-NPs group

The Cx43 positive immunoreaction detected in the control sections (Fig. 3D) became widely spread in the sections of part distalis of Au-NPs treated rats with a statistically significant increased mean area percent (Fig. 3E, F).

### Increased number of apoptotic cells in Au-NPs group

Cells with Cyt-C immunoreactivity were few in the anterior pituitary of control rats (Fig. 3G). However, in rats treated with Au-NPs sections, the Cyt-c immunereaction was abundantly widespread with

**Figure 2.** Photomicrographs of H&E stained pituitary sections. The pituitary glands in the control group (**A**, **B**, **C**) presented with the normal tissue architecture demonstrating pars distalis (PD) on the left and right sides and pars intermedia (PI) & pars nervosa (PV) in the middle (A), and at the higher magnification the hypophyseal cleft (HC) between PD and PI (B). At (C) the pars distalis shows blood capillaries (BC) between cellular cords of chromophobes (P), acidophils (A) and basophils (B). All the cell types reveal rounded vesicular nuclei (v). The pituitary of rats in the Au-NP group (**D**, **E**, **F**) demonstrates disturbed architecture (D). In (E) there are visible shrunken cells with deeply eosinophilic cytoplasm (curved arrow) as well as cells with shrunken nuclei (n). In (F) inflammatory cell infiltration (In) and dilated congested vein (cv) with extra-vascular exudation (E) are noticed. Photomicrographs of PAS reaction in the pars distalis are shown in (**G**) and (H). In the control group (G), numerous positive intracellular reaction products (bifid arrow) are present in the basophils and extracellular reaction (arrowheads) are visible in the colloid. The cells of pars distalis of the Au-NP group (**H**) show diminished intracellular reaction (bifid arrow) and increment of the extracellular reaction (arrowhead). (**I**) The mean area percent of PAS reaction in pars distalis of the pituitary glands. Data are presented as mean ± SD (n = 6 for each group). Magnifications: (A) 40×; (B, D) 100×; (C, E, F, G, H) 400×.

statistically significant increased mean area percent *versus* the control group (Figs. 3H, I).

### Ultrastructure the of the pars distalis cells of control rats

Control group sections (Fig. 4A–F) revealed the presence of secretory and non-secretory cells presenting euchromatic nuclei with prominent nucleoli. Mammotrophs contained relatively large secretory granules of variable size (Fig. 4B). The somatotrophs (Figs. 4C and 4D) showed cisternae of rough endoplasmic reticulum (rER), multiple mitochondria and relatively abundant large scattered dense secretory granules. The corticotrophs (Fig. 4E) appeared as low electron dense stellate-shaped cells with the cytoplasm demonstrating few rER cisternae, mitochondria and small granules alongside the cell membrane. Furthermore, the gonadotrophs (Fig. 4E) were shown with rounded secretory granules of variable size and density located at the pole of the cells. Thyrotrophs (Fig. 4F) displayed rER, mitochondria and the smallest secretory granules among all secretory cells.
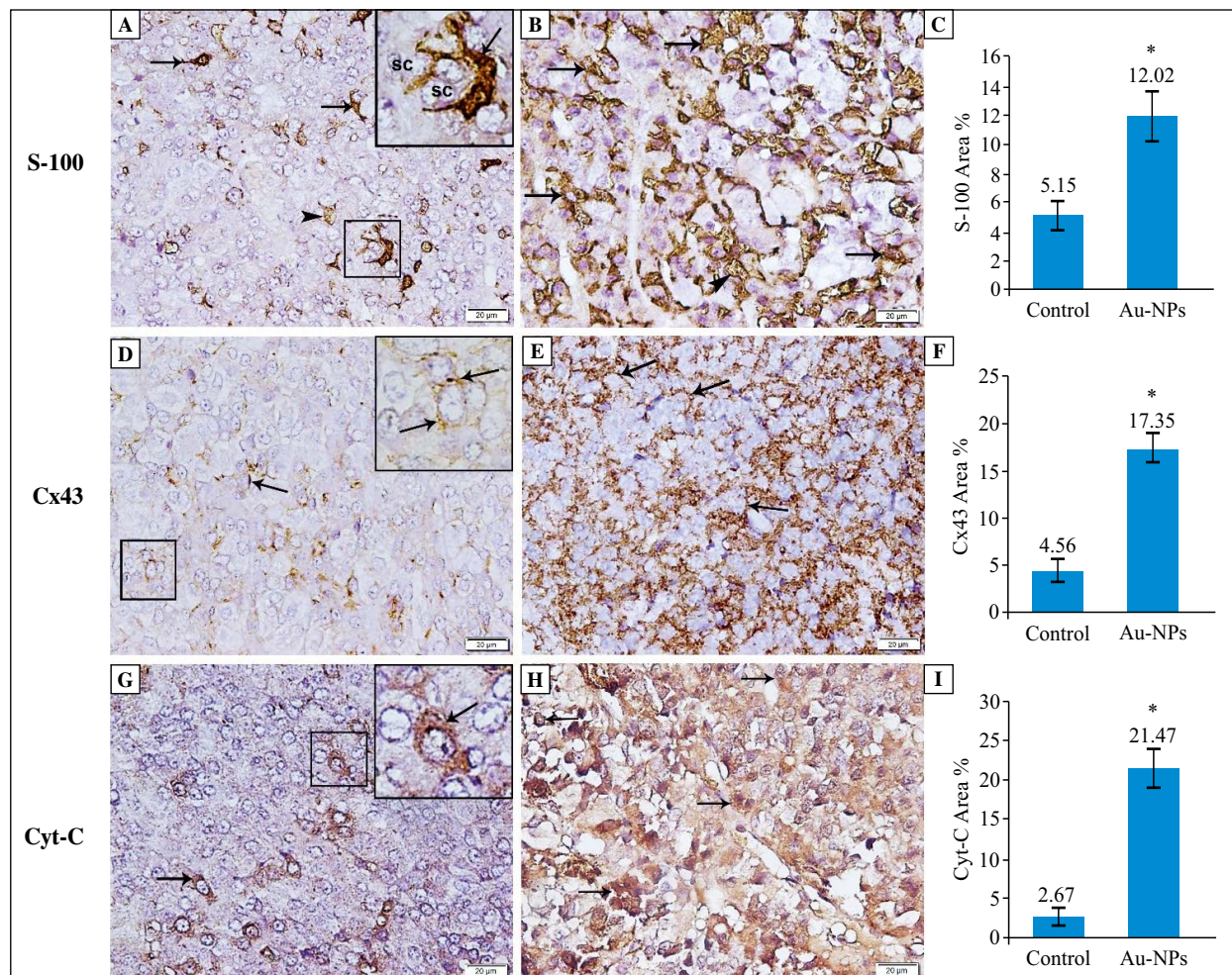
**Figure 3.** Photomicrographs of immunohistochemistry in the pars distalis sections for S-100, Cx43 and Cyt-C. Anti-S-100 immunohistochemistry: The pituitary glands of rats in the control group (**A**) show some cells demonstrating positive immunoreaction (arrow) in the cytoplasm, the nuclei and the processes of FSCs which surround cell follicles. A faint positive immunoreaction is noted in the follicular colloid (arrowhead). The right up inset: a higher magnification of the boxed area illustrates a follicle, FSCs (arrow) and their processes extended between the secretory cells (sc). The pituitary glands of rats in the Au-NP group (**B**) reveal marked increase in the positive FSCs (arrow) and colloid (arrowhead) immunoreaction. Anti-Cx-43 immunohistochemistry: The control group (**D**) displays some FSCs and their processes illustrate positive immunoreaction (arrow). The right inset: a higher magnification of the boxed area illustrates the reaction in the FSCs processes in-between the secretory cells. The Au-NP group (**E**) shows widely spread positive immunoreaction (arrow). Anti-Cyt-c immunohistochemistry: The control group (**G**) shows few cells with positive cytoplasmic immunoreaction (arrow). The upper right inset: a higher magnification of the boxed area illustrating the cytoplasmic reaction (arrow) in a hormonal cell. The Au-NP group (**H**) displays abundant positive immunoreaction (arrow). (**C, F, I**) The mean area percent of S-100, Cx43 and Cyt-C immunoreactivity, respectively. Data are presented as mean ± SD (n = 6, for each group). *significantly different from control, $p < 0.05$. Magnifications: A, B, D, E, G and H: 400×; Insets: 1000×.

The FSCs in the control group (Figs. 4A–C) were demonstrated as star-shaped cells with ovoid euchromatic nuclei, non-granular cytoplasm with electron-dense bodies (assumed to be lysosomes). They lined small follicles. The lumens of these follicles were surrounded by junctional complexes (Fig. 4D). These follicular lumens were filled with electron-lucent colloid. The processes of these cells were stretched between the secretory cells and extended to the blood capillaries. Gap junctions were visualized between the FSCs and between them and the secretory cells (Fig. 4D and 4F).

***Ultrastructural degenerative changes in the secretory cells of pars distalis in rats treated with Au-NPs are accompanied by increased activity of FSCs***

In the pars distalis of rats treated with AU-NPs (Figs. 5A–F), it was difficult to differentiate between various types of secretory cells as they all revealed features
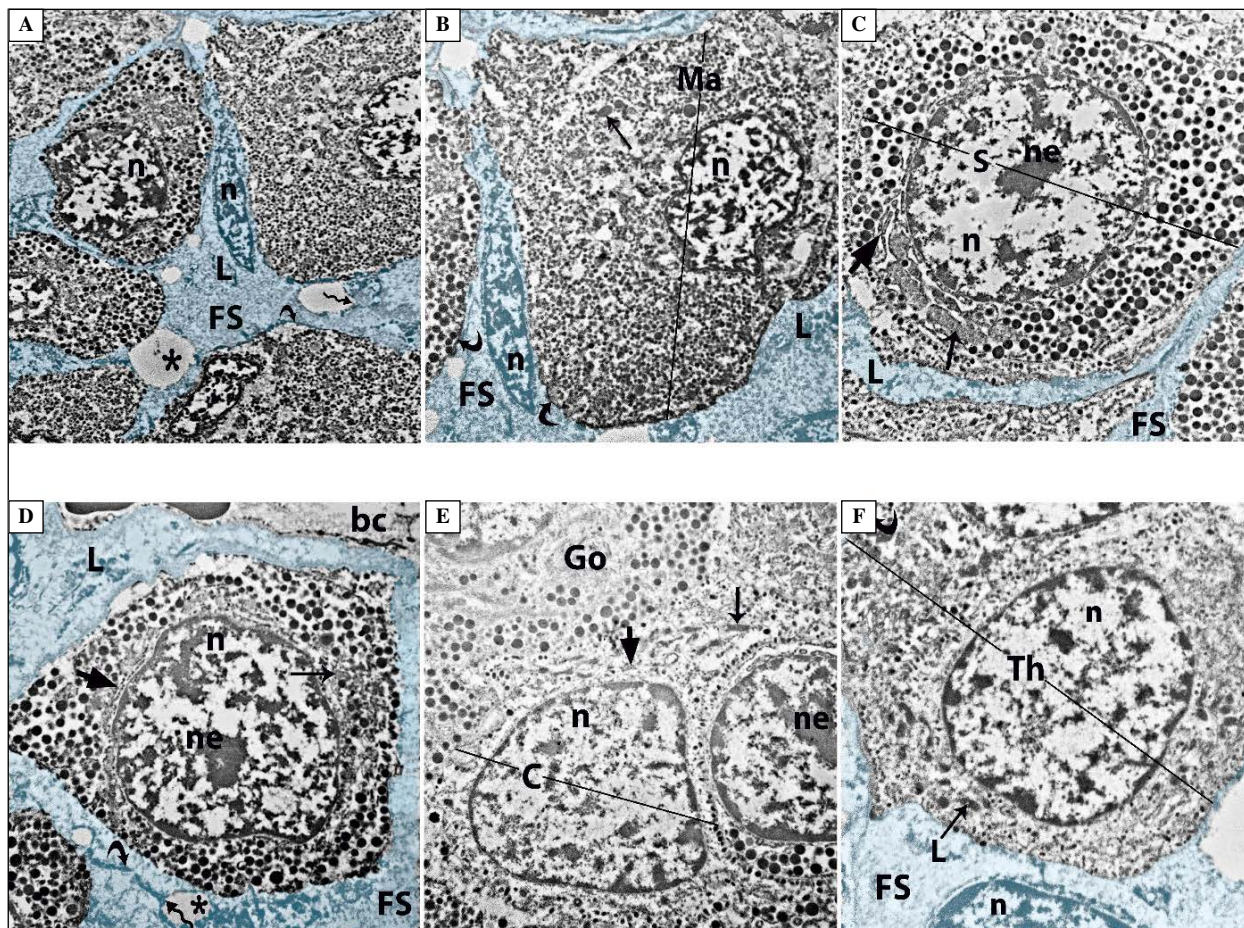
**Figure 4.** TEM photomicrographs of pars distalis in the rat pituitary glands of the control group. In (**A**) normal ultra-structure of endocrine cells and blue-labeled FSCs (FS) are noted. In (**B**) mammotrophs (Ma), illustrate abundant variable sized granules. In (**C** and **D**) somatotrophs (S) display abundant large dense granules. In (**E**) gonadotrophs (Go) show rounded granules of variable size and density mainly at the pole of the cell, while corticotrophs (C) with the fewest granules that are small and peripherally located immediately under the plasmalemma. In (**F**) thyrotrophs (Th) show many peripheral small granules. All secretory cells reveal euchromatic nuclei (n), prominent nucleoli (ne), rER (short arrow) and mitochondria (arrow). FSCs (FS) are visualized with euchromatic nuclei (n), and lysosomes (L). They line follicles filled with colloid (*) and surrounded by junctional complexes (wavy arrow). Their processes are stretched between the secretory cells and extend to the blood capillaries (bc). Gap junctions (curved arrow) are noted between FSCs and between them and the secretory cells. Magnifications: A: 5000×; B: 6000×; C, D and E: 8000×; F: 1000×; (B) is a higher magnification of (A).

of cellular damage. The cells appeared fused with rarified vacuolated cytoplasm, swollen degenerated mitochondria with ruptured cristae, dilated disrupted rER and reduced number of secretory granules. In addition, the nuclei revealed signs of apoptosis such as nuclear irregularity, shrunken dense nuclei, multiple large chromatin clumps and chromatin margination.

On the contrary, the FSCs (Figs. 5A–G) demonstrated apparently normal ultrastructure with multiple electron-dense particles within the colloid. Additionally, FSCs contained multiple cytoplasmic electron-dense bodies (lysosomes), multiple mitochondria and vesicles filled with colloid material.

## Discussion

The current work aimed at investigating the histological and biochemical influences of repeated oral intake of small-sized (11 ± 2 nm) Au-NPs on the pars distalis of the pituitary gland of adult male albino rats, with special reference to their effects on FSCs.

In this study, small-sized Au-NPs were chosen because it was demonstrated that nanoparticles' diagnostic and therapeutic features such as plasma half-life [25], uptake by the cells [26] and tumor infiltration [27], are affected by their sizes. It has been assumed that for effective biological effects of NPs their size
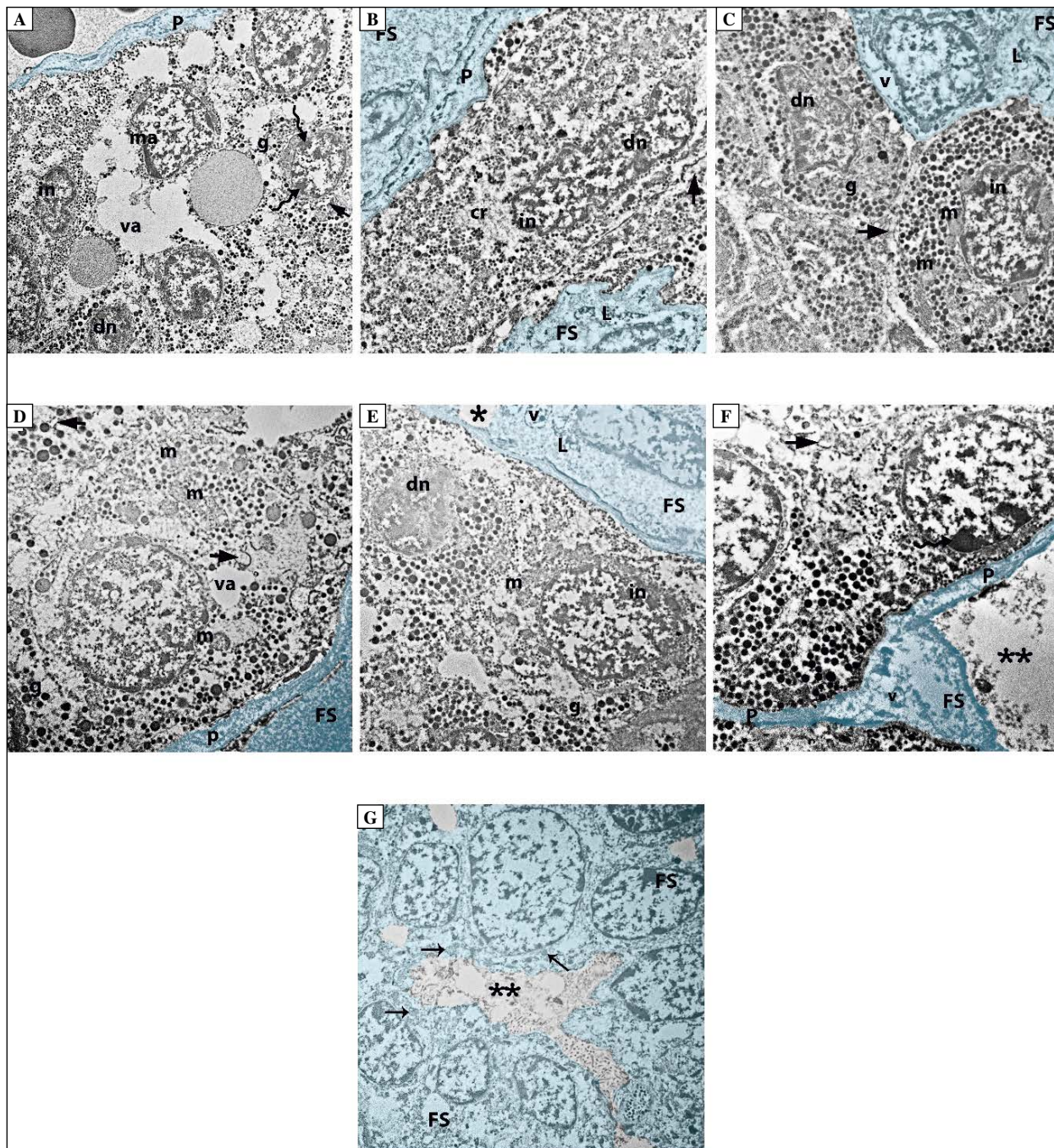
**Figure 5.** TEM photomicrographs of pars distalis in the rat pituitary glands of the Au-NP group. EM photographs A–D show marked degeneration of different endocrine cells illustrating fused cells with cytoplasmic vacuolations (va) and rarefication (Cr) dilated disrupted rER (short arrow), swollen mitochondria with ruptured cristae (m) and few secretory granules (g). The nuclei are either irregular (in), shrunken dense (dn), with multiple chromatin clumps (wavy arrow) or chromatin margination (ma). The FSCs (FS) appear almost normal and contain multiple lysosomes (L) and colloid-filled vesicles (v). (A–F) The FSCs' processes (P) embrace the hormonal cells and/or the colloid materials (*). The large-sized colloid (**) display multiple electron-dense particles. (G) A group of FSCs (FS) surrounding large-sized colloid (**) and they display multiple mitochondria (arrow) in their cytoplasm. Magnifications: A: 4000×; B, C and E: 6000×; D and F: 8000×; G: 5000×.

has to range between 10–200 nm since NPs smaller than 10 nm can be filtered by the kidneys and NPs larger than 200 nm could activate the immune system resulting in their elimination from blood [28]. So, the optimum size was recognized to be 50 nm [26] but the size of 10–20 nm adds more therapeutic benefits like the tumor penetration ability [27]. Additionally, male rats were used to avoid the changes that occur in the density of the somatotrophs and the mammotrophs in females due to the trans-differentiation between them [29].

In the current work, the rats which received orally Au-NPs for 2 weeks were found to accumulate Au-NPs in the pituitary gland detected by ICP-MS. This is concomitant with formerly reported results where Au-NPs were accumulated in different mice organs following single and repeated intravenous administrations, repeated intraperitoneal injections and oral intake [12]. In rodents, such deposition could be explained by the distribution of Au-NPs throughout the body by blood, with the liver and the spleen (mononuclear phagocytic system) being the first organs to show Au-NPs accumulation, followed by the lungs [30]. Once the nanoparticles reached the systemic circulation, they were distributed *via* blood to all other organs including kidneys [31]. Additionally, 20 nm-sized Au-NPs can cross the blood-retina barrier resulting in their deposition in the retina [32].

In various organs, Au-NPs were taken up by the cells mainly through clathrin-mediated endocytosis [33]. This occurs *via* two stages; the first one is a rapid phase that lasts for 6 h where the Au-NPs are free and easily taken-up by the cells and the second one is a plateau stage where the particles are conjugated with serum proteins forming more stable Au-NPs//protein complexes [34]. Such cellular uptake occurred deoebdent on Au-NPs size where the smaller ones (10 nm) were more widely deposited in the organs than larger ones (50 nm) [35].

The main finding of our study was the demonstration that the deposition of Au-NPs in the pars distalis of young adult male rats resulted in its disorganization and cellular damage. Our study adds important data to the research on the distribution of gold nanoparticles in other organs of rat [31] and mouse [30]. In the present study we present novel findings indicating deterioration of the histomorphology of the adenohypohysis as a result of the repeated Au-NPs treatment of male Wistar rats. We also showed that the ultrastructural changes induced by Au-NPs administration resulted in functional damage since the serum concentration of FSH, LH and PRL was reduced in the rats treated with gold nanoparticles. One explanation of such a damaging effect of Au-NPS may be related to the

oxidative stress as a result of the production of high levels of reactive oxygen species (ROS) [36].

In the present study, tendency to increased catalase level, a key antioxidant enzyme, was noted in Au-NPs rats *versus* the control rats. Although daily oral administration of (5 and 10 mg/kg) Au-NPs in rats for 3 weeks increased the production of antioxidants, this increase was not statistically significant [31]. In this previous study [31], the antioxidant level was not enough to compensate for the increased ROS leading to imbalance of the redox system [37]. Besides, it was proved that intraperitoneal injection of 20 nm sized nanoparticles to rats for 3 days reduced the activity of the antioxidant, reduced glutathione peroxidase [38]. This explanation is similar to that proposed by Elbakary *et al.* to explain lung tissue damage induced by Au-NPs [20].

The high ROS levels lead to DNA damage, protein oxidation and lipid peroxidation [37]. The release of lipid peroxidation products such as MDA and 4-hydroxy-2-nonenal (4-HNE) induces inflammation and apoptotic cell death [39]. This was enforced in the current work by the significant increase in the mean level of MDA in Au-NPs rats as compared to the control rats. Further support came from the presence of inflammatory signs (congestion and dilatation of the blood vessels, extra-vascular exudate and inflammatory cell infiltration) and evidently increased apoptosis expressed in highly increased relative area of Cyt-c immunoreactivity.

These inflammatory signs were previously reported in the lung tissue following Au-NPs administration. Besides, prominent population of Kupffer cells was demonstrated in the liver for more phagocytic activity and nanoparticles elimination [31]. Au-PNs have been shown to induce the release of the pro-inflammatory cytokines, as a sequel of nanoparticles-induced ROS production and oxidative stress where interleukin (IL)-1$\alpha$ and TNF-$\alpha$ were detected in mice brain following 'nanoparticles' administration [38]. Additionally, other cytokines induced neutrophil chemoattractant and macrophage inflammatory protein-1$\alpha$ were reported to recruit neutrophils and macrophages to engulf the Au-NPs deposited in the lungs [40]. Such inflammatory reaction explanation was supported in the current study by the significant increase in the serum level of TNF-$\alpha$ in Au-NPs rats as compared to the control rats.

Prolonged inflammation leads to the release of more ROS, more cellular damage and apoptotic cell death [20]. In the adenohypophyseal sections of AU-NPs-treated rats, the detected cellular death was presumed to be due to mitochondrial (intrinsic) pathway of apoptosis, as it resulted from cellular

stresses (oxidative and inflammatory) [31]. These stresses ensue consequently production of ROS and lipid peroxidation leading to mitochondrial dysfunction [39]. Additionally, it was reported *in vitro* that Au-NPs overexpress Bax (pro-apoptotic protein) that forms heterodimer with Bcl-2 (anti-apoptotic protein) [41]. This successively results into release of mitochondrial Cyt-c (pro-apoptotic protein) [41] and inevitable apoptotic cell death through increased expression of caspase-3 [31].

Such assumption was enforced by the data presented in this study through the appearance of the mitochondrial degeneration signs in ultrathin sections and the significant increase in the mean area % of Cyt-c immunoreactivity in Au-NPs group *versus* the control group. Further reinforcement came from the significant decrease in the level of Bcl-2 in the pars distalis homogenates of group II compared to group I. In the same way, other study [42] stated that accumulated Au-NPs provoke a significant increase in the mRNA expression of Bax, P53, caspase-3 and caspase-9. This, in turn, suggests the intrinsic pathway of apoptosis.

Cellular damage displayed in the pars distalis of group II was furtherly reinforced by the significant decrease in the serum levels of PRL secreted by acidophils, and FSH and LH secreted by basophils. Moreover, there was diminished intracellular PAS positive reaction that indicated reduced basophils content. In the same way, other study denoted decreased GH immunoexpression following cellular apoptosis induced by oral malathion [17].

Interestingly, Au-NPs can cross the blood brain barrier and accumulate in the brain [43]. There, they can induce apoptosis of neurons of the cerebral cortex and the hippocampus [4]. By the same token, they could induce apoptosis in the hypothalamus and their secretory cells. This was supported previously [44, 45] by reporting the negative effect of nanoparticles on the ovarian and testicular functions *via* acting on the hypothalamic-pituitary-gonadal axis.

On the contrary to the secretory cells of the pars distalis, FSCs were shown in Au-NPs-treated rats to be intact and probably proliferated. This was supported by the increase in the mean area percent of the S-100 immunoreactivity in this group *versus* the control group. This could be explained by the fact that FSCs are considered as the stem cells to the pars distalis endocrine cells [46]. Additionally, they are believed to be their nursing cells *via* their processes that extend to the blood capillaries and are localized between endocrine cells [47]. Moreover, the gap junctions present between FSCs and between them and the endocrine cells allow rapid spread of the signals and the trophic factors secreted by FSCs to the other FSCs and the

endocrine cells which they support, controlling their secretion and promoting their proliferation [48]. Thus, the significant increase in the mean area percent of Cx43 immunoreactivity in Au-NPs rats as compared with the control rats ensured the nursing potential of FSCs.

One of these trophic growth factors is bFGF that is a potent angiogenic factor in the anterior pituitary and it has a paracrine action promoting cell proliferation and differentiation and autocrine action that increases its own secretion. Besides, it increases the gap junctions between FSCs and between FSCs and endocrine cells [48]. In the adenohypophysis it is secreted mainly by FSCs [49]. The significant increase of its serum level in group II was suggested to be due to its augmented secretion by FSCs.

Moreover, FSCs are supposed to be phagocytic cells that engulf the apoptotic pars distalis cells, degrade them within their lysosomes and secrete the residual cellular debris into the colloid in the middle of FSCs clusters [50]. Since the apoptotic cell death was documented in Au-NPs-treated rats to be more intense than in the control rats, the phagocytic capability of FSCs was assumed to be augmented. This was supported by the presence of numerous electron-dense lysosomes and electron-dense particles within the colloid. Further support came from the enlarged colloid size detected in ultrathin sections and the increased extracellular positive PAS reaction. Such increase in this PAS reaction product was identified to probably compensate for its intracellular decrease in basophils due to their apoptosis.

In summary, we demonstrated that in rat repetitive oral administration of small-sized gold nanoparticles resulted in their deposition in the pituitary gland with subsequent degeneration of endocrine cells together with biochemical and functional alterations. However, FSCs proliferated and displayed increased growth factors production, as bFGF. This proliferation could be suggested to remove cell degeneration wastes and to support the endocrine cells *via* paracrine secretions of these growth factors.

## Conflict of interest

All authors declare no conflict of interest.

### References

1. Jeevanandam J, Barhoum A, Chan YS, et al. Review on nanoparticles and nanostructured materials: history, sources, toxicity and regulations. Beilstein J Nanotechnol. 2018; 9: 1050–1074, doi: 10.3762/bjnano.9.98, indexed in Pubmed: 29719757.
2. Buzea C, Pacheco II, Robbie K. Nanomaterials and nanoparticles: sources and toxicity. Biointerphases. 2007; 2(4): MR17–MR71, doi: 10.1116/1.2815690, indexed in Pubmed: 20419892.

3. Wicki A, Witzigmann D, Balasubramanian V, et al. Nanomedicine in cancer therapy: challenges, opportunities, and clinical applications. J Control Release. 2015; 200: 138–157, doi: 10.1016/j.jconrel.2014.12.030, indexed in Pubmed: 25545217.

4. El-Drieny EA, Sarhan NI, Bayomy NA, et al. Histological and immunohistochemical study of the effect of gold nanoparticles on the brain of adult male albino rat. J Microsc Ultrastruct. 2015; 3(4): 181–190, doi: 10.1016/j.jmau.2015.05.001, indexed in Pubmed: 30023198.

5. Versiani A, Andrade L, Martins E, et al. Gold nanoparticles and their applications in biomedicine. Future Virol. 2016; 11(4): 293–309, doi: 10.2217/fvl-2015-0010.

6. Chow EKH, Ho D. Cancer nanomedicine: from drug delivery to imaging. Sci Transl Med. 2013; 5(216): 216rv4, doi: 10.1126/scitranslmed.3005872, indexed in Pubmed: 24353161.

7. Lal S, Clare SE, Halas NJ. Nanoshell-enabled photothermal cancer therapy: impending clinical impact. Acc Chem Res. 2008; 41(12): 1842–1851, doi: 10.1021/ar800150g, indexed in Pubmed: 19053240.

8. Luo P, Stutzenberger F. Nanotechnology in the detection and control of microorganisms. Adv Appl Microbiol. 2008: 145–181, doi: 10.1016/s0065-2164(07)00004-4.

9. Marques Neto LM, Kipnis A, Junqueira-Kipnis AP. Role of Metallic Nanoparticles in Vaccinology: Implications for Infectious Disease Vaccine Development. Front Immunol. 2017; 8: 239, doi: 10.3389/fimmu.2017.00239, indexed in Pubmed: 28337198.

10. Pissuwan D, Niidome T, Cortie MB. The forthcoming applications of gold nanoparticles in drug and gene delivery systems. J Control Release. 2011; 149(1): 65–71, doi: 10.1016/j.jconrel.2009.12.006, indexed in Pubmed: 20004222.

11. Skirtach AG, Muñoz Javier A, Kreft O, et al. Laser-induced release of encapsulated materials inside living cells. Angew Chem Int Ed Engl. 2006; 45(28): 4612–4617, doi: 10.1002/anie.200504599, indexed in Pubmed: 16791887.

12. Lasagna-Reeves C, Gonzalez-Romero D, Barria MA, et al. Bioaccumulation and toxicity of gold nanoparticles after repeated administration in mice. Biochem Biophys Res Commun. 2010; 393(4): 649–655, doi: 10.1016/j.bbrc.2010.02.046, indexed in Pubmed: 20153731.

13. Prades R, Guerrero S, Araya E, et al. Delivery of gold nanoparticles to the brain by conjugation with a peptide that recognizes the transferrin receptor. Biomaterials. 2012; 33(29): 7194–7205, doi: 10.1016/j.biomaterials.2012.06.063, indexed in Pubmed: 22795856.

14. Perez-Castro C, Renner U, Haedo MR, et al. Cellular and molecular specificity of pituitary gland physiology. Physiol Rev. 2012; 92(1): 1–38, doi: 10.1152/physrev.00003.2011, indexed in Pubmed: 22298650.

15. Yeung CM, Chan CB, Leung PS, et al. Cells of the anterior pituitary. Int J Biochem Cell Biol. 2006; 38(9): 1441–1449, doi: 10.1016/j.biocel.2006.02.012, indexed in Pubmed: 16621669.

16. Haschek W, Rousseaux C, Wallig M. Endocrine System. Fundamentals Toxicol Pathol. 2010: 513–551, doi: 10.1016/b978-0-12-370469-6.00017-9.

17. El-Kordy E, Mubarak HED, Makhlouf M, et al. Effect of malathion on pars distalis of the pituitary gland and the possible protective role of vitamin C in adult female albino rats. Egyptian J Histol. 2014; 37(3): 453–463, doi: 10.1097/01.ehx.0000452052.09124.28.

18. Pires M. Update on pituitary folliculo-stellate cells. Int Arch Endocrinol Clin Res. 2016; 2(1), doi: 10.23937/2572-407x.1510006.

19. Le Tissier PR, Hodson DJ, Lafont C, et al. Anterior pituitary cell networks. Front Neuroendocrinol. 2012; 33(3): 252–266, doi: 10.1016/j.yfrne.2012.08.002, indexed in Pubmed: 22981652.

20. Elbakary R, Okasha E, Ragab A, et al. Histological effects of gold nanoparticles on lung tissue of adult male albino rats. J Microsc Ultrastruct. 2018; 6(2): 116–122, doi: 10.4103/JMAU.JMAU_25_18, indexed in Pubmed: 30221136.

21. Lévy R, Thanh NTK, Doty RC, et al. Rational and combinatorial design of peptide capping ligands for gold nanoparticles. J Am Chem Soc. 2004; 126(32): 10076–10084, doi: 10.1021/ja0487269, indexed in Pubmed: 15303884.

22. Barathmanikanth S, Kalishwaralal K, Sriram M, et al. Anti-oxidant effect of gold nanoparticles restrains hyperglycemic conditions in diabetic mice. J Nanobiotechnology. 2010; 8: 16, doi: 10.1186/1477-3155-8-16, indexed in Pubmed: 20630072.

23. Kiernan J. Histological and histochemical methods: Theory and practice. New York: Arnold publisher; 2001.

24. Salama NM, Zaghlol SS, Mohamed HH, et al. Suppression of the inflammation and fibrosis in Asherman syndrome rat model by mesenchymal stem cells: histological and immunohistochemical studies. Folia Histochem Cytobiol. 2020; 58(3): 208–218, doi: 10.5603/FHC.a2020.0024, indexed in Pubmed: 32996119.

25. Faraji AH, Wipf P. Nanoparticles in cellular drug delivery. Bioorg Med Chem. 2009; 17(8): 2950–2962, doi: 10.1016/j.bmc.2009.02.043, indexed in Pubmed: 19299149.

26. Huang J, Bu L, Xie J, et al. Effects of nanoparticle size on cellular uptake and liver MRI with polyvinylpyrrolidone-coated iron oxide nanoparticles. ACS Nano. 2010; 4(12): 7151–7160, doi: 10.1021/nn101643u, indexed in Pubmed: 21043459.

27. Chauhan VP, Stylianopoulos T, Martin JD, et al. Normalization of tumour blood vessels improves the delivery of nanomedicines in a size-dependent manner. Nat Nanotechnol. 2012; 7(6): 383–388, doi: 10.1038/nnano.2012.45, indexed in Pubmed: 22484912.

28. de Barros AB, Tsourkas A, Saboury B, et al. Emerging role of radiolabeled nanoparticles as an effective diagnostic technique. EJNMMI Res. 2012; 2(1): 39, doi: 10.1186/2191-219X-2-39, indexed in Pubmed: 22809406.

29. Porter TE, Wiles CD, Frawley LS. Evidence for bidirectional interconversion of mammotropes and somatotropes: rapid reversion of acidophilic cell types to pregestational proportions after weaning. Endocrinology. 1991; 129(3): 1215–1220, doi: 10.1210/endo-129-3-1215, indexed in Pubmed: 1874167.

30. Yang L, Kuang H, Zhang W, et al. Comparisons of the biodistribution and toxicological examinations after repeated intravenous administration of silver and gold nanoparticles in mice. Sci Rep. 2017; 7(1): 3303, doi: 10.1038/s41598-017-03015-1, indexed in Pubmed: 28607366.

31. Aravinthan A, Kamala-Kannan S, Govarthanan M, et al. Accumulation of biosynthesized gold nanoparticles and its impact on various organs of Sprague Dawley rats: a systematic study. Toxicol Res (Camb). 2016; 5(6): 1530–1538, doi: 10.1039/c6tx00202a, indexed in Pubmed: 30090454.

32. Kim JH, Kim JH, Kim KW, et al. Intravenously administered gold nanoparticles pass through the blood-retinal barrier depending on the particle size, and induce no retinal toxicity. Nanotechnology. 2009; 20(50): 505101, doi: 10.1088/0957-4484/20/50/505101, indexed in Pubmed: 19923650.

33. Kreyling WG, Semmler-Behnke M, Möller W. Ultrafine particle-lung interactions: does size matter? J Aerosol Med. 2006; 19(1): 74–83, doi: 10.1089/jam.2006.19.74, indexed in Pubmed: 16551218.

34. Chithrani BD, Ghazani AA, Chan WCW. Determining the size and shape dependence of gold nanoparticle uptake into mammalian cells. Nano Lett. 2006; 6(4): 662–668, doi: 10.1021/nl052396o, indexed in Pubmed: 16608261.

35. De Jong WH, Hagens WI, Krystek P, et al. Particle size-dependent organ distribution of gold nanoparticles after intravenous administration. Biomaterials. 2008; 29(12): 1912–1919, doi: 10.1016/j.biomaterials.2007.12.037, indexed in Pubmed: 18242692.

36. Dykman L, Khlebtsov N. Immunological properties of gold nanoparticles. Chem Sci. 2017; 8(3): 1719–1735, doi: 10.1039/c6sc03631g, indexed in Pubmed: 28451297.

37. Liou GY, Storz P. Detecting reactive oxygen species by immunohistochemistry. Methods Mol Biol. 2015; 1292: 97–104, doi: 10.1007/978-1-4939-2522-3_7, indexed in Pubmed: 25804750.

38. Siddiqi NJ, Abdelhalim MA, El-Ansary AK, et al. Identification of potential biomarkers of gold nanoparticle toxicity in rat brains. J Neuroinflammation. 2012; 9: 123, doi: 10.1186/1742-2094-9-123, indexed in Pubmed: 22691312.

39. Breitzig M, Bhimineni C, Lockey R, et al. 4-Hydroxy-2-nonenal: a critical target in oxidative stress? Am J Physiol Cell Physiol. 2016; 311(4): C537–C543, doi: 10.1152/ajpcell.00101.2016, indexed in Pubmed: 27385721.

40. Morimoto Y, Izumi H, Kuroda E. Significance of persistent inflammation in respiratory disorders induced by nanoparticles. J Immunol Res. 2014; 2014: 962871, doi: 10.1155/2014/962871, indexed in Pubmed: 25097864.

41. Liu M, Gu X, Zhang Ke, et al. Gold nanoparticles trigger apoptosis and necrosis in lung cancer cells with low intracellular glutathione. J Nanopart Res. 2013; 15(8), doi: 10.1007/s11051-013-1745-8.

42. Noël C, Simard JC, Girard D. Gold nanoparticles induce apoptosis, endoplasmic reticulum stress events and cleavage of cytoskeletal proteins in human neutrophils. Toxicol In Vitro. 2016; 31: 12–22, doi: 10.1016/j.tiv.2015.11.003, indexed in Pubmed: 26551149.

43. Etame AB, Diaz RJ, O'Reilly MA, et al. Enhanced delivery of gold nanoparticles with therapeutic potential into the brain using MRI-guided focused ultrasound. Nanomedicine. 2012; 8(7): 1133–1142, doi: 10.1016/j.nano.2012.02.003, indexed in Pubmed: 22349099.

44. Hou CC, Zhu JQ. Nanoparticles and female reproductive system: how do nanoparticles affect oogenesis and embryonic development. Oncotarget. 2017; 8(65): 109799–109817, doi: 10.18632/oncotarget.19087, indexed in Pubmed: 29312650.

45. Cavallin MD, Wilk R, Oliveira IM, et al. The hypothalamic-pituitary-testicular axis and the testicular function are modulated after silver nanoparticle exposure. Toxicol Res (Camb). 2018; 7(1): 102–116, doi: 10.1039/c7tx00236j, indexed in Pubmed: 30090567.

46. Kikuchi M, Yatabe M, Tando Y, et al. Immunohistochemical localization of anterior pituitary hormones in S-100 protein-positive cells in the rat pituitary gland. Cell Tissue Res. 2011; 345(3): 425–429, doi: 10.1007/s00441-011-1214-6, indexed in Pubmed: 21830043.

47. Marin F, Stefaneanu L, Kovacs K. Folliculostellate cells of the pituitary. Endocr Pathol. 1991; 2(4): 180–192, doi: 10.1007/BF02915206, indexed in Pubmed: 32138407.

48. Vitale ML, Barry A. Biphasic effect of basic fibroblast growth factor on anterior pituitary folliculostellate TtT/GF cell coupling, and connexin 43 expression and phosphorylation. J Neuroendocrinol. 2015; 27(10): 787–801, doi: 10.1111/jne.12308, indexed in Pubmed: 26265106.

49. Amano O, Yoshitake Y, Nishikawa K, et al. Immunocytochemical localization of basic fibroblast growth factor in the rat pituitary gland. Arch Histol Cytol. 1993; 56(3): 269–276, doi: 10.1679/aohc.56.269, indexed in Pubmed: 8240855.

50. Claudius L, Yoshimi Y, Yoichiro H, et al. Phagocytotic removal of apoptotic endocrine cells by folliculostellate cells and its functional implications in clusterin accumulation in pituitary colloids in helmeted guinea fowl (Numida meleagris). Acta Histochem. 2006; 108(1): 69–80, doi: 10.1016/j.acthis.2006.01.006, indexed in Pubmed: 16569423.

ORIGINAL PAPER

# Decreased immunoreactivity of von Willebrand factor may reflect persistent nature of the endothelial dysfunction in non-ischemic heart failure

Edyta Reichman-Warmusz[1], Marlena Brzozowa-Zasada[1], Celina Wojciechowska[2], Damian Dudek[1, 3], Oliwia Warmusz[1], Romuald Wojnicz[1]

[1]Department of Histology and Cell Pathology, Medical University of Silesia in Katowice, School of Medicine with the Division of Dentistry, Zabrze, Poland
[2]Second Department of Cardiology, Medical University of Silesia, School of Medicine with the Division of Dentistry, Zabrze, Poland
[3]Ambulatory Oral Surgery and Implantology, Torun, Poland

**Abstract**

**Introduction.** Endothelial dysfunction is a critical part of heart failure (HF) pathophysiology. It is not clear, however, whether it is present at the similar level in the early and late HF stages.

**Material and methods.** von Willebrand factor (vWF) and its mRNA levels in biopsies of non-ischemic patients with HF secondary to dilated cardiomyopathy were studied. Consecutive patients with HF were divided into two groups: group A with disease duration ≤ 12 months (n = 59) and group B with disease duration > 12 months (n = 68). The immunoreactivity of the vWF was compared with autopsy sections of 19 control cases. Tissue vWF gene expression was analyzed at the mRNA level by RT-PCR.

**Results.** In the group A, there was lower vWF immunoreactivity in the coronary microvessels compared to the group B [1.5 (1.0–2.0) *vs.* 2.0 (1.5–2.4), P = 0.001]. In the control group, only weak vWF expression was observed. Protein expression was not accompanied by vWF mRNA whose levels were significantly higher in the Group A as compared to the Group B [14671 (4932-51561) *vs.* 3643 (185.3–9030.8), P = 0.005]. Protein vWF expression was inversely associated with its mRNA levels (r = –0.34, P = 0.04).

**Conclusions.** High myocardial protein expression of vWF in patients with long-lasting HF symptoms may highlight the persistent nature of endothelial dysfunction in such a cohort of patients. *(Folia Histochemica et Cytobiologica 2021, Vol. 59, No. 2, 108–113)*

**Key words:** heart failure; dilated cardiomyopathy; endomyocardial biopsy; endothelial dysfunction; von Willebrand factor; qPCR; IHC

## Introduction

Heart failure is defined as a complex clinical syndrome of impaired heart functions and is a leading cause of morbidity and mortality in developed countries. The prevalence of heart failure (HF) worldwide continues to increase, maintaining high rates of morbidity and mortality despite the use of multiple evidence-based therapeutic strategies [1]. The main characteristic of HF is its multifaceted clinical presentation and its progressive nature [2].

For a long time disturbances in the coronary microcirculation have been postulated to contribute to HF development and progression [3, 4]. It is believed to be a consequence of endothelial dysfunction through loss of its multifaceted regulatory properties [5, 6]. As

**Correspondence address:** Edyta Reichman-Warmusz, PhD
Department of Histology and Cell Pathology in Zabrze,
Medical University of Silesia in Katowice,
School of Medicine with the Division of Dentistry,
Jordana 19, 41–808 Zabrze, Poland
e-mail: ewarmusz@sum.edu.pl

a result, an abnormal coronary microcirculatory flow may cause impairment of myocardial perfusion and metabolic changes compatible with local myocardial ischemia [7, 8]. More recently it has been reported that endothelial dysfunction in HF independently predicts morbidity and mortality in this cohort of patients [9, 10]. The exact mechanisms for endothelial dysfunction in HF are unclear. However, it is believed to be the result of lost nitric oxide-dependent vasodilatation, a proinflammatory state, and its prothrombotic properties [11, 12].

Von Willebrand factor (vWF) is a large multimeric glycoprotein produced by endothelial and megakaryocytes that is present in endothelial cells (Weibel-Palade bodies), the subendothelial matrix, platelets and blood plasma [13]. Its main function is mediation of platelet aggregation at the site of vascular injury and thrombus growth. Thus, given the ubiquitous involvement of vWF in local vascular homeostasis, it is not surprising that this factor plays an important role in HF pathogenesis [14]. As vWF release is increased when endothelial cells are injured, it has been proposed as a marker of endothelial dysfunction [15–17]. It is not clear, however, whether endothelial dysfunction is present to the same extent in the HF of short or long duration.

Accordingly, the aim of this study was to clarify this issue by examining biopsy specimens of patients with short and long-standing HF duration by immunohistochemistry (IHC) and RT-qPCR.

## Materials and methods

**Patients and material collection.** *Patients.* One hundred and twenty-seven patients with stable, non-ischemic HF (NYHA I to III, LVEF < 40%), attributable to dilated cardiomyopathy were prospectively studied. Right ventricular endomyocardial biopsy was carried out in all patients. Patients were divided into two groups: Group A with HF duration ≤ 12 months (n = 59; 50 men and 9 women), and Group B with HF duration > 12 months (n = 68; 63 men and 5 women). In addition, we used the cardiac autopsy sections of 19 young cases that suddenly died in car crashes (11 men, 8 women, mean age of 33.5 ± 6.8 years). This group served as a control for immunohistochemical staining of vWF protein.

All the HF patients had selective coronary angiography to exclude ischemic etiology of HF. In addition, none of the studied patients had other potential causes of HF, including valvular (except relative mitral and/or tricuspid regurgitation), endocrine disease (except impaired glucose tolerance), advanced renal disease, and reported drug or alcohol abuse. All of them were on typical therapeutic regimens for HF including loop diuretics (torasemide and/or furosemide), ACE inhibitors or ATII blockers, β-blockers, and spironol-

actone for at least 6 months prior to the biopsy. Apart from standard HF therapy, none of the patients was treated with oral anticoagulants, statins and antiarrhythmic drugs or had an electrical device implanted before the biopsy was done.

Four to five endomyocardial biopsies were obtained from each patient. All biopsies except one specimen dedicated for molecular biology, were fixed for 20 min in cold acetone, immersed in embedding medium (OCT Compound, Miles Inc., Sakura Finetek, USA) and cryo-preserved in liquid nitrogen until tested.

This study was carried out in accordance with the Helsinki Declaration, and the study design was approved by the Institutional Ethics Committee (NN-6501-7/07). All patients gave their informed consent.

**Immunohistochemistry.** For IHC, specimens were cut serially into 5 mm thick slices on a Cryotome FSE® Thermo Shandon (Thermo Scientific-Shandon, Lipshaw, PA, USA), air-dried at room temperature and incubated with murine monoclonal anti-vWF antibodies (clone F8/86); dilution 1:300; DAKO). In addition, to exclude myocarditis, frozen sections were incubated with murine monoclonal antihuman antibodies (Abs): ant-HLA-class II (DR antigens), Alpha chain (clone TAL.1B5), anti-HLA-class I (ABC antigens) (clone W6/32), anti-CD3 for T lymphocytes (Clone T3-4B5), and anti-CD68 (clone EBM11). All antibodies were from DAKO A/S, Glostrup, Denmark. The dilution of the primary antibody was verified in our laboratory in a series of pilot experiments.

The En-Vision method (DAKO En-Vision Kit®/Alkaline Phosphatase detection system) was used according to the manufacturer's instructions. The bound primary antibody was detected using New Fuchsin Substrate System (DAKO A/S). The primary antibody was omitted from negative control slides. To suppress nonspecific staining due to endogenous alkaline phosphatase activity, Levamisole was used at a final concentration of 0.2 mM. The sections were counterstained with Mayer's hematoxylin.

For the semiquantitative assessment of the intensity of vWF microvascular staining, the score index at 200× magnification was as follows: (1+) weak staining in a few vessels; (2+) moderate staining in most microvessels and (3+) strong staining in all microvessels. All IHC analyses were performed by two investigators independently, blinded to clinical features. The inter-observer variability of immunohistological examinations for vWF was < 3%. Histological results were obtained with the use of Nikon Eclipse 80*i* microscope with DS-F*i*1 digital camera and *NIS* Elements software from Nikon (Tokyo, Japan).

**Quantitative real-time PCR (qPCR).** For the real-time PCR examination of the vWF RNA, total RNA was extracted from myocardial specimens by the Trizol® reagent (Invitrogen, Thermo Fisher Scientific, Waltham, MA, USA)

**Table 1.** Baseline characteristics of the patients

| | All patients n = 127 | Group A n = 59 | Group B n = 68 | P |
|---|---|---|---|---|
| Age [y] | 44.2 ± 11.7 | 40.7 ± 10.7 | 42.4 ± 0.9 | NS |
| Sex, male/female | 113/14 | 50/9 | 63/5 | NS |
| Time of HF duration [mth] | 29.5 ± 38.9 | 7.6 ± 2.7 | 52.1 ± 21.9 | – |
| Atrial fibrillation, n [%] | 21 (16.5) | 9 (15.3) | 12 (17.6) | NS |
| BMI [kg/m$^2$] | 26.3 ± 4.6 | 25.5 ± 4.4 | 26.2 ± 5.2 | NS |
| NYHA class, n, I/II/III | 4/110/13 | 3/51/5 | 1/59/8 | NS |
| LVEF [%] | 28.1 ± 7.0 | 29.2 ± 6.4 | 27.6 ± 7.5 | NS |
| LVEDD [mm] | 68.6 ± 10.3 | 67.5 ± 11.3 | 69.6 ± 0.1 | NS |
| Serum vWF [%] | 156.3 ± 63.5 | 162.8 ± 67.3 | 149.4 ± 60.3 | NS |
| Fibrinogen [mg/dL] | 367.2 ± 95.3 | 376.0 ± 107.1 | 357.9 ± 81.5 | NS |
| CRP [mg/dL] | (–) | 1.42 (0.14–30.2) | 1.64 (0.17–21.5) | NS |
| UA [μmol/L] | 436.9 ± 111.9 | 440.5 ± 114.4 | 439.0 ± 114.6 | NS |
| NT-proBNP [pg/mL], median [1st-3rd quartile] | 898.9 (356.5–2338) | 886.8 (365–3004) | 838.3 (248.1–2757) | NS |

Values are expressed as mean ± SD or as indicated, NS — non-significant. Group A — HF duration ≤ 12 mo, group B — HF duration > 12 mo. Abbreviations: BMI — body mass index; CRP — C-reactive protein; HF — heart failure; LVEF — left ventricle ejection fraction; LVEDD — left ventricle end diastolic dimension; NYHA — New York Heart Association; NT-proBNP — amino-terminal pro-B-type natriuretic peptide; UA — uric acid

according to the manufacturer's protocol. The quality of the RNA was assessed by gel electrophoresis and the quantitative analysis of RNA extracts was performed spectrophotometrically using a GeneQuant™ pro RNA/ /DNA Calculator (Amersham Biosciences, Little Chalfont, United Kingdom). The quantitative analysis was carried out with the use of an Opticon™ DNA Engine Continuous Fluorescence detector (MJ Research, Reno, NV, United States). The expression of the mRNA for vWF was determined by quantitative real-time PCR (forward sequence: CCTTGAATCCCAGTGACCCTGA, reverse sequence: GGTTCCGAGATGTCCTCCACAT). The PCRs of RNA extracted from biopsy specimens were carried out in 25 cycles. All PCR reactions were terminated by a final elongation step of 10 min at 72°C. All samples were tested in triplicate. The PCR amplicons was determined after each round of amplification, using the fluorescent dye SYBR-Green (Sybr Green Quantitect RT-PCR Kit; Qiagen, Venlo, Netherlands). Glyceraldehyde-3-phosphate dehydrogenase (GAPDH) and $\beta$-actin (TaqMan® DNA template reagents kit; PE Applied Biosystems) were included to monitor RT-PCR. To assess vWF gene expression in the studied groups we used the standard curve method to determine the absolute mRNA quantity in the samples. PCR products were separated on 6% polyacrylamide gel and visualized using silver staining. The length of the amplified fragments was assessed by analysis with Quantity One 4.6.9 software (Molecular Imager ChemiDOC XRS+, BIO-RAD, Hercules, CA, USA).

**Statistical analysis.** The statistical analysis was made with the SPSS version 16.0 software package (SPSS, Inc., Chicago, IL, USA). Data were analyzed by the Shapiro-Wilk test to determine distribution. Normally distributed data were analyzed using $t$-test (based on normal distribution tested by the Kolmogorov-Smirnov test) and expressed as mean ± SD. Not normally distributed data are presented as median with interquartile range (IQR; 25th and 75th percentiles). To compare not normally distributed data of vWF immunoreactivity in all studied groups, Kruskal-Wallis analysis of ranks and *post hoc* test of the Mann-Whitney U test were used. Associations between them were done by the Kendall's *tau* test. Differences were considered statistically significant at $P < 0.05$.

## Results

Clinical and demographic details of the study patients are shown in Table 1. Except for the HF duration, there was no difference in age, gender, etiology of HF, and medications used between the study groups. For the overall group of patients, the average time of symptoms was 19 months (ranging from 0.6 months to 8 years), and all the patients were in NYHA class I, II or III.

In the control cryostat sections, only weak and focally distributed expression of vWF was observed (Fig. 1A and 1B). The cryostat sections taken from HF patients presented both basal and strong immunoreactivity of vWF (Fig. 1C and 1D). In group A (HF duration ≤ 12 months), there was lower pheno-
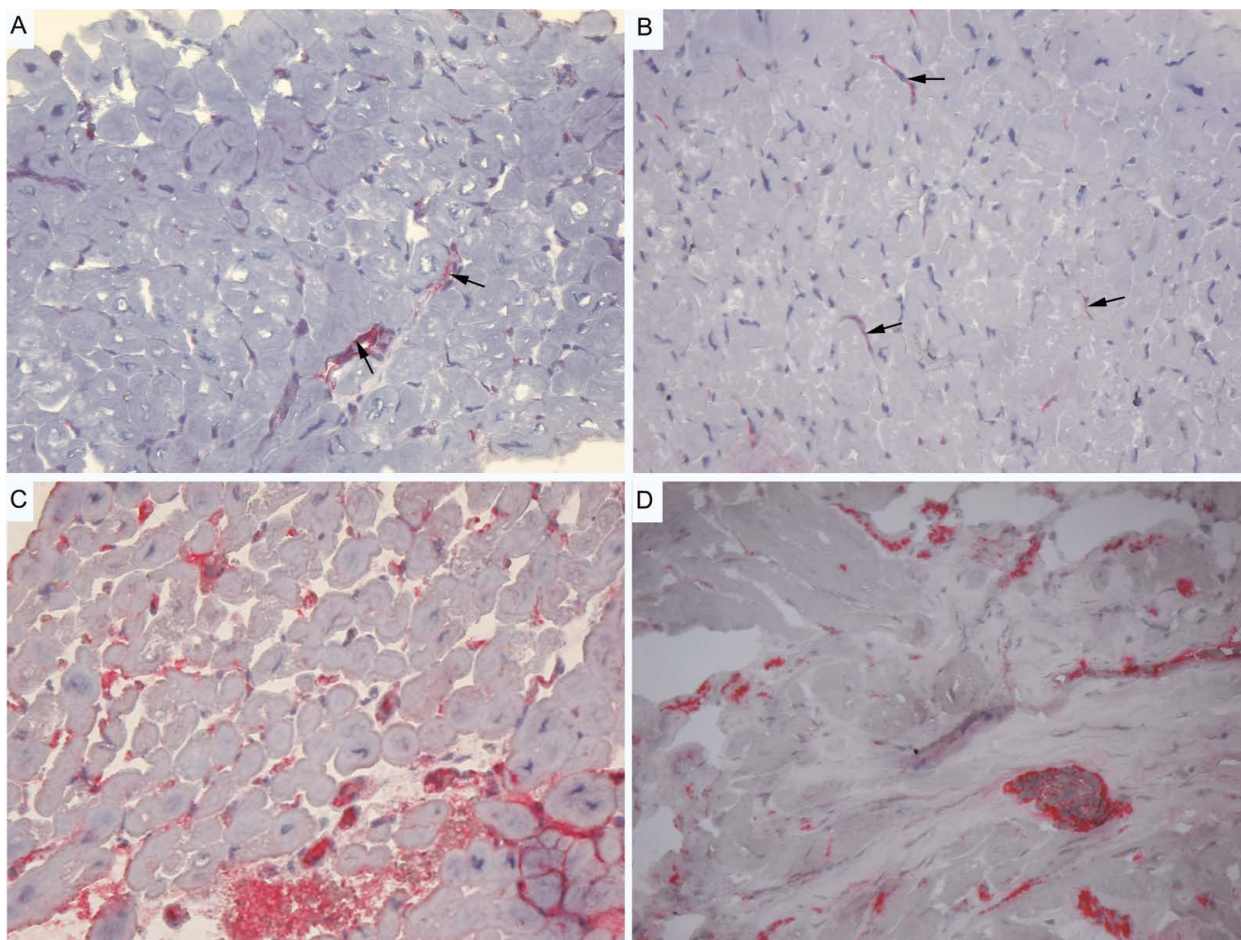
**Figure 1.** Representative examples of vWF immunostaining in the study groups: Group A — heart failure duration ≤ 12 mths, Group B — heart failure duration > 12 mths. The basal expression of vWF on sparse microvessels (arrows) in the control subjects (original magnification 100×). (**C** and **D**) The strong up-regulation of vWF on microvascular endothelium in two HF subjects from the Group B (red color; original magnification × 100).

type vWF expression in the coronary microvessels in comparison with group B (HF duration > 12 months) [1.5 (1.0–2.0) *vs.* 2.0 (1.5–2.4), P < 0.001] (Fig. 2). Unexpectedly, the IHC data was not collaborated with the vWF mRNA copy quantity which were present in a wide range in both study groups and were significantly lower in patients with long-standing disease [median 14671 (range 4932–51561) *vs.* 3643 (185.3–9030.8), P = 0.005] (Fig. 3). In addition, vWF protein immunoreactivity was inversely associated with vWF mRNA levels (r = –0.34, P = 0.04).

## Discussion

To the best of our knowledge, we have for the first time observed a relationship between up-regulation of vWF protein immunoreactivity in the myocardium of patients with non-ischemic HF secondary to dilated cardiomyopathy and the disease duration.
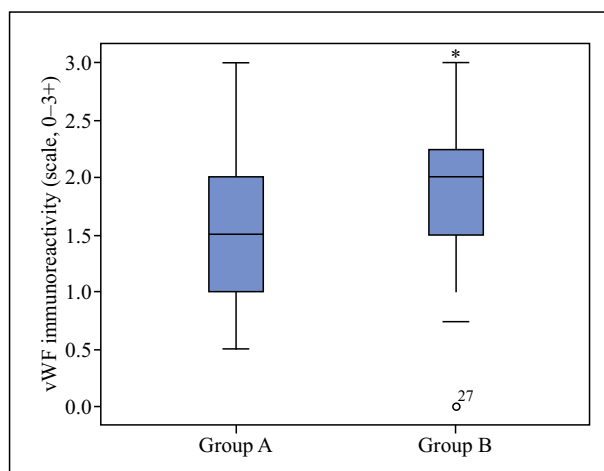


**Figure 2.** Comparison of the immunoreactivity index (0–3+) for vWF between the Group A (HF duration ≤ 12 mths) and Group B (HF duration > 12 mths). Values are medians with IQRs. *P < 0.001. The Immunoreactivity index was calculated as described in Methods.
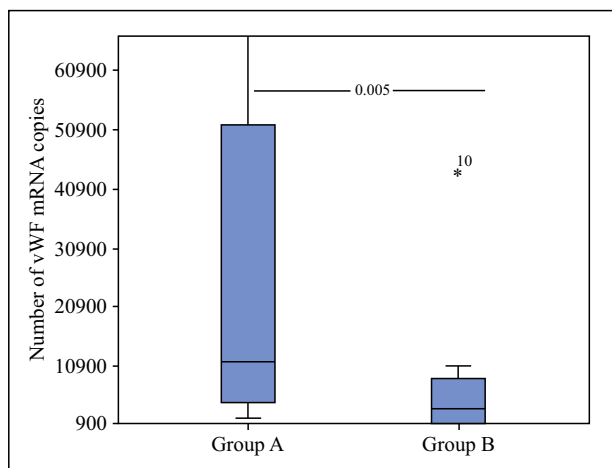
**Figure 3.** vWF gene expression in the Group A (HF duration ≤ 12 months) *versus* Group B (HF duration > 12 months) by RT-qPCR. Data presented show the mRNA quantity/μg for vWF obtained by the use of standard curve method.

It was known that vWF, stored mainly in the Weibel-Palade bodies of endothelial cells, can be mobilized rapidly after endothelial cell activation [6]. In addition, among hemostatic mediators, vWF plays a key role in platelet aggregation and stabilization of circulating clotting factors [13].

Most previously published reports focused on soluble vWF levels in plasma of HF patients [18, 19]. Following the observations by Lip *et al.*, HF were found to substantially increase plasma vWF concentrations and appeared to be highest among patients with acute or recently decompensated HF [20]. Of note, in this study the risk of stroke and thromboembolism was substantially increased in patients with congestive HF concomitant with atrial fibrillation. In another study by Gibbs *et al.*, patients with persistently increased serum concentrations of vWF and higher degree of endothelial dysfunction had a higher risk of thrombosis [21]. Studies by Kleber *et al.* have shown that plasma vWF was an independent predictor of the long-term outcome in these patients [18].

Little attention has been paid to tissue vWF expression in HF patients. Fukuchi *et al.* [22] have provided evidence that stronger tissue immunoreactivity for vWF in the endocardial endothelium in overloaded human atrial appendage may be a local predisposing factor for intra-atrial thrombogenesis. Our findings extend these results, revealing persistent vWF expression on the coronary microvessels in HF patients. Although hypothetical, this may reflect the role of endothelial dysfunction in perpetuating myocardial failure in such a cohort of patients.

The increased vWF protein immunoreactivity together with diminished levels of mRNA in long-last-

ing HF in our study seems to be only on the surface discrepant. Taking into consideration the results of previous study, it is likely that it may reflect lower turnover of this protein rather than an increase in its synthesis in the endothelium. Indeed, it was reported that activity of plasma metalloprotease ADAMTS13 which cleaves vWF was decreased in HF. Such low ADAMTS13 activities were accompanied with high vWF serum levels of HF patients [14].

It has to be kept in mind that the size of sample in our study is limited. Therefore this study may not have been powered enough to verify negative relationship of phenotype protein expression and mRNA levels found. Moreover, we did not perform follow-up biopsies to better reflect time-related changes in protein and mRNA expressions. Our findings cannot be extrapolated to patients with more severe disease or unstable conditions.

Despite these limitations in the present study we demonstrated for the first time the persistent nature of vWF protein expression in the coronary microvessels of non-ischemic HF patients. Considering the results, it may be hypothesized that some of these patients are stranded on a self-perpetuating course of advancing heart failure. Thus, persistent endothelial dysfunction as reflected by the up-regulation of myocardial vWF protein expression in patients with long-standing HF might contribute to local hypercoagulability and hence actively contributes to the disease progression.

**Conflict of interest**
The authors declare no conflict of interest.

**References**

1.  Rosamond W, Flegal K, Furie K, et al. American Heart Association Statistics Committee and Stroke Statistics Subcommittee, American Heart Association Statistics Committee and Stroke Statistics Subcommittee. Heart disease and stroke statistics-2008 update: a report from the American Heart Association Statistics Committee and Stroke Statistics Subcommittee. Circulation. 2008; 117(4): e25–146, doi: 10.1161/CIRCULATIONAHA.107.187998, indexed in Pubmed: 18086926.
2.  Mosterd A, Hoes AW, Mosterd A, et al. Clinical epidemiology of heart failure. Heart 2007;93:1137-1146. , doi: 10.1136/hrt.2003.025270, indexed in Pubmed: 17699180.
3.  Inoue T, Sakai Y, Morooka S, et al. Coronary flow reserve in patients with dilated cardiomyopathy. Am Heart J. 1993; 125(1): 93–98, doi: 10.1016/0002-8703(93)90061-d, indexed in Pubmed: 8417548.
4.  Salgado DR, Favory R, Rocco JR, et al. Microcirculatory effects of angiotensin II inhibitors in patients with severe heart failure. Clin Hemorheol Microcirc. 2013; 54(1): 87–98, doi: 10.3233/CH-2012-1569, indexed in Pubmed: 22890051.

5.  van Hinsbergh VWM. Endothelium-role in regulation of coagulation and inflammation. Semin Immunopathol. 2012; 34(1): 93–106, doi: 10.1007/s00281-011-0285-5, indexed in Pubmed: 21845431.

6.  Zuchi C, Tritto I, Carluccio E, et al. Role of endothelial dysfunction in heart failure. Heart Fail Rev. 2020; 25(1): 21–30, doi: 10.1007/s10741-019-09881-3, indexed in Pubmed: 31686283.

7.  Chen JW, Ting CT, Chen YH, et al. Differential coronary microvascular function in patients with left ventricular dysfunction of unknown cause — implication for possible mechanism of myocardial ischemia in early stage of cardiomyopathy. Int J Cardiol. 1999; 69(3): 251–261, doi: 10.1016/s0167-5273(99)00042-x, indexed in Pubmed: 10402108.

8.  Heuvel Av, Veldhuisen Dv, Wall Ev, et al. Regional myocardial blood flow reserve impairment and metabolic changes suggesting myocardial ischemia in patients with idiopathic dilated cardiomyopathy. J Am Coll Cardiol. 2000; 35(1): 19–28, doi: 10.1016/s0735-1097(99)00499-4, indexed in Pubmed: 10636254.

9.  Neglia D, Michelassi C, Trivieri MG, et al. Prognostic role of myocardial blood flow impairment in idiopathic left ventricular dysfunction. Circulation. 2002; 105(2): 186–193, doi: 10.1161/hc0202.102119, indexed in Pubmed: 11790699.

10. Fischer D, Rossa S, Landmesser U, et al. Endothelial dysfunction in patients with chronic heart failure is independently associated with increased incidence of hospitalization, cardiac transplantation, or death. Eur Heart J. 2005; 26(1): 65–69, doi: 10.1093/eurheartj/ehi001, indexed in Pubmed: 15615801.

11. Katz SD, Hryniewicz K, Hriljac I, et al. Vascular endothelial dysfunction and mortality risk in patients with chronic heart failure. Circulation. 2005; 111(3): 310–314, doi: 10.1161/01.CIR.0000153349.77489.CF, indexed in Pubmed: 15655134.

12. Lerman A, Zeiher A. Endothelial Function. Circulation. 2005; 111(3): 363–368, doi: 10.1161/01.cir.0000153339.27064.14, indexed in Pubmed: 15668353.

13. Ruggeri Z. Structure and Function of von Willebrand Factor. Thromb Haemost. 2017; 82(08): 576–584, doi: 10.1055/s-0037-1615883, indexed in Pubmed: 10605754.

14. Gombos T, Makó V, Cervenak L, et al. Levels of von Willebrand factor antigen and von Willebrand factor cleaving protease (ADAMTS13) activity predict clinical events in chronic heart failure. Thromb Haemost. 2009; 102(3): 573–580, doi: 10.1160/TH09-01-0036, indexed in Pubmed: 19718479.

15. Nowroozpoor A, Gutterman D, Safdar B. Is microvascular dysfunction a systemic disorder with common biomarkers found in the heart, brain, and kidneys? A scoping review. Microvasc Res. 2021; 134: 104123, doi: 10.1016/j.mvr.2020.104123, indexed in Pubmed: 33333140.

16. Galatius S, Wroblewski H, Sïrensen V, et al. Endothelin and von Willebrand factor as parameters of endothelial function in idiopathic dilated cardiomyopathy: Different stimuli for release before and after heart transplantation? Am Heart J. 1999; 137(3): 549–554, doi: 10.1016/s0002-8703(99)70505-3, indexed in Pubmed: 10047640.

17. El-Mansi S, Nightingale TD. Emerging mechanisms to modulate VWF release from endothelial cells. Int J Biochem Cell Biol. 2021; 131: 105900, doi: 10.1016/j.biocel.2020.105900, indexed in Pubmed: 33301925.

18. Kleber ME, Koller L, Goliasch G, et al. Von Willebrand factor improves risk prediction in addition to N-terminal pro-B-type natriuretic peptide in patients referred to coronary angiography and signs and symptoms of heart failure and preserved ejection fraction. Circ Heart Fail. 2015; 8(1): 25–32, doi: 10.1161/CIRCHEARTFAILURE.114.001478, indexed in Pubmed: 25342739.

19. Zannad F, Stough WG, Regnault V, et al. Is thrombosis a contributor to heart failure pathophysiology? Possible mechanisms, therapeutic opportunities, and clinical investigation challenges. Int J Cardiol. 2013; 167(5): 1772–1782, doi: 10.1016/j.ijcard.2012.12.018, indexed in Pubmed: 23298559.

20. Lip GYH, Pearce LA, Chin BSP, et al. Effects of congestive heart failure on plasma von Willebrand factor and soluble P-selectin concentrations in patients with non-valvar atrial fibrillation. Heart. 2005; 91(6): 759–763, doi: 10.1136/hrt.2004.036160, indexed in Pubmed: 15894770.

21. Gibbs CR, Blann AD, Watson RD, et al. Abnormalities of hemorheological, endothelial, and platelet function in patients with chronic heart failure in sinus rhythm: effects of angiotensin-converting enzyme inhibitor and beta-blocker therapy. Circulation. 2001; 103(13): 1746–1751, doi: 10.1161/01.cir.103.13.1746, indexed in Pubmed: 11282905.

22. Fukuchi M, Watanabe J, Kumagai K, et al. Increased von Willebrand factor in the endocardium as a local predisposing factor for thrombogenesis in overloaded human atrial appendage. J Am Coll Cardiol. 2001; 37(5): 1436–1442, doi: 10.1016/s0735-1097(01)01125-1, indexed in Pubmed: 11300458.

ORIGINAL PAPER

# Repeated isoflurane exposures of neonatal rats contribute to cognitive dysfunction in juvenile animals: the role of miR-497 in isoflurane-induced neurotoxicity

**Yuanyuan Que, Fangxiang Zhang, Jing Peng, Zhuhua Zhang, Duwen Zhang, Minghai He**

Department of Anesthesiology, Guizhou Provincial People's Hospital, China

**Abstract**

**Introduction.** Isoflurane anesthesia at the period of brain development can lead to neurotoxicity and long-term cognitive impairment. This study aimed to investigate the role of miR-497 on isoflurane-induced neurotoxicity.
**Material and methods.** Neonatal rats (P7) were subject to isoflurane for 2 h at P7, P9, and P11. MiR-497 and neuron apoptosis were evaluated in hippocampal tissue by qRT-PCR and western blot. Fear conditioning test and Morris water maze were performed to determine cognitive function. The cell viability of isolated hippocampal neuronal cells exposed to isoflurane was measured using MTT test. The regulation of phospholipase D1 (PLD1) by miR-497 in isolated hippocampal neuronal cells was evaluated by luciferase reporter assays and western blot. Immunohistochemistry and TUNEL staining were employed to examine the PLD1 expression and neuronal cell apoptosis in hippocampus of neonatal rats, respectively.
**Results.** Repeated isoflurane anesthesia led to neurons' apoptosis and long-term cognitive impairment. Isoflurane exposure led to apoptosis and viability reduction in hippocampal neuronal cells. MiR-497 was observed to be upregulated after isoflurane exposure both *in vivo* and *in vitro*. Knockdown of miR-497 attenuated isoflurane-induced neuronal cells apoptosis and viability reduction. Furthermore, PLD1 was predicted and then validated as a novel target of miR-497. miR-497 could negatively regulate PLD1 by binding to its 3'-untranslated region. Downregulation of PLD1 was also observed after isoflurane exposure in neonatal rat hippocampus and hippocampal primary neuronal cell cultures.
**Conclusions.** Induction of miR-497 was involved in isoflurane anesthesia-induced cognitive impairment and neuronal cell apoptosis by targeting PLD1. miR-497 may be a novel potential mechanism in isoflurane-induced neurotoxicity so that our findings provide new insight into a better and understanding of the clinical application of isoflurane. *(Folia Histochemica et Cytobiologica 2021, Vol. 59, No. 2, 114–123)*

**Key words:** isoflurane; neurotoxicity; rat pups; hippocampal neurons; miR-497; phospholipase D1; cognitive impairment; qPCR; western blot

## Introduction

Early exposure to anesthetic agents is deleterious to nervous system development, impairs learning and memory, this neurocognitive dysfunction will even persist into later adulthood [1]. As millions of young children are exposed to anesthesia every year for various reasons, and there is raising concern about risks that may result from anesthesia exposure. Studies have shown that children who received multiple anesthesias are likely to develop a learning disability [2, 3]. Animal studies have found that both intravenous and inhalation anesthetic agents can cause central nerve cell apoptosis, especially during the critical period of

**Correspondence address:** Dr Fangxiang Zhang
Guizhou Provincial People's Hospital,
Guiyang, Guizhou 550002, China
phone: 0851-85922979
e-mail: fwz123ab@163.com

brain development [4–6]. It was demonstrated that in postnatal day 7 (P7) inhalation of anesthetic isoflurane by rat pups increased neuronal cell apoptosis, especially in thalamic nuclei [7], and inhibited the proliferation of neural progenitor cells in hippocampus, which ultimately led to poor learning and memory in P7 rats; however, the same administration of isoflurane to P60 rats seemed to play an opposite role [1]. Although a rising number of studies have focused on anesthesia-induced detrimental effects on cognitive function [8–10], it is still insufficient to understand the underlying mechanisms.

MicroRNAs (miRNAs) are small non-coding RNAs that complementarily bind to the 3'-untranslated region (3'-UTR) of targets to regulate their expression [11]. The highly multitudinous miRNAs have been involved in the regulation of neurodevelopment, neuronal inflammation, neuronal degeneration and apoptosis, cognition, memory, and other processes [12, 13]. For example, Mai *et al.* showed that intranasal injection of miR-146a can reduce the cognitive dysfunction in a murine Alzheimer's disease model, and that miR-146a exerts an inhibitory effect on amyloid $\beta$ (A$\beta$) precipitation, tau protein phosphorylation, and neuroinflammation in the hippocampus [14]. Some recent studies have found that the use of anesthetics has an effect on the expression of miRNAs in the brain, and more in-depth studies have shown a link between the expression of miRNAs and cognitive impairment associated with anesthesia [15–18].

The highly conserved *miR-195/497* cluster is located on human chromosome 17p13.1 [19]. Yin *et al.* found an increase of miR-497 expression in the brain tissue of transient middle cerebral artery occlusion (MCAO) mice. Further studies found that the knocking down of miR-497 can reduce the neuronal apoptosis caused by oxygen and glucose deprivation [20]. Another study demonstrated that the expression of miR-497 in neuroblastoma cell exposed to ethanol was significantly increased, and miR-497 was subsequently proved to play an important regulatory role in the nerve cells apoptosis induced by ethanol by targeting anti-apoptosis protein BCL2 [21]. These studies indicated that miR-497 may play an important role in neuronal apoptosis.

In this study, we used neonatal rats and primary neuronal cell cultures exposed to isoflurane to detect the expression of miR-497, and the effects of miR-497 on neurotoxicity induced by isoflurane was investigated by downregulating the expression of miR-497. The present study aimed to investigate the potential mechanism underlying the effect of miR-497 on learning and memory impairment in isoflurane-treated rats and may provide a theoretical basis for the molecular

mechanism of isoflurane in the clinical treatment of neuronal damage.

## Materials and methods

Experimental procedures were carried out in strict accordance with the recommendations in the Guide for the Care and Use of Laboratory Animals of the Guizhou Provincial People's Hospital and the protocol was approved by the Hospital.

**Animals.** Seven-day-old (P7) Sprague-Dawley male rat pups were randomly assigned to two groups: the control group (n = 20) and isoflurane group (n = 20). Rats in the isoflurane group were exposed for 2 h to 2% isoflurane in 25% oxygen in a temperature-controlled chamber, and the isoflurane exposure was conducted on postnatal (P) days P7, P9, and P11. The time and concentration of isoflurane exposure was selected according to previous research with some modifications [22, 23]. Rats in the control group received control gas (25% oxygen) in a similar chamber for 2 h. The chamber was kept in a homeothermic incubator to maintain the temperature at 37°C. After 24 h of the last exposure, half of the rat pups from each group were euthanized by intraperitoneal injection of pentobarbital sodium (150 mg/kg; Sigma-Aldrich, St. Louis, MO, USA) overdose, the brains were dissected, and the hippocampus of each brain was immediately frozen in liquid nitrogen and stored at –80°C for western blot and qRT-PCR analysis. The remaining animals were used for a behavioral study to determine their cognitive function after 7 weeks (at P57).

**TUNEL staining and immunohistochemistry.** The dissected hippocampus was immediately immersed in 4% formaldehyde at 4°C for 24 h and then embedded in paraffin. The embedded tissue was then sectioned into 5 $\mu$m slides. As for TUNEL staining, a commercial TUNEL Apoptosis Detection Kit (Millipore, Billerica, MA, USA) was employed according to the manufacturer's instruction. Briefly, the sections were deparaffinized and dehydrated using xylene and ethanol. After rehydration, the sections were rinsed with phosphate-buffered saline (PBS) and incubated with proteinase K, followed by incubation with TUNEL reaction mixture for 1 h at 37°C, then further stained using DAPI. The sections were examined under a laser scanning confocal microscope LSM710 (Carl Zeiss, Jena, Germany).

For immunohistochemistry, the paraffin-embedded sections were deparaffinized and dehydrated as described above, and then incubated with anti-PLD1 antibody (sc-28314, 1:50, Santa Cruz Biotechnology, Santa Cruz, CA, USA) at 4°C for 12 h. After washing, the sections were incubated with HRP-conjugated secondary antibody for 1.5 h at room temperature (RT) and then stained with diaminobenzidine tetrachloride (DAB) and counterstained with hematoxylin.

**Isolation and primary cultures of hippocampal neurons.** The brains of Sprague-Dawley rat embryos (E18) were dissected, and primary cultures were isolated as reported previously [24]. Briefly, the hippocampus was dissected from the brain, followed by trituration dissociation and enzymatic digestion (0.3% trypsin), and seeded in poly-D-lysine-precoated 6-well plates (Corning, NY, USA). Cultures were maintained in a humidified incubator with 5% $CO_2$ at 37°C in Neurobasal medium (Gibco, Frederick, MD, USA) with 2 mM glutamine, 2% B27, 100 units/mL penicillin, and 100 mg/mL streptomycin. The density of neurons in plates was $10^6$ cells/cm². Treatments were performed on the 6th day *in vitro*.

**Cell viability assays.** Primary neurons were exposed to normal air (control group), 2% (ISO-2 group), or 5% (ISO-5 group) isoflurane for the indicated time. The cell viability was measured using 3-(4, 5-dimethylthiazol-2-yl)-2, 5-diphenyltetrazolium bromide (MTT) (Sigma-Aldrich, Taufkirchen, Germany). After 24 h of the exposure to the indicated doses of isoflurane, primary neuronal cells were cultured at normal air for 1, 3 and 7 days, cell viability was determined by incubation with 25 $\mu$l 0.5 mg/mL of MTT reagent at 37°C for 4 h, followed by the addition of 150 $\mu$l dimethyl sulphoxide (DMSO) to resolve the generated formazan. The absorbance at a wavelength of 570 nm was measured using a microplate reader. Data were collected from 3 independent experiments.

**RNA extraction and quantitative real-time PCR (qRT-PCR).** Total RNA was isolated from hippocampal tissue samples and neurons cell by Trizol reagent (Invitrogen, Grand Island, NY, USA). RNAs were reverse transcribed into cDNA using miScript Reverse Transcription Kit (QIAGEN, Dusseldorf, Germany) following the manufacturer's protocol. qRT-PCR was performed with SYBR Premix EX Taq TM II (Takara, Dalian, China) on the real time PCR detection system ABI7900 (Thermo Fisher Scientific, Waltham, MA, USA). GAPDH or U6 was used as the internal reference, and relative expression was calculated by $2^{-\Delta\Delta Ct}$ method. The primer sequences were as follows: miR-497-F: GTCGTATCCAGTGCAGGGTCCGAGGT; R: ATTCGCACTGGATACGACTACAAACC; GAPDH-F: GTGAACCATGAGAAGTATGACAAC; R: CATGAGTCCTTCCACGATACC; U6-F: GCTTCGGCAGCACATATACTAAAAT; R: CGCTTCACGAATTTGCGTGTCAT.

**Luciferase assay.** The 3'-UTR of phospholipase D1 (PLD1) harboring the seed sequence of the miR-497 wild-type binding sites or mutant binding sites was inserted into the pmirGLO dual-luciferase vector (pmirGLO Vector) containing firefly and renilla luciferase genes (Promega, Madison, WI, USA). The wild-type or the mutant dual-luciferase vectors were co-transfected with 20 nM miR-497 mimic or inhibitor or their negative control into 293T cells using Lipofectamine 2000 (Invitrogen) according to the manufacturer's instructions. After 48 h of transfection, cells were harvested, and luciferase activity was detected using the Dual-Luciferase Assay System (Promega). The ratio of firefly activity to renilla activity was defined as the relative reporter activity. All experiments were performed in triplicate.

**Transfection of neurons.** The miR-497 mimic or inhibitor or their negative control was transfected into the primary neuron using Lipofectamine 2000 (Invitrogen) according to the manufacturer's instructions. The final concentration of small RNAs was 50 nM.

**Western blot analysis.** Ground tissue or neurons were lysed with RIPA lysis buffer, and the protein concentration was quantified using BCA protein assay kit (Beyotime, Shanghai, China). Following the extraction of total proteins, 20 $\mu$g of proteins were loaded and separated on 10% sodium dodecyl sulfate polyacrylamide gels. The separated proteins were transferred onto polyvinylidene fluoride membrane (Millipore). After blocking with nonfat dry milk (2.5%), the membranes were incubated with primary antibodies overnight at 4°C. The next day, membranes washed with TBST for every ten minutes were incubated with secondary antibodies conjugated with Horse Radish Peroxidase (HRP) for 1 h at RT. Antibodies used were as followed: anti-cleaved caspase 3 (ab2302, 1:1000, Abcam, Cambridge, MA, USA), anti-$\beta$-actin (ab8226, 1:1000, Abcam), anti-PLD1 (ab50695, 1:1000, Abcam). The membranes were subsequently incubated with HRP-conjugated secondary antibodies and detected with Pierce™ ECL Plus Western Blotting Substrate (32134, Thermo Fisher Scientific). The images were captured with SmartView Pro 2000 (UVCI-2100, Major Science, Saratoga, CA, USA). The bands were analyzed using Image J (version 1.8.0_112, National Institutes of Health, Bethesda, MD, USA).

**Morris water maze.** To assess the learning and memory functions of juvenile rats, animals from all the groups were subjected to the Morris water maze test at P60. A platform located at a fixed position in a circular water pool (100 cm in diameter, 80 cm in height) was submerged 2 cm below the water surface. The water temperature was set at 23°C. The training was conducted twice per day for seven consecutive days. During the trials, the swimming animals were forced to find the hidden platform within a maximum of 60 s. If the rat failed to find the platform within 60 s, it would be manually guided to the platform and allowed to stay on it for 15 s. The time spent on locating the platform (latency) was recorded and analyzed. The probe trials were performed on the 8th day, the platform was removed, then,
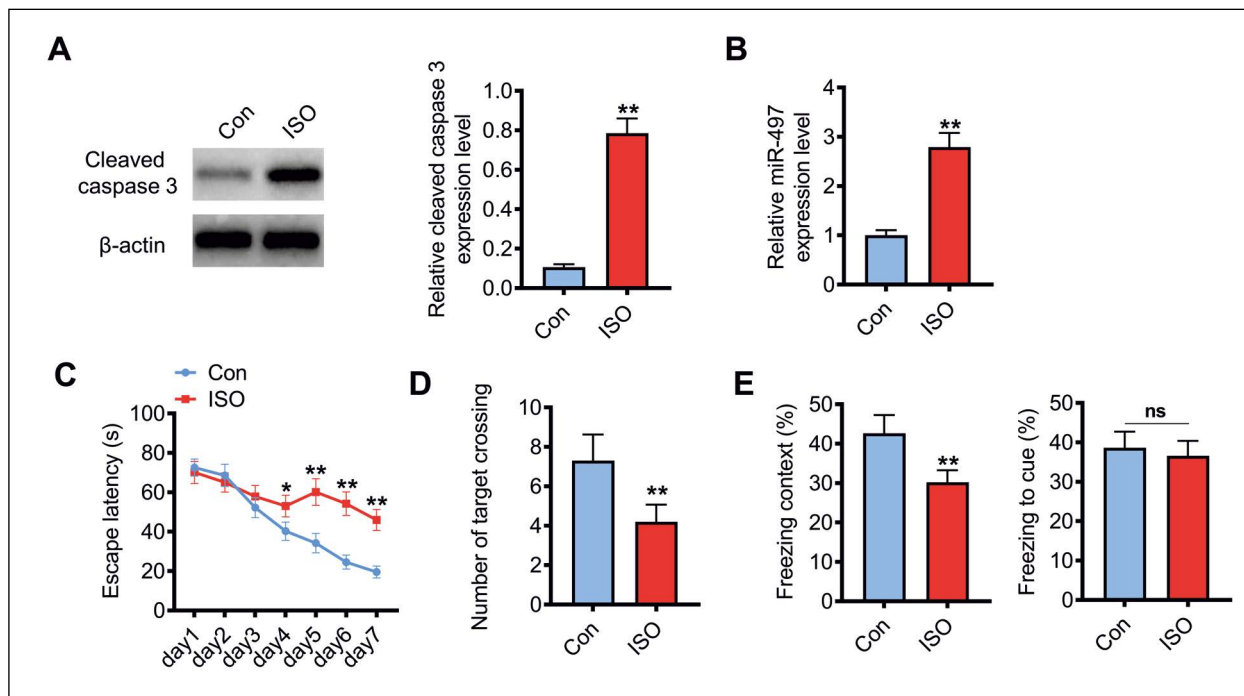
**Figure 1.** Isoflurane (ISO) anesthesia-induced neurotoxicity and miR-497 expression level in neonatal rat hippocampus. **A.** The expression of cleaved caspase 3 (western blot) and **(B)** miR-497 expression (RT-qPCR) in neonatal rat hippocampus after exposure of rat pups to ISO at the postnatal (P) day 7, P9, and P11 (P7, P9, and P11) (n = 10). **C.** Place trial demonstrating latency for rats to reach platform measuring spatial reference memory and learning as described in Methods. **D.** Probe trial demonstrating the target platform crossing times of juvenile rats in Morris water maze. **E.** The freezing time to context and the freezing time to cue in the fear conditioning test (n = 10). Fear conditioning test was performed at P57, Morris water maze was performed at P60 on the same rat. $*p < 0.05$, $**p < 0.01$, compared with the control group.

the number of times the rats crossed the area where the platform was located in the target quadrant was recorded. The entire test was recorded and analyzed by an MS-type Water Maze Video analysis system (Chengdu Instrument Ltd., Chengdu, China).

**Fear conditioning test.** On P57, rats were subjected to fear conditioning test. Each animal was placed in a conditioning chamber with a stainless-steel shock grid floor. The rats were allowed to explore the chamber for 3 min for adaption, and then rats were given for 30 sec tone-foot shock (80 dB, 1 kHz) followed by a 2-s foot shock (1.0 mA), this process was repeated 3 times with an intertribal interval of 60 s. Then, the animal was removed from the test chamber 60 sec after conditioning training. The contextual fear memory was measured 24 h after training for 5 min by placing the rat back in the original training chamber to monitor freezing behavior. The cued fear memory was tested 24 h after training, and the rats were placed in a novel chamber that had different context and smell with a continuous 3-min training tone presentation to monitor freezing behavior. Freezing behavior, defined as the absence of all visible movement of the body except for respiration, was recorded by a video camera with a high resolution on top of the chamber.

**Statistical analysis.** Statistical analyses were performed using SPSS 19.0 software (IBM SPSS Inc., Chicago, IL, USA) and Prism 7.0 software (GraphPad Software, La Jolla, CA, USA). Behavioral studies were analyzed with two-way ANOVA (treatment and time). Other data were analyzed using Student's $t$-test and one-way ANOVA. All the values were presented as the mean $\pm$ SD. $P < 0.05$ was considered statistically significant.

## Results

### Expression of miR-497 was upregulated in hippocampus of neonatal rats induced by isoflurane

After isoflurane exposure on P7, P9, and P11, the hippocampus of the neonatal rat (n = 10) was sampled. Isoflurane exposure increased cleaved caspase 3 as indicated in Figure 1A. To determine whether miR-497 is associated with isoflurane exposure, the expression level of miR-497 was detected using qRT-PCR. The result suggested that miR-497 was significantly upregulated nearly 2.7-fold after isoflurane exposure compared to the control (Fig. 1B). These results may imply the involvement of miR-497 in isoflurane-induced neurotoxicity. The rest of the rats (n = 10) were keeping feeding till P57. The
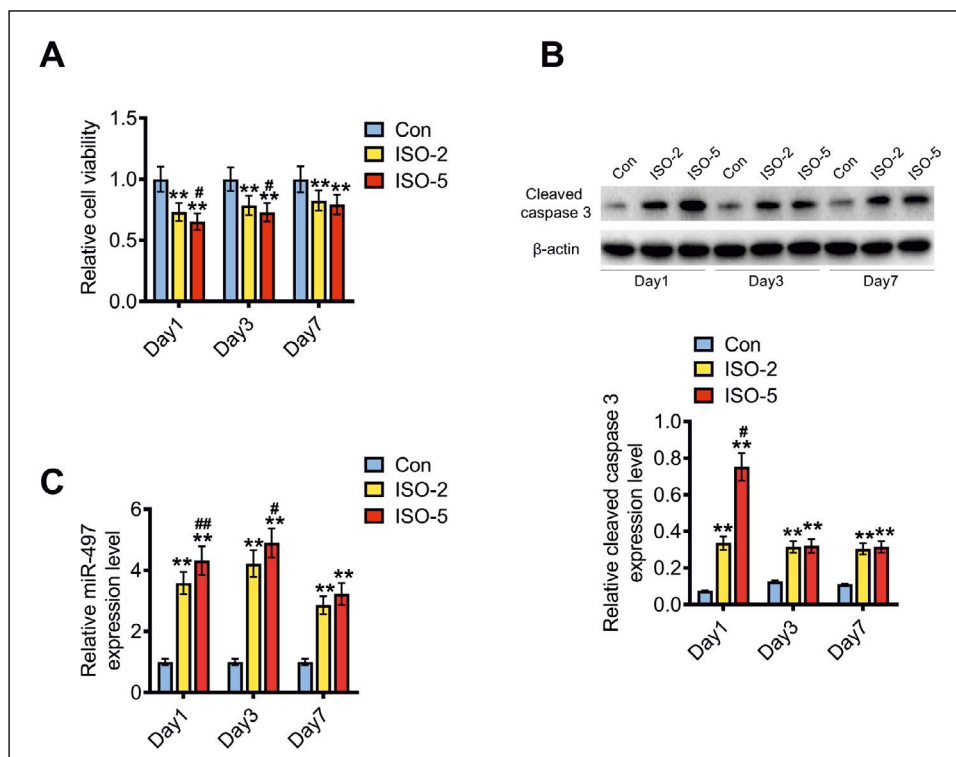
**Figure 2.** Isoflurane-induced neurotoxicity and miR-497 expression in primary cultures of hippocampal neurons. Neurons were cultured for 7 days and then exposed to two doses of isoflurane (ISO-2, 2% isoflurane; ISO-5, 5% isoflurane) for 24 h. **(A)** Cell viability (MTT test), **(B)** cleaved caspase 3 (western blot), and **(C)** miR-497 expression (RT-qPCR) were detected on the following days (D1, D3, D7). $**p < 0.01$, compared with control group, $^{#}p < 0.05$, $^{##}p < 0.01$, compared with ISO-2 group.

long-term neurocognitive impairment induced by isoflurane was evaluated by fear conditioning test and Morris water maze. As indicated in Figure 1C, rats exposed to isoflurane spent more time to find a submerged platform than the sham group. In the probe test, the number of platform crossing of rats exposed to isoflurane was reduced compared to the control group (Fig. 1D). In fear conditioning test, the freezing time of rats exposed to isoflurane decreased compared to that of the sham group (Fig. 1E). These results implied that multiple exposures to isoflurane in newborns may lead to long-term cognitive impairment.

***Upregulation of miR-497 induced by isoflurane was associated with apoptosis of neurons in primary culture***
Primary neurons cells isolated from rat embryos were exposed to 2% or 5% isoflurane for 24 h, the cell viability was measured at 1, 3, and 7 days after isoflurane exposure using MTT test. As indicated in Figure 2A, isoflurane exposure impaired neurons' viability, and a higher concentration of isoflurane exerted higher toxicity, moreover, the impaired viability of neurons was observed even 7 days after isoflurane exposure. The increased level of cleaved caspase 3, which is

a marker of cell apoptosis, was also observed after isoflurane exposure (Fig. 2B). The expression of miR-497 was significantly increased after isoflurane exposure, especially at 3 days after exposure (Fig. 2C). These results suggest isoflurane impairs neurons viability and induces apoptosis, and miR-497 may be involver in this process.

***MiR-497 inhibition mitigated isoflurane-induced apoptosis of hippocampal neurons in primary culture***
To examine the role of miR-497 in isoflurane-induced neurotoxicity, miR-497 inhibitor, or its negative control was transfected into primary neurons before isoflurane exposure. The transfection efficiency of miR-497 was confirmed by real-time PCR (Fig. 3A). After 7 days of 2% isoflurane exposure, the impaired cell viability of neurons cell induced by isoflurane was significantly alleviated with miR-497 inhibitor transfection (Fig. 3B). The miR-497 inhibition also decreased the level of cleaved caspase 3, which was dramatically induced by isoflurane exposure (Fig. 3C). These results suggested the protective role of miR-497 inhibition in neurotoxicity induced by isoflurane.
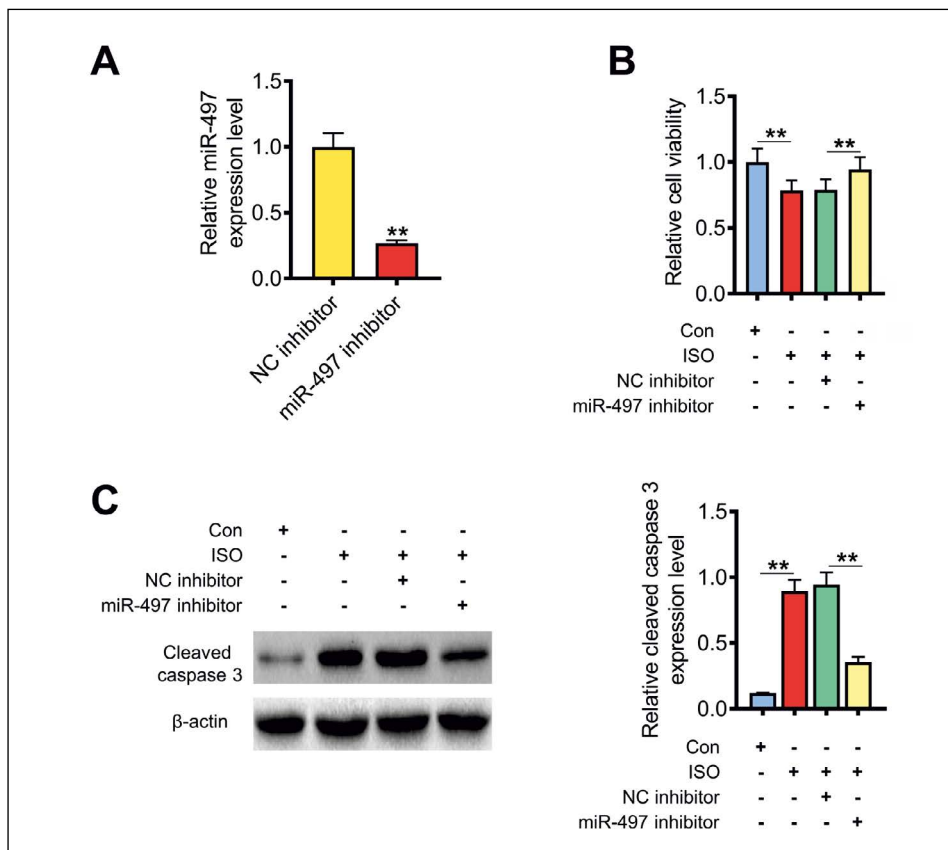
**Figure 3.** MiR-497 inhibitor ameliorated isoflurane-induced neurotoxicity in primary cultures of hippocampal neurons. **A.** Relative expression levels of miR-497 (RT-qPCR) in neuronal cells transfected with miR-497 inhibitor or negative control. **B.** Viability of cells transfected with miR-497 inhibitor or negative control followed by 2% isoflurane exposure for 24 h. **C.** Expression of cleaved caspase 3 (western blot) in primary neuronal cell transfected with miR-497 inhibitor or negative control followed by 2% isoflurane exposure for 24 h. **\*\***$p < 0.01$.

### MiR-497 suppressed PLD1 expression by direct binding at the 3'UTR

To explore the mechanism of miR-497 in isoflurane-induced neurotoxicity, the TargetScan (http://www.targetscan.org/vert_72/) was used for predicting the target gene of miR-497, and PLD1 was predicted to be a potential target of miR-497 (Fig. 4A). Luciferase reporter assay was carried out to validate the direct interaction between miR-497 and PLD1. The 3'UTR region of PLD1 containing wide-type or mutant miR-497 binding sites was cloned into the pmirGLO vector. HEK-293T cells were co-transfected with reporter plasmids and miR-497 mimic or inhibitor or their negative control. As shown in Figure 4B, the ectopic expression of miR-497 significantly repressed luciferase activity, whereas miR-497 inhibition enhanced the luciferase activity. In contrast, 3'UTR mutations completely abrogated the effect of miR-497 on luciferase activity. Besides, the protein level of PLD1 was determined in neurons with miR-497 overexpression or inhibition. Overexpression of miR-497 repressed protein levels of PLD1, while

miR-497 inhibition had the opposite effect (Fig. 4C). Furthermore, PLD1 was also detected in neurons treated with the indicated concentration of isoflurane and rat hippocampus after isoflurane anesthesia. As indicated in Fig. 4D, the protein level of PLD1 was dramatically suppressed after isoflurane exposure.

### Isoflurane exposure downregulated PLD1 expression and prompted neuronal cell death in rat pup's hippocampus

We next detected the expression of PLD1 in rat pup's hippocampus after isoflurane exposure at days P7, P9 and P11. After isoflurane exposure, the protein abundance of PLD1 was reduced in hippocampus (Fig. 5A). Our IHC results demonstrated a dramatic reduction of PLD1-positive cells in hippocampus (Fig. 5B). The neuronal cell death in rat hippocampus was determined using TUNEL staining, and the results indicated an increasing portion of TUNEL-positive cells after isoflurane exposure (Fig. 5C). These results indicated that isoflurane exposure suppressed the expression of PLD1, and led to neurons cells death in rat pup's hippocampus.
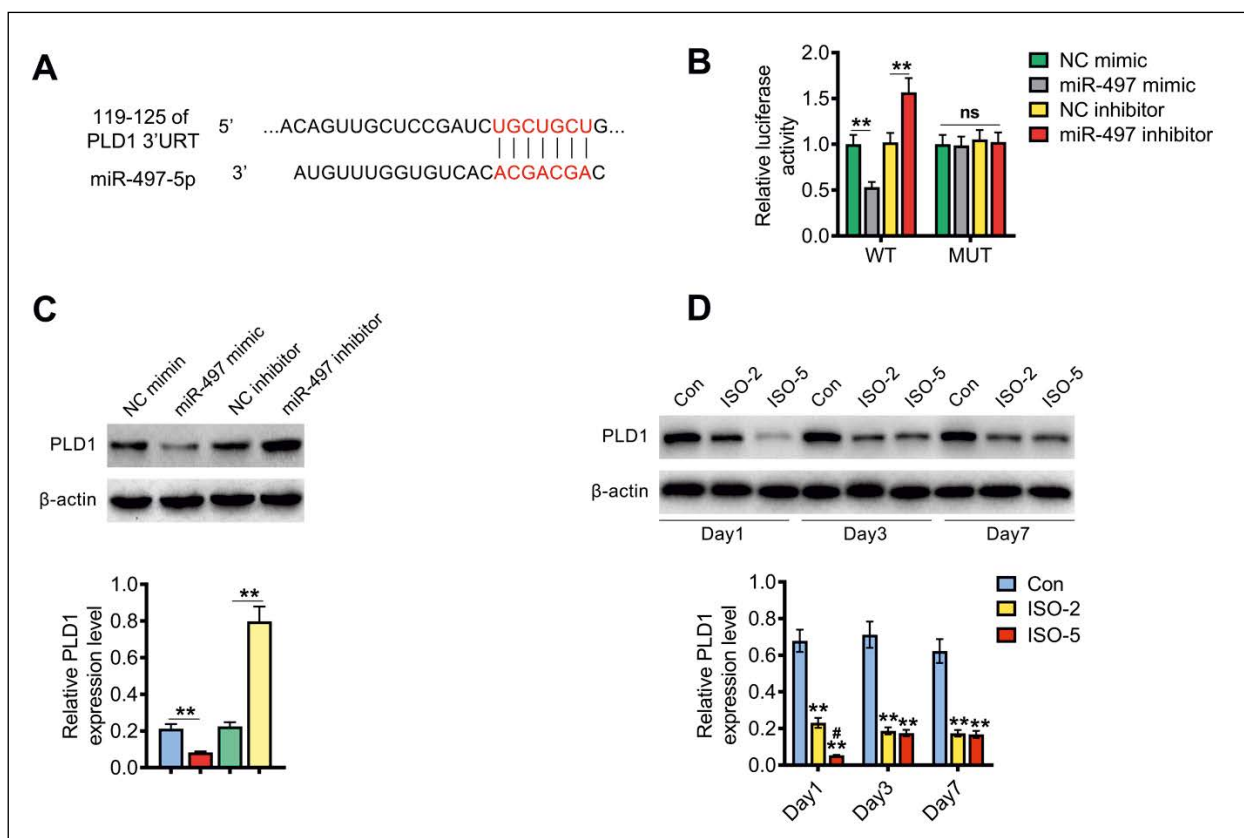
**Figure 4.** Phospholipase D1 (PLD1) is a novel target of miR-497. **A.** The predicted binding sites of miR-497 on 3'UTR of PLD1 based on TargetScan. **B.** Luciferase reporter assay was performed in HEK-293T cells to detect luciferase activity after co-transfection with miR-497 mimic, miR-497 inhibitor, or their negative control and dual-luciferase vector of 3'-UTR of PLD1 harboring the seed sequence of the miR-497 wild-type binding sites (WT) or mutant binding sites (MUT). **C.** PLD1 protein expression (western blot) in primary neuronal cells transfected with miR-497 mimic, miR-497 inhibitor, or their negative control for 48 h. $**p < 0.01$, compared with NC mimic or NC inhibitor group. **D.** PLD1 protein expression (western blot) in primary neuronal cells subjected to 2% and 5% isoflurane for 24 h after the indicated days of culture. $**p < 0.01$, compared with control group, $^{\#}p < 0.05$, compared with ISO-2 group.

## Discussion

In the present study, we showed that multiple isoflurane exposure of neonatal rats caused apoptosis of hippocampal neurons and led to long-term impairment of cognitive and learning functions. There are numerous reports which showed that single or multiple isoflurane exposure at neonatal period will lead to cognitive impairment. For instance, rats repeatedly exposed to isoflurane on P7 were found to have a long-term impaired of cognitive function, however, the cognitive impairments induced by a single exposure to isoflurane varied by gender [22]. The long-term impairment induced by neonatal isoflurane exposure perhaps largely results from neuronal apoptosis in the developing brain. As indicated in other study in which single isoflurane anesthesia of rats from 1 to 14 postnatal day, the highest level of apoptotic neuronal death was induced in neonatal

rats at P7, the lowest neuronal apoptosis was seen in P14 rats. This finding could be explained by the fact that P7 rats are more vulnerable to be damaged since at this age the peak of synaptogenesis takes place [25]. Interestingly, some studies demonstrated that adult and aged rodents exposed to isoflurane also developed cognitive impairment [23, 26, 27]. Zhong *et al.* found that neonatal male mice exposed repeatedly to isoflurane exhibited dysregulated hippocampal H4K12 acetylation and decreased c-Fos expression, and administration of a histone deacetylase inhibitor could attenuate the impairment [28]. An another report revealed the possibility of the activation of hypoxia inducible factor-1$\alpha$ (HIF-1$\alpha$) in isoflurane-induced neonatal neurotoxicity [29]. Additionally, TLR2/NF-$\kappa$B pathway was proved to be involved in isoflurane-induced neurotoxicity [30]. Although great efforts have been done in elucidating the developmental neurotoxicity of isoflurane, the
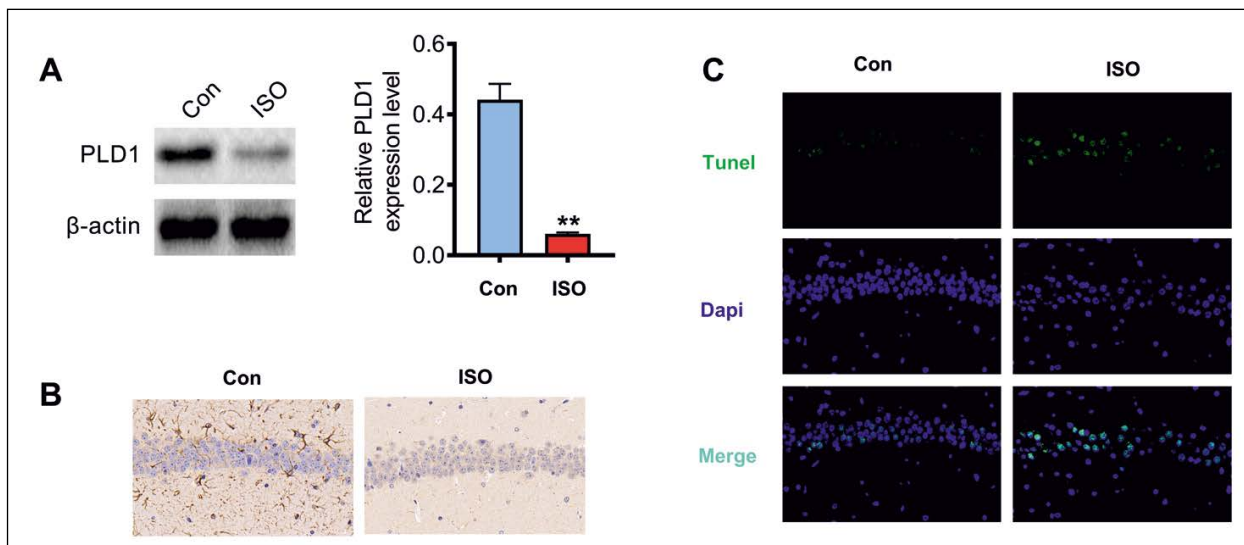
**Figure 5.** Isoflurane exposure downregulated PLD1 expression and prompted neuronal cell death in rat pup's hippocampus. After 3 independent isoflurane exposures at days P7, P9 and P11, the protein expression of PLD1 in rat pup's hippocampus (24 h after the last exposure) was examined by western blot (A) and immunohistochemistry (CA1) (B). C. Death of hippocampal neurons was evaluated using TUNEL assay in hippocampal CA1 after isoflurane exposure. Magnification for (B) and (C): 200×.

underlying mechanisms have not been completely clarified so far.

The involvement of the crucial roles of miRNAs in various human diseases has been widely demonstrated. Besides, some recent studies also indicated that miRNAs may participate in neurotoxicity induced by isoflurane. For instance, miR-142-5p was found to be upregulated in neurological impairment caused by isoflurane in neonatal rats, whereas the inhibition of miR-142-5p exerted neuroprotective effects against isoflurane, reflected by a better behavior performance [31]. Moreover, isoflurane facilitated the expression of miR-140-5p in diabetic rat hippocampus, which led to the post-transcriptional suppression of sorting protein nexin 12, and the depletion of sorting nexin 12 subsequently contributed to isoflurane neurotoxicity [32].

The main purpose of our study focuses on the role of miR-497 in isoflurane-induced neurons apoptosis and long-term cognitive impairment. Here, we showed that neonatal rats and cultured hippocampal neurons subjected to isoflurane displayed an obvious induction of miR-497. To clarify the role of miR-497 in isoflurane-induced neurotoxicity, miR-497 depletion using miR-497 inhibitor was conducted in cultured neurons and our results confirmed the neuroprotective effect of miR-497, as assessed by increased cell viability and decreased apoptosis. It was previously reported that the induction of miR-497 in neuronal cells exposed to ethanol and overexpression of miR-497 in the absence of ethanol also leads to neuronal cell apoptosis [21]. miR-497 also plays a role in oxygen-glucose depri-

vation-induced neuronal cell death [20], implying the potential anti-apoptotic effect of miR-497 in the central nervous system.

Most importantly, our results further established PLD1 as a direct target of miR-497 in neuronal cells. PLD1 is a member of phospholipase D lipid-signaling enzyme superfamily and has been widely reported to function in various neuronal processes. The deficiency of PLD1 led in mice to defects in brain growth and cognitive function, moreover, upon stimulation the PLD-deficient mice released less acetylcholine than wild-type ones [33]. In addition, PLD1 was found to participate in BDNF-dependent nuclear recruitment of phospho-ERK1/2 and phospho-CREB, which may play role in neuronal development and induction of glutamatergic synapses, because it is known that BDNF plays a role in hippocampal long-term potentiations [34]. As synapses are responsible for information transmission, processing, and signal integration in the nervous system, PLD1 was found to promote the development of the dendritic spines by regulating N-cadherin [35]. A similar conclusion was drawn in another report: genetic or pharmacological inhibition of PLD1 or its upstream RSK2 would lead to the impairment of neuronal growth factor-induced neurite outgrowth [36]. A recent study revealed that PLD1 activation attenuates coflin-p53 pro-apoptotic pathway induced by amyloid *β*, exerting its role in anti-apoptosis of neuronal cells [37]. In our present study, isoflurane anesthesia suppressed the expression of PLD1 both in neonatal rat hippocampus and

primary neuronal cell cultures, which may be the potential mechanism of isoflurane-induced neurotoxicity. Moreover, PLD1 was validated as a novel target of miR-497 and was negatively regulated by miR-497. Hence, we inferred that isoflurane-induced the expression of miR-497 and consequently inhibited PLD1 to contribute to the apoptosis of neuronal cells. However, the effect of miR-497/PLD1 on cognitive impairment induced by isoflurane in neonatal rats need to be further investigated.

Taken together, our present research demonstrated that the involvement of miR-497 in isoflurane-induced neurotoxicity and long-term neurocognitive impairment, and clarified PLD1 as the downstream target of miR-497. This work may shed light on the underlying mechanisms of anesthetics-induced neurotoxicity and may contribute to developing novel therapeutic ways for isoflurane--related application.

## Acknowledgments

## Funding

## Availability of data and materials

All data generated or analyzed during this study are included in this published article.

## Authors' contributions

YYQ and FXZ designed the study, supervised the data collection and analyzed the data; JP and ZHZ interpreted the data and prepared the manuscript for publication; DWZ and MHH supervised the data collection, analyzed the data and reviewed the draft of the manuscript.
All authors have read and approved the manuscript.

## Ethics approval and consent to participate

The animal use protocol listed below has been reviewed and approved by the Animal Ethical and Welfare Committee.

## Conflict of interests

The authors declare that they have no competing interests, and all authors should confirm their accuracy.

## References

1. Stratmann G, Sall JW, May LDV, et al. Isoflurane differentially affects neurogenesis and long-term neurocognitive function in 60-day-old and 7-day-old rats. Anesthesiology. 2009; 110(4): 834–848, doi: 10.1097/ALN.0b013e31819c463d, indexed in Pubmed: 19293705.
2. Flick RP, Katusic SK, Colligan RC, et al. Cognitive and behavioral outcomes after early exposure to anesthesia and surgery. Pediatrics. 2011; 128(5): e1053–e1061, doi: 10.1542/peds.2011-0351, indexed in Pubmed: 21969289.
3. Sprung J, Flick RP, Wilder RT, et al. Anesthesia for cesarean delivery and learning disabilities in a population-based birth cohort. Anesthesiology. 2009; 111(2): 302–310, doi: 10.1097/ALN.0b013e3181adf481, indexed in Pubmed: 19602960.
4. Lu LX, Yon JH, Carter LB, et al. General anesthesia activates BDNF-dependent neuroapoptosis in the developing rat brain. Apoptosis. 2006; 11(9): 1603–1615, doi: 10.1007/s10495-006-8762-3, indexed in Pubmed: 16738805.
5. Creeley CE. From drug-induced developmental neuroapoptosis to pediatric anesthetic neurotoxicity-where are we now? Brain Sci. 2016; 6(3), doi: 10.3390/brainsci6030032, indexed in Pubmed: 27537919.
6. Cabrera OH, O'Connor SD, Swiney BS, et al. Caffeine combined with sedative/anesthetic drugs triggers widespread neuroapoptosis in a mouse model of prematurity. J Matern Fetal Neonatal Med. 2017; 30(22): 2734–2741, doi: 10.1080/14767058.2016.1261400, indexed in Pubmed: 27924651.
7. Stratmann G, May LDV, Sall JW, et al. Effect of hypercarbia and isoflurane on brain cell death and neurocognitive dysfunction in 7-day-old rats. Anesthesiology. 2009; 110(4): 849–861, doi: 10.1097/ALN.0b013e31819c7140, indexed in Pubmed: 19293696.
8. Yang S, Gu C, Mandeville ET, et al. Anesthesia and surgery impair blood-brain barrier and cognitive function in mice. Front Immunol. 2017; 8: 902, doi: 10.3389/fimmu.2017.00902, indexed in Pubmed: 28848542.
9. Yu D, Li L, Yuan W. Neonatal anesthetic neurotoxicity: Insight into the molecular mechanisms of long-term neurocognitive deficits. Biomed Pharmacother. 2017; 87: 196–199, doi: 10.1016/j.biopha.2016.12.062, indexed in Pubmed: 28056424.
10. Clausen NG, Hansen TG, Disma N. Anesthesia neurotoxicity in the developing brain: basic studies relevant for neonatal or perinatal medicine. Clin Perinatol. 2019; 46(4): 647–656, doi: 10.1016/j.clp.2019.08.002, indexed in Pubmed: 31653300.
11. Piscopo P, Lacorte E, Feligioni M, et al. MicroRNAs and mild cognitive impairment: A systematic review. Ageing Res Rev. 2019; 50: 131–141, doi: 10.1016/j.arr.2018.11.005, indexed in Pubmed: 30472218.
12. Sun E, Shi Y. MicroRNAs: Small molecules with big roles in neurodevelopment and diseases. Exp Neurol. 2015; 268: 46–53, doi: 10.1016/j.expneurol.2014.08.005, indexed in Pubmed: 25128264.
13. Issler O, Chen A. Determining the role of microRNAs in psychiatric disorders. Nat Rev Neurosci. 2015; 16(4): 201–212, doi: 10.1038/nrn3879, indexed in Pubmed: 25790865.
14. Mai H, Fan W, Wang Y, et al. Intranasal administration of miR-146a agomir rescued the pathological process and cognitive impairment in an AD mouse model. Mol Ther Nucleic Acids. 2019; 18: 681–695, doi: 10.1016/j.omtn.2019.10.002, indexed in Pubmed: 31707205.
15. Goto G, Hori Y, Ishikawa M, et al. Changes in the gene expression levels of microRNAs in the rat hippocampus by sevoflurane and propofol anesthesia. Mol Med Rep. 2014; 9(5): 1715–1722, doi: 10.3892/mmr.2014.2038, indexed in Pubmed: 24626427.
16. Zhang N, Ye W, Wang T, et al. Up-regulation of miR-106a targets LIMK1 and contributes to cognitive impairment induced by isoflurane anesthesia in mice. Genes Genomics. 2020; 42(4): 405–412, doi: 10.1007/s13258-019-00913-8, indexed in Pubmed: 31933141.
17. Yan H, Xu T, Zhao H, et al. Isoflurane increases neuronal cell death vulnerability by downregulating miR-214. PLoS

One. 2013; 8(2): e55276, doi: 10.1371/journal.pone.0055276, indexed in Pubmed: 23408966.

18. Lu X, Lv S, Mi Y, et al. Neuroprotective effect of miR-665 against sevoflurane anesthesia-induced cognitive dysfunction in rats through PI3K/Akt signaling pathway by targeting insulin-like growth factor 2. Am J Transl Res. 2017; 9(3): 1344–1356, indexed in Pubmed: 28386360.

19. Itesako T, Seki N, Yoshino H, et al. The microRNA expression signature of bladder cancer by deep sequencing: the functional significance of the miR-195/497 cluster. PLoS One. 2014; 9(2): e84311, doi: 10.1371/journal.pone.0084311, indexed in Pubmed: 24520312.

20. Yin KJ, Deng Z, Huang H, et al. miR-497 regulates neuronal death in mouse brain after transient focal cerebral ischemia. Neurobiol Dis. 2010; 38(1): 17–26, doi: 10.1016/j.nbd.2009.12.021, indexed in Pubmed: 20053374.

21. Yadav S, Pandey A, Shukla A, et al. miR-497 and miR-302b regulate ethanol-induced neuronal cell death through BCL2 protein and cyclin D2. J Biol Chem. 2011; 286(43): 37347–37357, doi: 10.1074/jbc.M111.235531, indexed in Pubmed: 21878650.

22. Murphy KL, McGaughy J, Croxson PL, et al. Long-term effects of neonatal single or multiple isoflurane exposures on spatial memory in rats. Front Neurol. 2013; 4(1): 87–95, doi: 10.3389/fneur.2013.00087, indexed in Pubmed: 23847588.

23. Lin D, Zuo Z. Isoflurane induces hippocampal cell injury and cognitive impairments in adult rats. Neuropharmacology. 2011; 61(8): 1354–1359, doi: 10.1016/j.neuropharm.2011.08.011, indexed in Pubmed: 21864548.

24. Yan J, Huang Y, Lu Yi, et al. Repeated administration of ketamine can induce hippocampal neurodegeneration and long-term cognitive impairment via the ROS/HIF-1$\alpha$ pathway in developing rats. Cell Physiol Biochem. 2014; 33(6): 1715––1732, doi: 10.1159/000362953, indexed in Pubmed: 24923288.

25. Yon JH, Daniel-Johnson J, Carter LB, et al. Anesthesia induces neuronal cell death in the developing rat brain via the intrinsic and extrinsic apoptotic pathways. Neuroscience. 2005; 135(3): 815–827, doi: 10.1016/j.neuroscience.2005.03.064, indexed in Pubmed: 16154281.

26. Li XM, Zhou MT, Wang XM, et al. Resveratrol pretreatment attenuates the isoflurane-induced cognitive impairment through its anti-inflammation and -apoptosis actions in aged mice. J Mol Neurosci. 2014; 52(2): 286–293, doi: 10.1007/s12031-013-0141-2, indexed in Pubmed: 24126892.

27. Kong F, Chen S, Cheng Y, et al. Minocycline attenuates cognitive impairment induced by isoflurane anesthesia in aged

rats. PLoS One. 2013; 8(4): e61385, doi: 10.1371/journal.pone.0061385, indexed in Pubmed: 23613842.

28. Zhong T, Guo Q, Zou W, et al. Neonatal isoflurane exposure induces neurocognitive impairment and abnormal hippocampal histone acetylation in mice. PLoS One. 2015; 10(4): e0125815, doi: 10.1371/journal.pone.0125815, indexed in Pubmed: 25928815.

29. Chai D, Jiang H, Li Q. Isoflurane neurotoxicity involves activation of hypoxia inducible factor-1$\alpha$ via intracellular calcium in neonatal rodents. Brain Res. 2016; 1653: 39–50, doi: 10.1016/j.brainres.2016.10.014, indexed in Pubmed: 27769790.

30. Pang X, Zhang P, Zhou Y, et al. Dexmedetomidine pretreatment attenuates isoflurane-induced neurotoxicity via inhibiting the TLR2/NF-$\kappa$B signaling pathway in neonatal rats. Exp Mol Pathol. 2020; 112: 104328, doi: 10.1016/j.yexmp.2019.104328, indexed in Pubmed: 31678237.

31. Xie C, Wang H, Zhang Yu, et al. Neuroprotective effects of miR-142-5p downregulation against isoflurane-induced neurological impairment. Diagn Pathol. 2020; 15(1): 70, doi: 10.1186/s13000-020-00978-0, indexed in Pubmed: 32505188.

32. Fan D, Yang S, Han Y, et al. Isoflurane-induced expression of miR-140-5p aggravates neurotoxicity in diabetic rats by targeting SNX12. J Toxicol Sci. 2020; 45(2): 69–76, doi: 10.2131/jts.45.69, indexed in Pubmed: 32062618.

33. Burkhardt U, Stegner D, Hattingen E, et al. Impaired brain development and reduced cognitive function in phospholipase D-deficient mice. Neurosci Lett. 2014; 572: 48–52, doi: 10.1016/j.neulet.2014.04.052, indexed in Pubmed: 24813107.

34. Ammar MR, Thahouly T, Hanauer A, et al. PLD1 participates in BDNF-induced signalling in cortical neurons. Sci Rep. 2015; 5: 14778, doi: 10.1038/srep14778, indexed in Pubmed: 26437780.

35. Luo LD, Li G, Wang Y. PLD1 promotes dendritic spine development by inhibiting ADAM10-mediated N-cadherin cleavage. Scientific Reports. 2017; 7(1), doi: 10.1038/s41598-017-06121-2, indexed in Pubmed: 28729535.

36. Ammar MR, Humeau Y, Hanauer A, et al. The Coffin-Lowry syndrome-associated protein RSK2 regulates neurite outgrowth through phosphorylation of phospholipase D1 (PLD1) and synthesis of phosphatidic acid. J Neurosci. 2013; 33(50): 19470–19479, doi: 10.1523/JNEUROSCI.2283-13.2013, indexed in Pubmed: 24336713.

37. Liu T, Wang F, LePochat P, et al. Cofilin-mediated Neuronal Apoptosis via p53 Translocation and PLD1 Regulation. Sci Rep. 2017; 7(1): 11532, doi: 10.1038/s41598-017-09996-3, indexed in Pubmed: 28912445.

ORIGINAL PAPER

# Astragalus polysaccharide protects formaldehyde--induced toxicity by promoting NER pathway in bone marrow mesenchymal stem cells

Yali She[1, 2]\*, Xiaowen Zhao[1]\*, Pingfan Wu[1], Ling Xue[1], Zhe Liu[1], Meng Zhu[1], Jie Yang[1], Yaling Li[1, 2]

[1]Department of Pathology, School of Basic Medicine, Gansu University of Chinese Medicine, Lanzhou, Gansu, China

[2]Provincial-Level Key Laboratory of Molecular Medicine of Major Diseases and Study on Prevention and Treatment of Traditional Chinese Medicine, Gansu University of Chinese Medicine, Lanzhou, Gansu, China

\*These authors contributed equally to this work.

**Abstract**

**Introduction.** In our previous study, it has been confirmed that formaldehyde (FA) not only inhibits the proliferative activity, but also causes DNA-protein crosslinks (DPCs) formation in bone marrow mesenchymal stem cells (BMSCs). The purpose of this study was to detect the protective effect of astragalus polysaccharide (APS) against the cytotoxicity and genotoxicity of BMSCs exposed to FA, and to explore potential molecular mechanisms of APS activity.

**Material and methods.** Human BMSCs were cultured *in vitro* and randomly divided into control cells (Ctrl group), FA-treated cells (FA group, 120 $\mu$mol/L), and cells incubated with FA and increasing concentrations (40, 100, or 400 $\mu$g/mL) of APS (FA + APS groups). Cytotoxicity was measured by MTT assay. DNA strand breakage, DNA-protein crosslinks (DPCs), and micronucleus formation were respectively detected by comet assay, KCl-SDS precipitation assay, and micronucleus assay. The mRNA and protein expression level of xeroderma pigmentosum group A (XPA), xeroderma pigmentosum group C (XPC), excision repair cross-complementation group 1 (ERCC1), replication protein A1 (RPA1), and replication protein A2 (RPA2) were all detected by qRT-PCR and Western Blot.

**Results.** Compared with the FA group, the cytotoxicity, DNA strand breakage, DPCs, and micronucleus levels were decreased significantly in FA + APS groups ($P < 0.01$). Meanwhile, the mRNA and protein expression of XPA, XPC, ERCC1, RPA1, and RPA2 were up-regulated significantly in the FA + APS groups ($P < 0.05$) with the most prominent effect of the 100 $\mu$g/mL APS.

**Conclusions.** Our results suggest that APS can protect the cytotoxicity and genotoxicity of human BMSCs induced by FA. The mechanism may be associated with up-regulated expression of XPA, XPC, ERCC1, RPA1, and RPA2 in the nucleotide excision repair (NER) pathway which promotes DNA damage repair. *(Folia Histochemica et Cytobiologica 2021, Vol. 59, No. 2, 124–133)*

**Key words:** astragalus polysaccharide; formaldehyde; bone marrow mesenchymal stem cells; toxicity; NER pathway; DNA strand breakage; DNA-protein crosslinks; micronucleus formation

**Correspondence address:** Yaling Li, MD
Provincial-Level Key Laboratory of Molecular
Medicine of Major Diseases and Study on Prevention
and Treatment of Traditional Chinese Medicine,
Gansu University of Chinese Medicine, Lanzhou, Gansu, China
phone 808-692-1554, fax: 808-692-1973
e-mail: liyaling_09@sina.com

## Introduction

As one component of bone marrow (BM), bone marrow mesenchymal stem cells (BMSCs) not only have multi-differentiation potential, but also can regulate the normal proliferation and differentiation of hematopoietic stem cells [1, 2]. Thus, if BMSCs undergo toxic damage, BMSCs will lose their normal control over hematopoietic stem cells which may lead to myeloid leukemia.

Formaldehyde (FA), an environmental pollutant, is widely present in pollution, tobacco smoke and home accessories [3, 4]. The International Agency for Research on Cancer (IARC) indicated that FA may cause leukemia but the mechanisms remain unclear [4]. FA exhibits toxic effects in various types of mammalian cells, including cultured human myeloid progenitor cells and bone marrow blood progenitor cells *in vivo* [5, 6]. In our previous study, it has been confirmed that FA induced the excessive DNA-protein crosslinks (DPCs) in murine BMSCs [7].

The formation of DPCs is related to oxidative damage caused by FA-induced excessive hydroxyl free radicals [8–10]. DPCs are the primary DNA damage products induced by FA, and the level of DPCs is considered to be a good molecular dosimeter to assess FA-related cancer risk [11]. When FA induces DNA damage, such as DPCs, the cell activates repair mechanisms to reverse the damage to reestablish stability of the genome. The nucleotide excision repair (NER) pathway is an important way for DNA damage repair, which mainly repairs the cyclobutane pyrimidine dimer, DNA adducts, and cross-linking between chains [12, 13]. It was found that the repair of FA-induced DPCs mainly depends on the NER pathway [14].

Astragalus membranaceus, belonging to the Leguminosae family, is used as a Qi-tonifying herb in traditional Chinese medicine [15]. Astragalus polysaccharide (APS), one of the active ingredients of Astragalus, has been shown to possess antioxidant, immunomodulatory, and tumor growth inhibitory properties in modern studies [16–18]. Numerous animal and anecdotal human data show that APS has anticancer effects in preclinical studies [19], as well as can improve myelosuppression induced by cytotoxic agents and chemopreventive effects [20]. APS enhanced the secretion of granulocyte colony-stimulating factor (G-CSF) and maintained the stability of the bone marrow hematopoietic microenvironment after chemotherapy [21]. In addition, APS could inhibit ionizing radiation-induced bystander effects in BMSCs [22] as well as inhibit apoptosis and senescence of BMSCs caused by ferric ammonium citrate iron overload [23].

The present study was performed to characterize the protective effect of APS against the cytotoxicity and genotoxicity of BMSCs exposed to FA. Subsequently, we used the qRT-PCR and Western Blot to assess the expression of xeroderma pigmentosum group A (XPA), xeroderma pigmentosum group C (XPC), excision repair cross-complementation group 1 (ERCC1), replication protein A1 (RPA1), and replication protein A2 (RPA2) genes in the NER pathway in FA- and APS-exposed BMSCs to explore potential molecular mechanisms of APS's activity.

## Materials and methods

**Cell culture.** Human BMSCs (Cyagen Biosciences Inc, Santa Clara, CA, US) were cultured in Dulbecco's Modified Eagel Media: Nutrient Mixture F-12 1:1 Mixture (D-MEM//F12) supplemented with 10% fetal bovine serum for stem cells, 315 mg/L D-glucose and glutamine (all from Cyagen Biosciences, Santa Clara, CA, USA) at 37°C in a humidified incubator with 5% $CO_2$ (SANYO Electric CO., Ltd, Osaka, Japan). During the logarithmic growth period, the cells were detached with 0.25% trypsin-0.02% EDTA.

**Preparation of astragalus polysaccharide (APS) and formaldehyde (FA).** The mass fraction of APS (Solarbio Science & Technology Co., Ltd., Beijing, China) was more than 98%. APS was dissolved and diluted to the final concentration of 40, 100, 400 $\mu$g/mL with D-MEM/F12. FA's (SigmaAldrich, St. Louis, MO, USA) mass fraction was more than 37%. FA was diluted with D-MEM/F12 to the final concentration of 120 $\mu$mol/L.

**Groups.** BMSCs were randomly divided into control group, FA group, and FA + APS 40, 100 and 400 $\mu$g/mL groups. In the control group, the cells were cultured with D-MEM/F-12. The cells in the FA group were cultured with 120 $\mu$mol/L FA of D-MEM/F-12. BMSCs co-cultured with 120 $\mu$mol/L FA and 40, 100, 400 $\mu$g/mL APS of D-MEM/F-12 served as FA + APS 40, 100 and 400 $\mu$g/mL groups. FA and APS were added at the same time and incubated together with BMSCs for 24 h.

**MTT assay.** Cell proliferation activity was measured by MTT assay. The number of cells was adjusted to $4 \times 10^3$ per well and inoculated on 96-well plates. Then MTT (Biowest, Loire Valley, France) 20 $\mu$L was added into cells and incubated for 4 h. The supernatant was discarded and then DMSO was added before oscillation. The absorbance (A) value was measured at 490 nm with the enzyme marker (Bio-Rad, Hercules, CA, USA). The cell proliferation rate of each experimental group was calculated according to the formula: cell proliferation rate = (A experiment — A blank)/(A control — A blank) ×100%.

**Table 1.** The sequence of each primer in qRT-PCR

| mRNA | | Primer sequence | Product length |
|---|---|---|---|
| XPA | Forward primer | 5'-CTACTGGAGGCATGGCTAAT-3' | 132bp |
| | Reverse primer | 5'-CCATAACAGGTCCTGGTTGA-3' | |
| XPC | Forward primer | 5'-ACTGCGCAGCCAGAAATCC-3' | 107bp |
| | Reverse primer | 5'-CTTTGGAGAGAAGGCTCTTC-3' | |
| ERCC1 | Forward primer | 5'-ATGGACCCTGGGAAGGACA-3' | 133bp |
| | Reverse primer | 5'-TCTGTGTAGATCGGAATAAGG-3' | |
| RPA1 | Forward primer | 5'-ATGCAGAAGGGGGATACAA-3' | 145bp |
| | Reverse primer | 5'-ACTGTGTCGCCAACATGAA-3' | |
| RAP2 | Forward primer | 5'-ATGACAGCTGCACCCATG-3' | 124bp |
| | Reverse primer | 5'-TGTTCTGAAAAGATCTCAGG-3' | |

**Comet assay.** Comet assay was used to detect DNA strand breakage. The normal 1% melting point agarose gel (Biowest) was prepared on frosted-glass slides. The cell suspension was spread onto normal 1% melting point agarose gel after it was mixed with 1% low melting point agarose (volume ratio: 1:3) and then immersed in a lysis buffer containing 40% proteinase K (Promega, Madison, WI, USA) for lysis. Then it was immersed into the electrophoresis buffer for 30 min at 4°C in the darkness under the voltage of 15 V, the current of 300 mA. It was fixed with 1% $H_2O_2$ and stained with propidium iodide (PI) for 30 min. Cells were observed under IX81 fluorescence microscope (Olympus, Tokyo, Japan) and photographed. Twenty cells were randomly selected from each treatment group and the collected images were analyzed with comet experiment professional analysis software CASP (version 1.2.3; Bio-Rad). Olive tail moment (OTM), an internationally recognized value, was used to evaluate DNA strand breakage. The OTM value is equal to the distance between the center of mass and the density of the comet head and tail × the DNA content of the comet tail.

**DNA-protein crosslinks formation assay.** DPCs formation was detected by KCl-SDS precipitation (KCl-SDS) precipitation assay. 2% SDS solution was added to cells that in the logarithmic growth stage, and the cells were lysed in the water bath at 65°C. Then 1 mol/L of KCl was added to the cells for fully mixing and an ice bath was used for 5 min to form SDS-K$^+$ precipitation. The pellet and supernatant containing free DNA were collected after centrifugation. The collected precipitate was added with 40% protease K and digested in a water bath at 50°C. The supernatant containing DNA in DPCs was collected after centrifugation. 1 mL of the supernatant containing free DNA and cross-linked DNA was taken and Hoechst33258 (Biyuntian Biotechnology Co., Ltd., Shanghai, China) was added to it for staining for 30 min. The standard curve was based on calf thymus DNA. Fluorescence values of each group were measured by RF-5301PC fluorescence spectrometer (Shimadzu, Tokyo,

Japan) under excitation light at 353 nm and emission light at 455 nm. The concentrations of free DNA and cross-linked DNA were quantified according to the standard curve. The DPCs level was calculated by the following formula: DPCs = cross-linked DNA concentration/(cross-linked DNA concentration + free DNA concentration) ×100%.

**Micronucleus assay.** Cells were digested by trypsin and collected. Then hypotonic KCl solution was used for 3 min. Finally, the cells were fixed, dripped, and stained by Giemsa (Solarbio). One thousand cells were randomly observed on each slide. Most of the micronucleus contained in the cells were round with smooth, neat edges. Their diameter was 1/16-1/3 of the main nucleus, without refraction, not connected with the main nucleus, and consistent with chromophile, purplish or blue-purple. One or more micronucleus could appear in a cell. The number of cells with micronuclei is counted. Micronucleus cell rate (‰) = total number of cells with micronucleus/total number of observed cells × 1000‰.

**Quantitative real time polymerase chain reaction (qRT--PCR) assay.** The expression of mRNA XPA, XPC, ERCC1, RPA1, and RPA2 were detected by qRT-PCR. Cells in the logarithmic growth phase were taken. Total RNA was extracted using TRIzol Reagent (Invitrogen, Carlsbad, CA, USA) and reverse transcribed to cDNA using the RT$^2$ First Strand Kit according to the manufacturer's instructions (Qiagen, Duesseldorf, Germany). Gene expression level was detected according to the instructions of the RT$^2$ SYBR® Green qPCR Mastermix (Qiagen). qRT-PCR was performed in CFX96™ Thermal Cycler (Bio-Rad). The formula $\Delta$ Ct = Ct average — average Ct of housekeeping genes, $\Delta\Delta$ Ct = $\Delta$ Ct (experimental group) — $\Delta$ Ct (control group), was used to calculate $\Delta$ Ct and $\Delta\Delta$ Ct value of the gene expression. 2-$\Delta\Delta$Ct was used to calculate the relative gene expression level of the experiment group. The primer details of XPA, XPC, ERCC1, RAP1, and RAP2 were shown in Table 1.

**Western blot analysis.** Western blot detected the expression of XPA, XPC, ERCC1, RPA1, and RPA2 proteins. Cells in the logarithmic growth stage were taken and 200 $\mu$L lysate solution (Biyuntian Biotechnology) was added. Cells were scraped with a cell scraper, collected, and centrifuged. Then the supernatant was collected and the loading buffer, at a ratio of 1:3, was added into supernatant before boiling it at 98°C and setting aside in the refrigerator at –20°C. The protein was separated by electrophoresis with 12% polyacrylamide gel. After membrane transfer with PVDF (Millipore Corporation, Burlington, MA, USA), the protein was sealed for 2 h by skimmed milk. The XPA, XPC, ERCC1, RAP1, and RAP2 antibody (1:1000, all from Ruiying Biological Co., Ltd.) was incubated at 4°C overnight and the goat anti-rabbit antibody (1:4000, Ruiying Biological Co., Ltd.) was incubated at room temperature for 2 h. The image was developed with ECL light agent (Cyagen Biosciences). The grayscale ratio of each target band and corresponding GAPDH was analyzed by Quantity One image analysis software (Bio-Rad) to represent the relative expression level of each protein.

**Statistical analysis.** Homogeneity test of variance and one-way ANOVA were used for comparison between groups. The statistical analysis of data obtained from each experiment used SPSS 26.0 for Windows software (Microsoft Corporation, Redmond, WA, USA). Values represented mean ± standard deviation. The vakues *, # [upper index) = zk] and **, ## denote P < 0.05 and P < 0.01, respectively which were considered to be statistically significant.

## Results

### Protective effect of APS against cytotoxicity in BMSCs exposed to FA

MTT assay was used to determine the cytotoxicity by calculating the proliferation rate of human BMSCs. MTT results (Fig. 1) showed that the cytotoxicity in FA-treated BMSCs increased significantly compared with control cells ($P < 0.01$) and cytotoxicity decreased significantly in cells incubated with FA plus APS at 40, 100 and 400 $\mu$g/mL compared with FA-treated BMSCs ($P < 0.01$). Among them, 100 $\mu$g/mL APS had the highest protective effect against cytotoxicity in BMSCs exposed to FA.

### Protective effect of APS against DNA breakage in BMSCs exposed to FA

We used comet assay to identify DNA breakage in human BMSCs and DNA breakage was quantified as the OTM. The results (Fig. 2) showed that DNA breakage in BMSCs induced by FA was remarkably higher than that in control cells ($P < 0.01$). Compared with the FA-treated BMSCs, DNA breakage was significantly reduced in cells incubated with FA plus
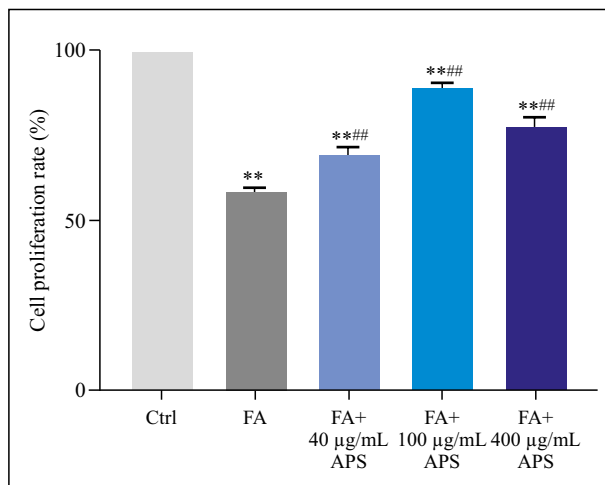


**Figure 1.** Astragalus polysaccharide (APS) reduced cytotoxicity in bone marrow mesenchymal stem cells (BMSCs) exposed to formaldehyde (FA). Human BMSCs were incubated in the D-MEM/F12 medium for 24 h in the presence of FA (120 $\mu$mol/L) and FA + APS at the concentrations of 40, 100 or 400 $\mu$g/mL as described in Methods. Cytotoxicity to BMSCs was determined by MTT test that assessed proliferation activity. Proliferation activity in human BMSCs exposed to FA decreased significantly compared with control (Ctrl) group. Cell proliferation activity increased significantly compared with that in FA + APS groups. *$P < 0.05$, **$P < 0.01$ *vs.* Ctrl group. #$P < 0.05$, ##$P < 0.01$ *vs.* FA group.

APS at 40, 100 and 400 $\mu$g/mL ($P < 0.01$). Among them, DNA breakage of cells treated with FA and 100 $\mu$g/mL was the least, and there was no significant difference compared with Ctrl group.

### Protective effect of APS against DPCs in BMSCs exposed to FA

In order to determine DPCs formation in human BMSCs, KCl-SDS precipitation assay was used. The results (Fig. 3) showed that FA could significantly induce DPCs formation in BMSCs compared with Ctrl group ($P < 0.01$). Compared with the FA group, DPCs level was significantly reduced in cells incubated with FA plus APS at 40, 100 $\mu$g/mL ($P < 0.01$). However, when 400 $\mu$g/mL APS was used, the DPCs level increased but it was still significantly lower than that in the FA group ($P < 0.01$).

### Protective effect of APS against micronucleus in BMSCs exposed to FA

The micronucleus assay results (Fig. 4) showed that the micronucleus frequency of FA-treated BMSCs was significantly increased compared with control cells ($P < 0.01$), and the micronucleus frequency was significantly decreased by the incubation of the cells with FA plus APS at the concentrations of 40, 100, and
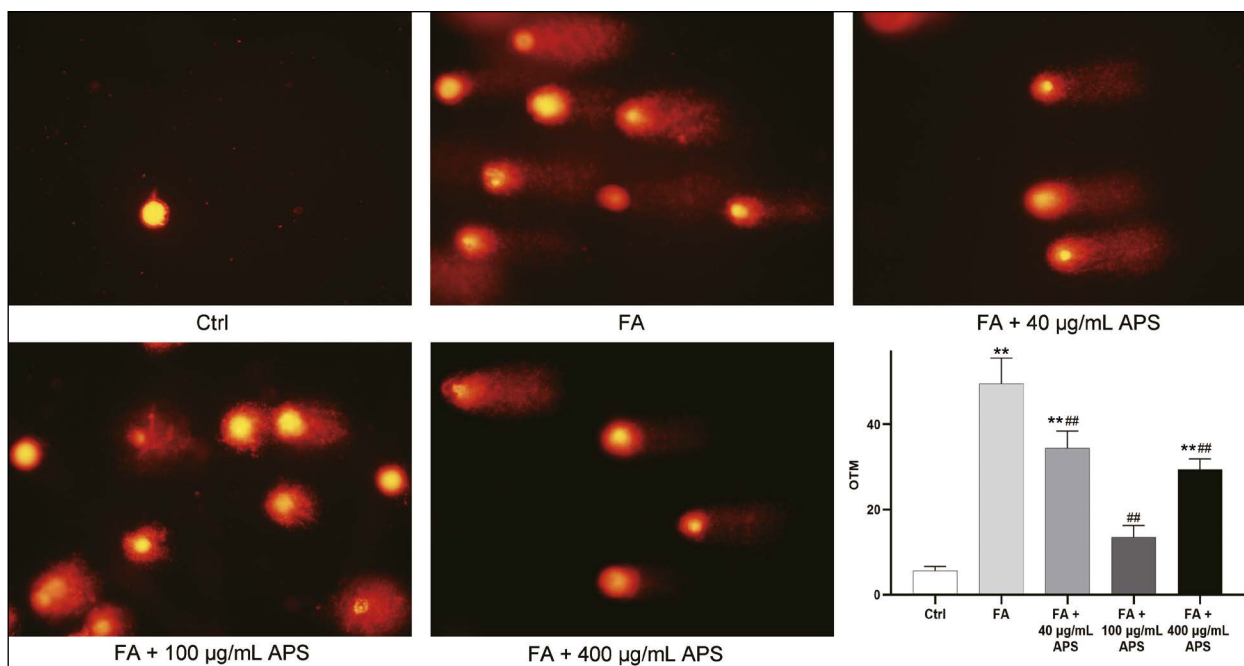
**Figure 2.** Astragalus polysaccharide (APS) reduced DNA breakage in BMSCs exposed to formaldehyde (FA). The comet assay was used to identify DNA breakage in human BMSCs. DNA breakage effect in human BMSCs exposed to FA was significantly higher than that in Ctrl group. Compared with FA group, DNA breakage in cells was significantly reduced in FA + APS groups. *$P < 0.05$, **$P < 0.01$ vs. control (Ctrl) group. #$P < 0.05$, ##$P < 0.01$ vs. FA group. Magnification: 400×.
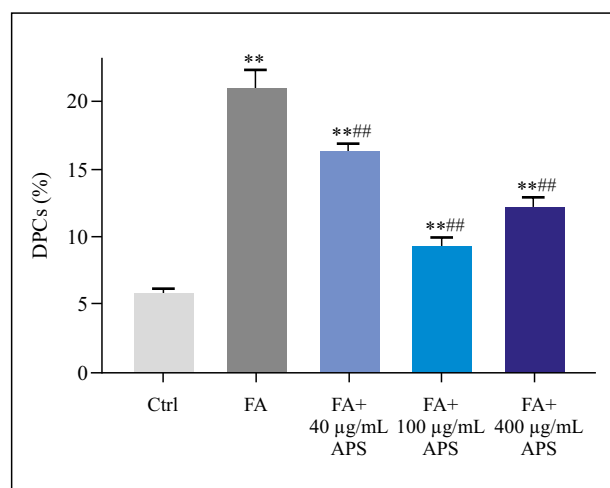


**Figure 3.** Astragalus polysaccharide (APS) reduced DNA-protein crosslinks (DPCs) in BMSCs exposed to formaldehyde (FA). DPCs was measured by KCl-SDS precipitation assay as described in Methods. FA significantly increased the formation of DPCs in human BMSCs compared with that in control (Ctrl) group. Compared with FA group, DPCs in cells was significantly decreased in FA + APS groups. *$P < 0.05$, **$P < 0.01$ vs. Ctrl group. #$P < 0.05$, ##$P < 0.01$ vs. FA group.

400 $\mu$g/mL ($P < 0.01$). The micronucleus frequency of cells treated with FA and 100 $\mu$g/mL APS was the lowest among the FA plus APS groups at different concentrations.

### Effect of APS on the expression of XPA, XPC, ERCC1, RPA1 and RPA2 genes in NER pathway of BMSCs exposed to FA

The results of qRT-PCR and Western blotting results (Fig. 5) showed that compared with the control cells, the expression of XPA protein, RPA1, RPA2 mRNA and protein were significantly down-regulated ($P < 0.01$), and XPA mRNA, XPC, ERCC1 mRNA and protein were significantly up-regulated in FA-treated BMSCs ($P < 0.01$, 0.05). Compared with the FA group, the mRNA and protein expression of XPA, XPC, ERCC1, RPA1, and RPA2 were all remarkably up-regulated in BMSCs incubated with FA plus each concentration of APS ($P < 0.01$, 0.05). Of note, the gene expression reached a peak in BMSCs treated with FA plus 100 $\mu$g/mL APS.

### Discussion

Our previous studies have confirmed that formaldehyde (FA) could inhibit the proliferative activity and enhance DNA-protein crosslinks (DPCs) formation in mice bone marrow mesenchymal stem cells (BMSCs) [7]. Therefore, the main purpose of this study was to investigate the protective effect of Astragalus polysaccharide (APS) against cytotoxicity and genotoxicity in human BMSCs exposed to FA and its potential mechanisms. In the present study, we found that the
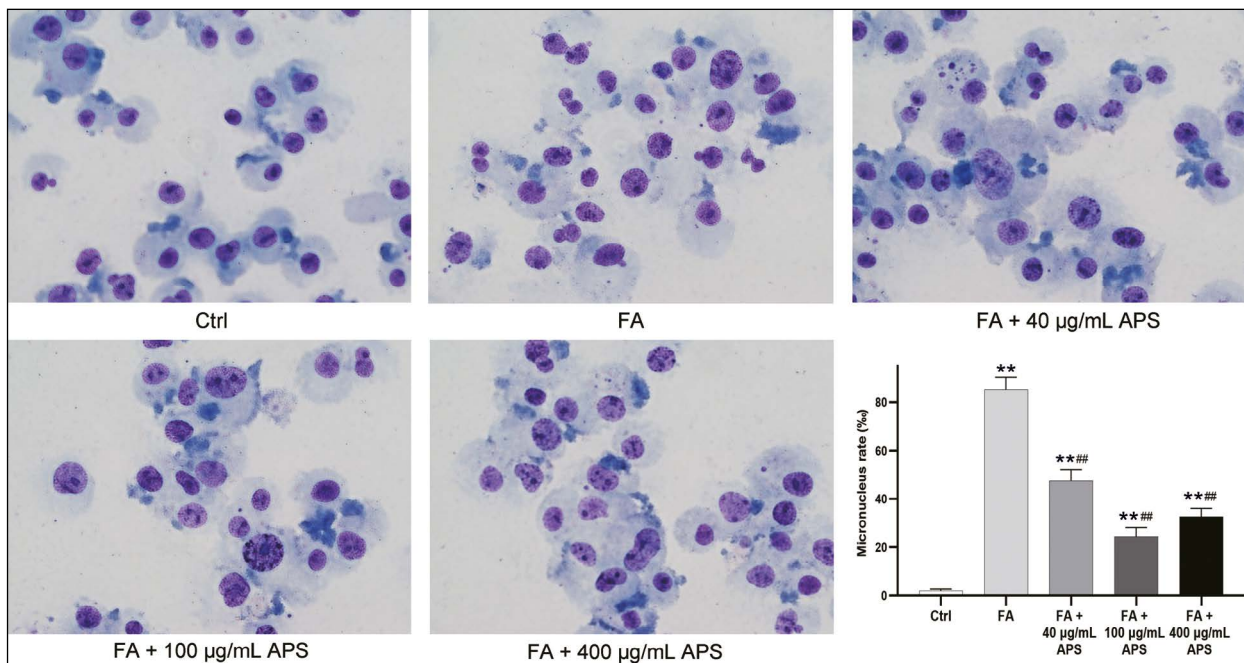
**Figure 4.** Astragalus polysaccharide (APS) decreased the micronucleus frequency in BMSCs exposed to formaldehyde (FA). The micronucleus frequency of human BMSCs was significantly increased in FA group compared with control (Ctrl) group. Compared with FA group, micronucleus frequency in cells was significantly decreased in FA + APS groups. *$P < 0.05$, **$P < 0.01$ *vs.* Ctrl group. #$P < 0.05$, ##$P < 0.01$ *vs.* FA group. Magnification: 400×.

proliferation activity decreased in BMSCs exposed to FA, but the proliferation activity significantly increased after the cells were incubated with FA plus APS. These indicated that APS could reduce the cytotoxicity induced by FA in human BMSCs.

DNA breakage and DPCs formation are considered to be the main forms of DNA damage caused by FA [24]. It has even been reported that DPCs is a molecular marker of FA-related cancer risk [11, 25]. DPCs are necessary for DNA replication, transcription, and cell growth in normal cells; however, excessive DPCs produced by endogenous and exogenous agents block DNA replication resulting in genomic instability and tumorigenesis [26–28]. In this study, the degree of genotoxicity in BMSCs exposed to FA was studied by detecting the levels of DNA breakage, DPCs, and micronucleus formation. It was found that DNA breakage, DPCs and micronucleus formation in BMSCs exposed to FA were increased compared with control cells, however, after treatment with APS, they were decreased. This indicates that APS may protect against genotoxicity in BMSCs exposed to FA. This is consistent with study showing that APS can maintain genomic stability and reduce DNA damage in BMSCs incubated with the irradiated A549 cells [22, 29].

When external factors induce DNA damage, the cells can mobilize relevant repair mechanisms to reverse these damages in order to maintain genetic sta-bility. The nucleotide excision repair (NER) pathway, the major mechanism in the process of DNA repair, primarily eliminates bulky adducts arising from exposure to environmental agents [30–32]. Xeroderma pigmentosum group A (XPA) and xeroderma pigmentosum group C (XPC) are the initial recognizing proteins responsible for the recruitment of relevant repair apparatus components to the DNA damage site [33–35]. Excision repair cross-complementation group 1 (ERCC1) has a global function in cellular DNA damage repair [36]. ERCC1 binds to XPF to form the ERCC1-XPF complex, which is responsible for cutting the damage-containing oligonucleotide [37, 38]. These core proteins involved in the NER reaction play a key role in the maintaining of genomic stability. Our study shows that the mRNA and protein expression levels of XPC and ERCC1 in FA-treated BMSCs were significantly higher than those in the control cells, indicating that XPC and ERCC1 may be involved in the repair of human BMSCs DNA damage caused by FA. This is in accordance with previous studies [7, 39]. The mRNA and protein expression levels of XPA, XPC, and ERCC1 in cells incubated with FA plus APS groups at different concentrations were significantly higher than those in the FA-treated cells. These findings demonstrate that APS promoted the repair of DNA damage by upregulating the mRNA and protein expressions of
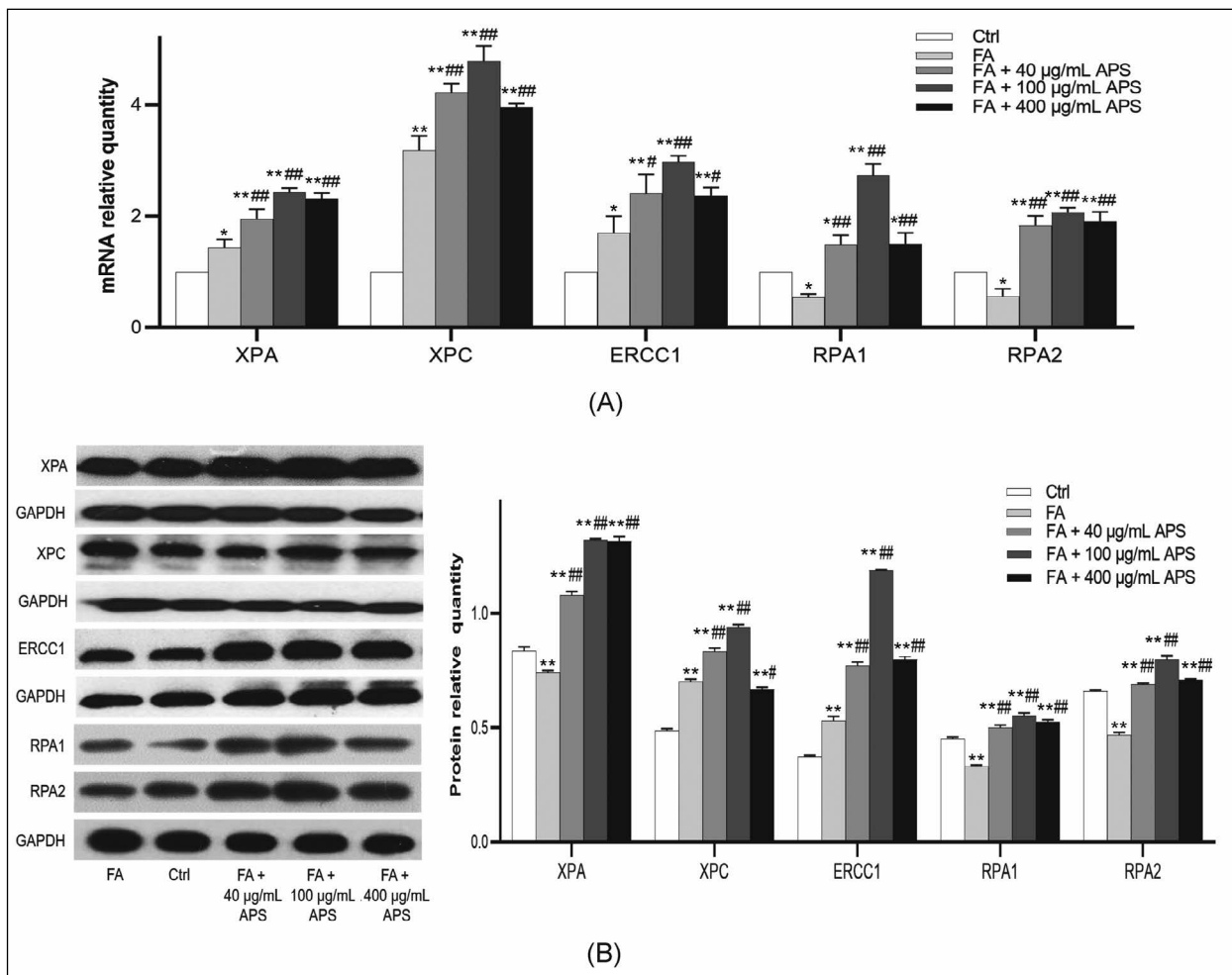
**Figure 5. A.** Astragalus polysaccharide (APS) up-regulated the mRNA expression of XPA, XPC, ERCC1, RPA1 and RPA2 in BMSCs exposed to formaldehyde. **B.** Astragalus polysaccharide (APS) up-regulated the protein expression of XPA, XPC, ERCC1, RPA1 and RPA2 in BMSCs exposed to formaldehyde. Relative levels of mRNA and protein content in the homogenates of BMSCs were measured by qRT-PCR and Western blotting as described in Methods. $*P < 0.05$, $**P < 0.01$ *vs.* control (Ctrl) group. $\#P < 0.05$, $\#\#P < 0.01$ *vs.* FA group.

XPA, XPC, and ERCC1, which was consistent with the results that APS significantly reduced the DNA breakage, DPCs, and micronucleus formation in human BMSCs exposed to FA. A similar mechanism of was demonstrated in other reports [40, 41]. In addition, the study also found that the expression level of XPA mRNA in BMSCs treated by FA was higher than that in Ctrl group, while the expression level of XPA protein was decreased, which may be related to protein degradation, or may be affected by miRNA, progressive regulation from the translation level so that the protein was not expressed or XPA mRNA was directly degraded.

Replication protein A (RPA), a eukaryotic single-stranded DNA binding protein, is composed of three related subunits: RPA1 (RPA70), RPA2 (RPA32), and RPA3 (RPA14). Much progress has

been made to elucidate the critical roles for RPA in DNA metabolic pathways that help promote genomic stability [42]. RPA is not only involved in the initiation, extension of DNA replication, and the organization of Okazaki fragments but is also involved in NER repair. RPA can protect single-stranded DNA from nuclear degradation and hairpin formation after DNA damage [43]. At the same time, RPA1 and RPA2 can bind to XPA to form the RPA-XPA complex, which is involved in the recognition of DNA damage [44]. In this study, we found that the mRNA and protein expression of RPA1, RPA2 decreased in FA-treated cells compared with control cells, indicating that RPA1, RPA2 did not participate in the repair of DNA damage caused by FA. On the other hand, DNA damage caused by FA blocks the cell cycle and DNA

replication, so the mRNA and protein expression of replication-related genes RPA1 and RPA2 were decreased in FA-treated cells. Compared with the FA group, the mRNA and protein expressions of RPA1, RPA2 in BMSCs incubated with FA plus each concentration of APS were significantly increased, suggesting that APS may promote the recognition of RPA1, RPA2, and DNA damage, and help in the formation of RPA-XPA complex, thus ensuring the smooth progression of NER. A similar mechanism of was demonstrated to be functional in study showing that XPA combined with RPA might be involved in damage-recognition in NER [40].

This study also found that the protective effect of APS on BMSCs treated by FA reached the peak when concentration of APS was 100 $\mu$g/mL. However, when APS mass concentration is greater than 100 $\mu$g/mL, APS may have toxic effects on BMSCs and aggravate DNA damage. These findings suggested that although APS may promote DNA repair, there is still a certain safe range of the mass concentration when it is used. However, the *in vitro* experiments, have a limited relevance to the whole body system. Drugs in the body have to go through absorption, distribution, and first-pass effects, and their functions are also affected by complex factors such as neuroendocrine and immune systems. Therefore, experiments *in vivo* are needed to further determine the effective concentration of APS or to link the concentration that produces toxicity *in vitro* with the corresponding dose *in vivo*.

In conclusion, APS has a significant protective effect against FA-induced cytotoxicity and genotoxicity of BMSCs, especially at the concentration of 100 $\mu$g/mL, which may be related to the up-regulation of gene expression of XPA, XPC, ERCC1, RPA1, and RPA2 in the NER pathway and the promotion of DNA damage repair. However, its specific safe dose range *in vivo* remains to be further studied and defined.

## Acknowledgment

## Conflict of interest

The authors hereby declare that they do not have any conflicting interest.

## References

1. Moore KA, Lemischka IR. Stem cells and their niches. Science. 2006; 311(5769): 1880–1885, doi: 10.1126/science.1110542, indexed in Pubmed: 16574858.
2. Méndez-Ferrer S, Michurina TV, Ferraro F, et al. Mesenchymal and haematopoietic stem cells form a unique bone marrow niche. Nature. 2010; 466(7308): 829–834, doi: 10.1038/nature09262, indexed in Pubmed: 20703299.
3. Zhang L, Freeman LE, Nakamura J, et al. Formaldehyde and leukemia: epidemiology, potential mechanisms, and implications for risk assessment. Environ Mol Mutagen. 2010; 51(3): 181–191, doi: 10.1002/em.20534, indexed in Pubmed: 19790261.
4. Chemical agents and related occupations. IARC Monogr Eval Carcinog Risks Hum. 2012; 100: 9–562, indexed in Pubmed: 23189753.
5. Zhang L, Tang X, Rothman N, et al. Occupational exposure to formaldehyde, hematotoxicity, and leukemia-specific chromosome changes in cultured myeloid progenitor cells. Cancer Epidemiol Biomarkers Prev. 2010; 19(1): 80–88, doi: 10.1158/1055-9965.EPI-09-0762, indexed in Pubmed: 20056626.
6. Liang X, Zhang J, Song W, et al. Formaldehyde exposure in indoor air from public places and its associated health risks in Kunshan City, China. Asia Pac J Public Health. 2018; 30(6): 551–560, doi: 10.1177/1010539518800348, indexed in Pubmed: 30221985.
7. She Y, Li Yi, Liu Y, et al. Formaldehyde induces toxic effects and regulates the expression of damage response genes in BM-MSCs. Acta Biochim Biophys Sin (Shanghai). 2013; 45(12): 1011–1020, doi: 10.1093/abbs/gmt105, indexed in Pubmed: 24077345.
8. Ortega-Atienza S, Wong VC, DeLoughery Z, et al. ATM and KAT5 safeguard replicating chromatin against formaldehyde damage. Nucleic Acids Res. 2016; 44(1): 198–209, doi: 10.1093/nar/gkv957, indexed in Pubmed: 26420831.
9. Zhang S, Chen H, Zhang J, et al. The multiplex interactions and molecular mechanism on genotoxicity induced by formaldehyde and acrolein mixtures on human bronchial epithelial BEAS-2B cells. Environ Int. 2020; 143: 105943, doi: 10.1016/j.envint.2020.105943, indexed in Pubmed: 32659531.
10. Liang FQ, Godley B. Oxidative stress-induced mitochondrial DNA damage in human retinal pigment epithelial cells: a possible mechanism for RPE aging and age-related macular degeneration. Exp Eye Res. 2003; 76(4): 397–403, doi: 10.1016/s0014-4835(03)00023-x.
11. Hubal EA, Schlosser PM, Conolly RB, et al. Comparison of inhaled formaldehyde dosimetry predictions with DNA-protein cross-link measurements in the rat nasal passages. Toxicol Appl Pharmacol. 1997; 143(1): 47–55, doi: 10.1006/taap.1996.8076, indexed in Pubmed: 9073591.
12. Latimer JJ, Johnson JM, Kelly CM, et al. Nucleotide excision repair deficiency is intrinsic in sporadic stage I breast cancer. Proc Natl Acad Sci U S A. 2010; 107(50): 21725–21730, doi: 10.1073/pnas.0914772107, indexed in Pubmed: 21118987.
13. Vrouwe MG, Pines A, Overmeer RM, et al. UV-induced photolesions elicit ATR-kinase-dependent signaling in non-cycling cells through nucleotide excision repair-dependent and

-independent pathways. J Cell Sci. 2011; 124(Pt 3): 435–446, doi: 10.1242/jcs.075325, indexed in Pubmed: 21224401.

14. Salem AMH, Nakano T, Takuwa M, et al. Genetic analysis of repair and damage tolerance mechanisms for DNA-protein cross-links in Escherichia coli. J Bacteriol. 2009; 191(18): 5657–5668, doi: 10.1128/JB.00417-09, indexed in Pubmed: 19617358.

15. Yeung K, Gubili J, Cassileth B. An evidence-based review of Astragalus membranaceus (Astragalus) for cancer patients. Evidence-based Anticancer Materia Medica. 2011: 65–84, doi: 10.1007/978-94-007-0526-5_3.

16. Jung Y, Jerng U, Lee S. A systematic review of anticancer effects of radix astragali. Chin J Integr Med. 2016; 22(3): 225–236, doi: 10.1007/s11655-015-2324-x, indexed in Pubmed: 26643507.

17. Wu J, Yu J, Wang J, et al. Astragalus polysaccharide enhanced antitumor effects of Apatinib in gastric cancer AGS cells by inhibiting AKT signalling pathway. Biomed Pharmacother. 2018; 100: 176–183, doi: 10.1016/j.biopha.2018.01.140, indexed in Pubmed: 29428665.

18. Liu T, Zhang M, Niu H, et al. Astragalus polysaccharide from Astragalus Melittin ameliorates inflammation via suppressing the activation of TLR-4/NF-κB p65 signal pathway and protects mice from CVB3-induced virus myocarditis. Int J Biol Macromol. 2019; 126: 179–186, doi: 10.1016/j.ijbiomac.2018.12.207, indexed in Pubmed: 30586589.

19. Zheng Y, Ren W, Zhang L, et al. A review of the pharmacological action of Astragalus polysaccharide. Front Pharmacol. 2020; 11: 349, doi: 10.3389/fphar.2020.00349, indexed in Pubmed: 32265719.

20. Chen M, May BH, Zhou IW, et al. Oxaliplatin-based chemotherapy combined with traditional medicines for neutropenia in colorectal cancer: A meta-analysis of the contributions of specific plants. Crit Rev Oncol Hematol. 2016; 105: 18–34, doi: 10.1016/j.critrevonc.2016.07.002, indexed in Pubmed: 27497028.

21. Zhang PP, Meng ZT, Wang LC, et al. Astragalus polysaccharide promotes the release of mature granulocytes through the L-selectin signaling pathway. Chin Med. 2015; 10: 17, doi: 10.1186/s13020-015-0043-z, indexed in Pubmed: 26161135.

22. Zhang LY, Yong WX, Wang L, et al. Astragalus polysaccharide eases G1 phase-correlative bystander effects through mediation of TGF- R/MAPK/ROS signal pathway after carbon ion irradiation in BMSCs. Am J Chin Med. 2019; 47(3): 595–612, doi: 10.1142/S0192415X19500319, indexed in Pubmed: 31122040.

23. Yang F, Yan G, Li Y, et al. Astragalus polysaccharide attenuated iron overload-induced dysfunction of mesenchymal stem cells via suppressing mitochondrial ROS. Cell Physiol Biochem. 2016; 39(4): 1369–1379, doi: 10.1159/000447841, indexed in Pubmed: 27607448.

24. Liu Y, Li CM, Lu Z, et al. Studies on formation and repair of formaldehyde-damaged DNA by detection of DNA-protein crosslinks and DNA breaks. Front Biosci. 2006; 11: 991–997, doi: 10.2741/1856, indexed in Pubmed: 16146790.

25. Formaldehyde, 2-butoxyethanol and 1-tert-butoxypropan-2-ol. IARC Monogr Eval Carcinog Risks Hum. 2006; 88: 1–478, indexed in Pubmed: 17366697.

26. Ji S, Thomforde J, Rogers C, et al. Transcriptional Bypass of DNA-Protein and DNA-Peptide Conjugates by T7 RNA Polymerase. ACS Chem Biol. 2019; 14(12): 2564–2575, doi: 10.1021/acschembio.9b00365, indexed in Pubmed: 31573793.

27. Ji S, Fu I, Naldiga S, et al. 5-Formylcytosine mediated DNA-protein cross-links block DNA replication and induce

28. mutations in human cells. Nucleic Acids Res. 2018; 46(13): 6455–6469, doi: 10.1093/nar/gky444, indexed in Pubmed: 29905846.

29. Permana PA, Snapka RM. Aldehyde-induced protein-DNA crosslinks disrupt specific stages of SV40 DNA replication. Carcinogenesis. 1994; 15(5): 1031–1036, doi: 10.1093/carcin/15.5.1031, indexed in Pubmed: 8200064.

30. Zhang L, Luo Y, Lu Z, et al. Astragalus polysaccharide inhibits ionizing radiation-induced bystander effects by regulating MAPK/NF-kB signaling pathway in bone mesenchymal stem cells (BMSCs). Med Sci Monit. 2018; 24: 4649–4658, doi: 10.12659/MSM.909153, indexed in Pubmed: 29976920.

31. Zhu J, Fu W, Jia W, et al. Association between NER pathway gene polymorphisms and wilms tumor risk. Mol Ther Nucleic Acids. 2018; 12: 854–860, doi: 10.1016/j.omtn.2018.08.002, indexed in Pubmed: 30161024.

32. Kojima Y, Machida YJ. DNA-protein crosslinks from environmental exposure: Mechanisms of formation and repair. Environ Mol Mutagen. 2020; 61(7): 716–729, doi: 10.1002/em.22381, indexed in Pubmed: 32329115.

33. Baker DJ, Wuenschell G, Xia L, et al. Nucleotide excision repair eliminates unique DNA-protein cross-links from mammalian cells. J Biol Chem. 2007; 282(31): 22592–22604, doi: 10.1074/jbc.M702856200, indexed in Pubmed: 17507378.

34. Buschta-Hedayat N, Buterin T, Hess MT, et al. Recognition of nonhybridizing base pairs during nucleotide excision repair of DNA. Proc Natl Acad Sci U S A. 1999; 96(11): 6090–6095, doi: 10.1073/pnas.96.11.6090, indexed in Pubmed: 10339546.

35. Wood R. DNA damage recognition during nucleotide excision repair in mammalian cells. Biochimie. 1999; 81(1-2): 39–44, doi: 10.1016/s0300-9084(99)80036-4, indexed in Pubmed: 10214908.

36. Yasuda G, Nishi R, Watanabe E, et al. In vivo destabilization and functional defects of the xeroderma pigmentosum C protein caused by a pathogenic missense mutation. Mol Cell Biol. 2007; 27(19): 6606–6614, doi: 10.1128/MCB.02166-06, indexed in Pubmed: 17682058.

37. Servant G, Streva VA, Derbes RS, et al. The nucleotide excision repair pathway limits L1 retrotransposition. Genetics. 2017; 205(1): 139–153, doi: 10.1534/genetics.116.188680, indexed in Pubmed: 28049704.

38. Sijbers A, Laat Wde, Ariza R, et al. Xeroderma pigmentosum group F caused by a defect in a structure-specific DNA repair endonuclease. Cell. 1996; 86(5): 811–822, doi: 10.1016/s0092-8674(00)80155-5, indexed in Pubmed: 8797827.

39. O'Donovan A, Davies AA, Moggs JG, et al. XPG endonuclease makes the 3' incision in human DNA nucleotide excision repair. Nature. 1994; 371(6496): 432–435, doi: 10.1038/371432a0, indexed in Pubmed: 8090225.

40. Cassee FR, de Burbure CY, Rambali B, et al. Subchronic inhalation of mixtures of cigarette smoke constituents in Xpa-/-p53+/- knock-out mice: a comparison of intermittent with semi-continuous exposure to acetaldehyde, formaldehyde, and acrolein. Food Chem Toxicol. 2008; 46(2): 527–536, doi: 10.1016/j.fct.2007.08.043, indexed in Pubmed: 17936466.

41. Saijo M, Kuraoka I, Masutani C, et al. Sequential binding of DNA repair proteins RPA and ERCC1 to XPA in vitro. Nucleic Acids Res. 1996; 24(23): 4719–4724, doi: 10.1093/nar/24.23.4719, indexed in Pubmed: 8972858.

42. Lindsey-Boltz LA, Kemp MG, Reardon JT, et al. Coupling of human DNA excision repair and the DNA damage checkpoint in a defined in vitro system. J Biol Chem. 2014; 289(8): 5074–5082, doi: 10.1074/jbc.M113.542787, indexed in Pubmed: 24403078.

42. Byrne BM, Oakley GG. Replication protein A, the laxative that keeps DNA regular: The importance of RPA phosphorylation in maintaining genome stability. Semin Cell Dev Biol. 2019; 86: 112–120, doi: 10.1016/j.semcdb.2018.04.005, indexed in Pubmed: 29665433.

43. Krasikova YS, Rechkunova NI, Maltseva EA, et al. Localization of xeroderma pigmentosum group A protein and replication protein A on damaged DNA in nucleotide excision repair. Nucleic Acids Res. 2010; 38(22): 8083–8094, doi: 10.1093/nar/gkq649, indexed in Pubmed: 20693538.

44. Krasikova YS, Rechkunova NI, Maltseva EA, et al. RPA and XPA interaction with DNA structures mimicking intermediates of the late stages in nucleotide excision repair. PLoS One. 2018; 13(1): e0190782, doi: 10.1371/journal.pone.0190782, indexed in Pubmed: 29320546.

ORIGINAL PAPER

**VIA MEDICA**

# Golgi $\alpha$-mannosidase II mediates the formation of vascular smooth muscle foam cells under inflammatory stress

## Kelan Zha#, Qiang Ye#

Department of Cardiology, The Affiliated Hospital of Southwest Medical University, Luzhou, China
#Both authors contributed equally to the manuscript and thus share the first authorship.

**Abstract**

**Introduction.** Vascular smooth muscle cells (VSMCs)-based foam cell formation is a crucial factor in the atherosclerosis process. We aimed to explore the mechanism of Golgi $\alpha$-mannosidase II (GMII) effects on the VSMCs-based foam cell formation.

**Material and methods.** VSMCs were exposed to different concentrations of low-density lipoproteins (LDLs), lipopolysaccharide (LPS), and/or GMII inhibitor (swainsonine). The qRT-PCR and western blot were used for expression analysis. Oil Red O staining was used to verify changes of lipid droplets in VSMCs. The translocation of the SCAP from the endoplasmic reticulum (ER) to Golgi was detected by immunofluorescence (IF).

**Results.** LPS disrupted the LDLs-mediated regulation of LDL receptor (LDLr) and increased intracellular cholesterol ester, which was inversely inhibited by swainsonine. The activity of $\alpha$-mannosidase II and GMII expression were decreased by LDLs but increased by the addition of LPS. Conversely, LPS-induced enhancement was reversed by swainsonine. Additionally, swainsonine reversed the LPS-induced increase of intracellular lipid droplets in the presence of LDLs. Expression analysis demonstrated that LDLr, SCAP, and SREBP2 were up-regulated by LPS, but reversed by swainsonine in LDLs-treated cells. IF staining revealed that swainsonine inhibited the translocation of SCAP to Golgi under inflammatory stress.

**Conclusions.** Collectively, swainsonine restrained LDLr expression to suppress the formation of VSMCs-based foam cells by reducing SREBP2 and SCAP under inflammatory stress conditions, suggesting that GMII contributes to the formation of VSMCs-based foam cells under inflammatory stress. *(Folia Histochemica et Cytobiologica 2021, Vol. 59, No. 2, 134–143)*

**Key words:** vascular smooth muscle cells; foam cells; LDLr; Golgi $\alpha$-mannosidase

## Introduction

Atherosclerosis is a chronic progressive inflammatory disease with high incidence and mortality, which

**Correspondence address:** Qiang Ye
Department of Cardiology, The Affiliated Hospital
of Southwest Medical University, No. 25,
Taiping Street, Jiangyang District,
Luzhou 646000, Sichuan, China
phone (0830)-3165120
fax: (0830)-2392753
e-mail: art006023@yeah.net
Co-authors' E-mail: Kelan Zha, 68069882@qq.com

is characterized by intimal accumulation of lipids (mainly cholesterol and cholesterol esters), the proliferation of vascular smooth muscle cells (VSMCs), and the infiltration of inflammatory cells in the wall of arteries [1, 2]. Particularly, VSMCs play a key role in atherogenesis by proliferating and migrating excessively in response to repeated injuries [3]. Foam cells, a special cell type located mainly in the intima of arteries [4], occur when lipid accumulation exceeds the cells' control mechanisms and is related to chronic inflammation in metabolic, infectious, and cardiovascular diseases (atherosclerosis, deep vein thrombosis, *etc.*) [5]. Foam cells play a significant role at all stages

of atherosclerotic lesion development, from initial lesions to advanced plaques [6]. In an early atherosclerotic lesion, the fatty streak appears on the arterial wall. With the progress of atherosclerosis, foam cells begin to release matrix-degrading enzymes, causing plaque rupture and blood vessel occlusion [7]. In pathological conditions, foam cells are derived from different cell types, including VSMCs and macrophages that originate from circulating monocytes [8].

Previous studies have focused on the accumulation of lipids in macrophages and vascular endothelial cells to form foam cells that deposit in the arterial wall. However, a limited number of studies focused on the role of VSMCs-based foam cells in the development of atherosclerosis. Recently, VSMCs were demonstrated to form foam cells after exposure to cholesterol or lipoproteins [9]. Notably, VSMCs-based foam cells account for about 45–90% of all foam cells [6]. Nevertheless, the mechanisms underlying the formation of VSMCs-based foam cells have not been explained.

It is widely accepted that the formation of foam cells is related to the dysregulation of intracellular cholesterol metabolism. Golgi $\alpha$-mannosidase II (GMII), sterol regulatory element-binding proteins (SREBPs), and SREBP cleavage-activating protein (SCAP) are important components of the intracellular cholesterol regulation system. GMII is a key glycosyl-hydrolase in the N-linked glycosylation pathway [10], which is required for SCAP glycosylation [11]. Additionally, SREBP2 is a transcription factor for the low-density lipoprotein (LDL) receptor (LDLr) gene, which is involved in cholesterol uptake [12]. SCAP can regulate the activity of SREBPs by adjusting their subcellular localization [13]. This feedback mechanism consisting of SCAP and SREBP2 can timely regulate intracellular cholesterol concentration under physiological conditions [14].

Inflammation participates in the pathophysiological process of atherosclerosis in many ways. Innate immune cells can secrete inflammatory mediators and promote the early stage of the atherosclerosis process [15]. Studies have shown that based on the pathophysiology of atherosclerosis, anti-inflammatory treatments are highly likely to be used to prevent atherosclerotic thrombosis [16].

Therefore, the present study aimed to investigate whether GMII affecting the VSMCs-based foam cells formation through the SCAP and SREBP2 pathway, so as to provide a new direction for the diagnosis and treatment of atherosclerosis. As consequence, the study preliminarily demonstrated that under *in vitro* conditions GMII contributes to the formation of VSMCs-based foam cells under inflammatory stress by promoting the translocation of SCAP complex from ER to Golgi, producing N-SREBP2 and eventually activating LDLr and lipid accumulation in VSMCs.

## Materials and methods

**Cell culture and treatments.** Human VSMCs from the coronary artery (TCS Cellworks, Buckingham, UK) were a gift from Professor X.Z. Ruan, University College London, London, England, UK. Human VSMCs were cultured in DMEM/F-12 (1:1) medium (Hyclone, Beijing, China), supplemented with 20% fetal bovine serum (FBS), 2 mmol/l glutamine, 100 U/ml penicillin, 100 $\mu$g/ml streptomycin under a humidified atmosphere at 37°C and 5% $CO_2$.

LDLs were isolated from the plasma of healthy human volunteers by sequential ultracentrifugation in the presence of 3 mmol/l EDTA, as previously described [17]. The plasma of healthy human volunteers was purchased from Luzhou Blood Center (Sichuan, China). After preparation of LDLs, cells were exposed to different concentrations of LDLs (25, 50, 100 and 200 $\mu$g/ml), lipopolysaccharide (LPS; 50, 100, 200, 400 ng/ml) and/or swainsonine (2.5, 5, and 7.5 $\mu$g/ml) according to the study design. LPS (from *Escherichia coli*, Cat. No. L4391) and swainsonine (Cat. No. 72741-87-8) were purchased from Sigma-Aldrich Corp. (Saint Louis, MO, USA). Cells exposed to DMEM/F-12 (1:1) medium were used as the control.

**Total RNA isolation and real-time quantitative polymerase chain reaction (qRT-PCR).** Total RNA was isolated from VSMCs using RNAiso kit (Takara, Dalian, China). Total RNA (1 mg), was used as a template for reverse transcription using Takara prime Script qRT-PCR Kit (Takara). qRT-PCR was performed in an ABI 7000 Sequence Detection System (Applied Biosystems, Waltham, MA, USA) using SYBR Green PCR Kit (Invitrogen, Carlsbad, CA, USA). GAPDH was used as an endogenous control to calculate the mRNA relative expression [18]. All the PCR primers were designed by Primer Express Software V2.0. PCR primer sequences were available in Table 1. The relative amount of mRNA was calculated using the comparative threshold cycle method.

**Measurement of intracellular cholesterol.** Treated cells were washed twice in phosphate-buffered saline (PBS); intracellular lipids were extracted in a chloroform/methanol (2:1) mix and dried under a vacuum. The total cholesterol, free cholesterol, and cholesterol ester content were measured by an enzymatic assay, as described previously [19], and normalized by total cell proteins determined by the Lowry assay (KeyGEN, Nanjing, China).

**Activity assay of $\alpha$-mannosidase.** The activity of $\alpha$-mannosidase was determined using an Alpha-Mannosidase Assay Kit (Cat: ab272519, Abcam, USA) according to the

**Table 1.** Primers used for qRT-PCR analysis

| Gene | Primer sequence (Forward) | Primer sequence (Reverse) |
|---|---|---|
| LDLr | 5'-GTGTCACAGCGGCGAATG-3' | 5'-CGCACTCTTTGATGGGTTCA-3' |
| SREBP2 | 5'-CCGCCTGTTCCGATGTACAC-3' | 5'-TGCACATTCAGCCAGGTTCA-3' |
| SCAP | 5'-GGGAACTTCTGGCAGAATGACT-3' | 5'-CTGGTGGATGGTCCCAATG-3' |
| $\beta$-actin | 5'-CCTGGCACCCAGCACAAT-3' | 5'-GCCGATCCACACACGGAGTACT-3' |

qRT-PCR — quantitative Reverse Transcription-Polymerase Chain Reaction

manufacturer's instruction. Briefly, the supernatant was firstly prepared from the homogenate of treated cells. Then, standards (100 $\mu$l) and samples (10 $\mu$l) were added into appropriate wells; subsequently, after adding the $\alpha$-mannosidase substrate, reaction mixes were incubated for 10 min at 25°C. The reaction was terminated with a stop reagent. The absorbance was detected at 405 nm. The $\alpha$-mannosidase activity was calculated using the formula: $\alpha$-mannosidase activity = $(OD_{sample} - OD_{blank})$/Slope (linear regression fit of the standard data points) × Dilution factor.

**Morphological examination by Oil Red O (ORO) staining.** Treated cells were firstly washed three times with PBS and then fixed with 5% formalin solution in PBS for 30 min. Subsequently, the fixed-cells were stained with ORO for 20 min and counterstained with hematoxylin for another 5 min. Finally, cell morphology was visualized under Olympus BX43 light microscope (Olympus, Tokyo, Japan).

**Protein isolation and Western blots analysis.** The cells were washed twice with PBS, placed at 4°C, and lysed for 10 min in lysis buffer. The concentration of protein was measured by bicinchoninic acid (BCA) (Solarbio, Beijing, China). After denaturation, the protein was electrophoresed on 8% SDS polyacrylamide gel in a Bio-Rad micro protein device (Bio-Rad, Hercules, CA, USA), then the membrane was transferred (100 V, 350 mA). After blocking with 5% skim milk, the following antibodies were diluted with antibody dilution buffer, and the protein strips were incubated at 4°C: rabbit anti-GMII antibody (Cat. No. ab224611, Abcam, Cambridge, UK), rabbit anti-LDLr antibody (1:1500, Cat. No. A00076-2, Boster, Wuhan, China), goat anti-SREBP2 antibody (1:1500, R&D Systems, Minneapolis, MN, USA), mouse anti-SCAP antibody (1:2000, Cat. No. sc-13553, Santa Cruz Biotechnology, Santa Cruz, CA, USA), and mouse anti-$\beta$-actin antibody (1:5000, Cat. No. A1978, SigmaAldrich). Rabbit anti-mouse (1:5000, Cat. No. sc-358914, Santa Cruz Biotechnology) or goat anti-rabbit HRP-labeled antibodies (1:5000, Cat. No. sc-2357, Santa Cruz Biotechnology) were used as the secondary antibodies correspondingly. Finally, detection procedures were performed using an ECL Advance TM western blotting detection kit, and autoradiography was performed on Hyperfilm TM ECL (Amersham Bioscience, Bucks, UK).

**Immunofluorescence (IF) staining.** The treated cells were fixed with 4% paraformaldehyde for 10 min and washed with PBS with 0.05% Tween-20 (SigmaAldrich) for 5 min. Then cells were permeabilized with 0.02% TritonX-100 (Solarbio) and blocked with goat serum (Solarbio) for 1 h. All the cells were incubated with rabbit anti-human SCAP antibody (1:100, Cat. No. ab190103, Abcam) and mouse anti-Golgi antibody (1:100, Cat. No. A-21270, Invitrogen) for 12 h at 4°C. After washing three times using PBS/Tween-20 over 30 min, cells were dual-stained with goat anti-rabbit IgG (H+L) highly cross-adsorbed secondary antibody, Alexa Fluor 488 (green) for SCAP (1:100, Cat. No. A-11034, Invitrogen) and goat anti-mouse IgG (H+L) highly cross-adsorbed secondary antibody, Alexa Fluor 594 (red) for Golgin (1:100, Cat. No. A-11032, Invitrogen) for 1 h at room temperature. Finally, cells were observed under a Leica TCS SP8 confocal microscope (Leica, Wetzlar, Germany).

**Statistical analysis.** Statistical analysis was performed with IBM SPSS statistics 17.0 (SPSS Inc., Chicago, IL, USA). All data were expressed as means ± standard deviation. Comparison between groups was performed with repeated-measures analysis of variance (ANOVA) followed by least-significant difference (LSD) *post-hoc* test. $p < 0.05$ was considered statistically significant.

## Results

### GMII inhibitor reverses the LPS-induced damage of LDLs-related LDLr negative feedback regulation

We investigated the impact of LPS-simulated inflammation on the negative feedback regulation of LDLr and choose the suitable concentration for the following experiments. We found that LDLs concentration at 25, 50, 100, 200 $\mu$g/ml significantly inhibited the expression of LDLr at the mRNA level (Fig. 1A, $p < 0.05$). LDLs at 25 $\mu$g/ml were sufficient to trigger negative feedback regulation, so the LDLs concentration used in this experiment was 25 $\mu$g/ml (Fig. 1A). Then, LPS was used to activate the inflammatory response. In the presence of LDLs (25 $\mu$g/ml), LDLr mRNA level was obviously up-regulated by LPS at 400 ng/ml ($p < 0.01$, Fig. 1B).
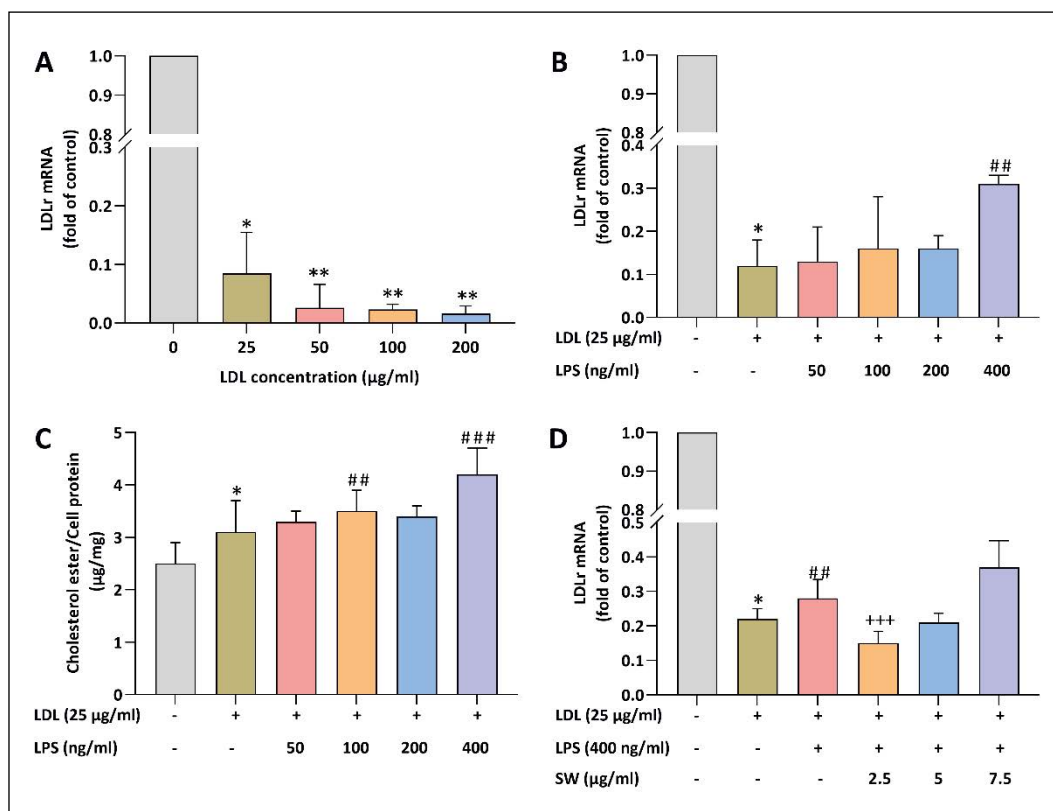
**Figure 1.** GMII inhibitor swainsonine reverses the LPS-induced damage of LDLs-related LDLr negative feedback regulation in cultured Vascular Smooth Muscle Cells (VSMCs). **A.** The optimal concentration of LDL triggering negative feedback regulation of LDLr. **B.** The optimal concentration of LPS that affected LDLr mRNA expression. **C.** The cholesterol ester content at optimal LDL concentration was affected by different concentrations of LPS. **D.** The optimal concentration of swainsonine that influenced LDLr mRNA expression. Data are expressed as means ± SD. *$p < 0.05$, **$p < 0.01$, and ***$p < 0.001$ *vs.* control; ##$p < 0.01$, ###$p < 0.001$ *vs.* LDL, +++$p < 0.001$ *vs.* LDL + LPS.

Then, we further verified the cholesterol ester content in VSMCs. Cholesterol ester content was increased by LPS at 400 ng/ml ($p < 0.001$), as shown in Figure 1C. Furthermore, in the presence of LDLs (25 μg/ml), swainsonine at a concentration of 2.5 μg/ml effectively reversed the up-regulation of LDLr mRNA mediated by LPS ($p < 0.001$, Fig. 1D). Taken together, based on the negative feedback regulation of LDLr, swainsonine could decrease the expression of LDLr under inflammatory stress conditions, indicating that GMII may be involved in foam cell formation. Moreover, the concentrations of LDLs, LPS, and swainsonine selected in the following experiments were 25 μg/ml, 400 ng/ml, and 2.5 μg/ml, respectively.

### Swainsonine inhibits the GMII up-regulation under inflammatory stress conditions
To explore whether GMII participates in the regulation of LDLr, we explored the expression of GMII under inflammatory agent, LPS, stimulation. As expected, LPS up-regulated the protein expression

of GMII in the presence of LDLs ($p < 0.01$, Fig. 2A). Moreover, LDLs decreased α-mannosidase activity ($p < 0.05$), but LPS reversed this effect and increased the α-mannosidase activity ($p < 0.01$). Meanwhile, the swainsonine decreased the activity of α-mannosidase ($p < 0.001$, Fig. 2B). Taken together, inflammation stress induced the up-regulation of GMII protein and GMII activity which was involved in the negative feedback regulation of LDLr expression.

### GMII inhibitor reduces cholesterol ester up-regulation under inflammatory stress conditions
Swainsonine, as an inhibitor of GMII, was used to further verify the relationship between the GMII and intracellular cholesterol ester. As shown in Figure 3A, compared with the control group, LDLs increased the number of lipid droplets in the VSMCs, which was further enhanced by LPS treatment. Moreover, swainsonine inhibited LPS-induced lipid droplet accumulation in VSCMs (Fig. 3A). Figure 3B showed that LDLs increased the cholesterol ester content
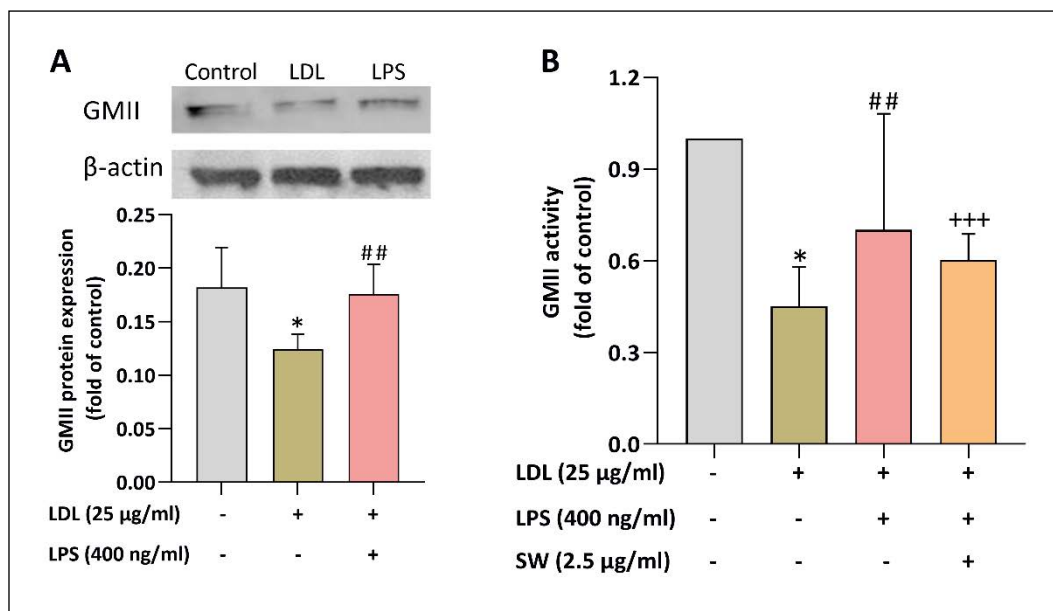
**Figure 2.** GMII inhibitor swainsonine inhibits the GMII up-regulation under inflammatory stress conditions in VSMCs. **A.** Effects of LDL and LPS on the expression of GMII were measured by Western blot. **B.** Effects of various treatments on GMII activity. Data are expressed as means ± SD. *$p < 0.05$ *vs*. control, ##$p < 0.01$ *vs*. LDL, +++$p < 0.001$ *vs*. LDL + LPS.
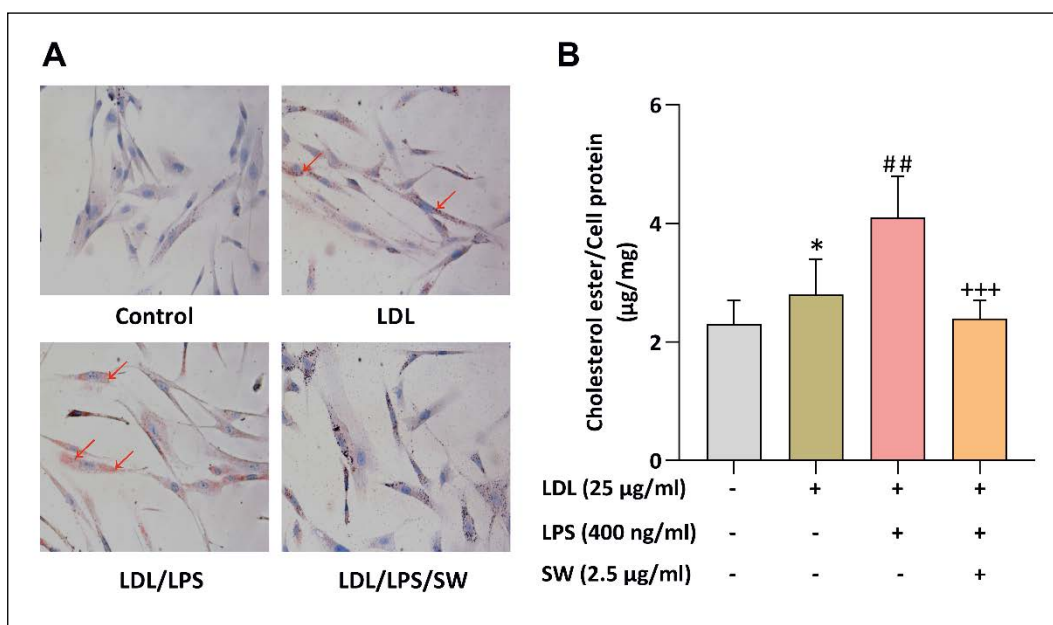


**Figure 3.** GMII inhibitor swainsonine reduces cholesterol ester up-regulation in the presence of LPS in VSMCs. **A.** Effects of various treatments on lipid droplets content (red arrow) were assessed by Oil Red O staining. **B.** Effects of various treatments on cholesterol ester content in VSMCs. Data are expressed as means ± SD. *$p < 0.05$ *vs*. control, ##$p < 0.01$ *vs*. LDL, +++$p < 0.001$ *vs*. LDL + LPS

($p < 0.05$); after LPS treatment, the cholesterol ester content was further increased ($p < 0.01$). After treatment with swainsonine, the content of cholesterol ester of VSMCs was decreased, despite LPS had augmented its level ($p < 0.001$). Thus, swainsonine reduced the level of intracellular cholesterol ester, indicating that GMII was involved in the accumulation of lipids.
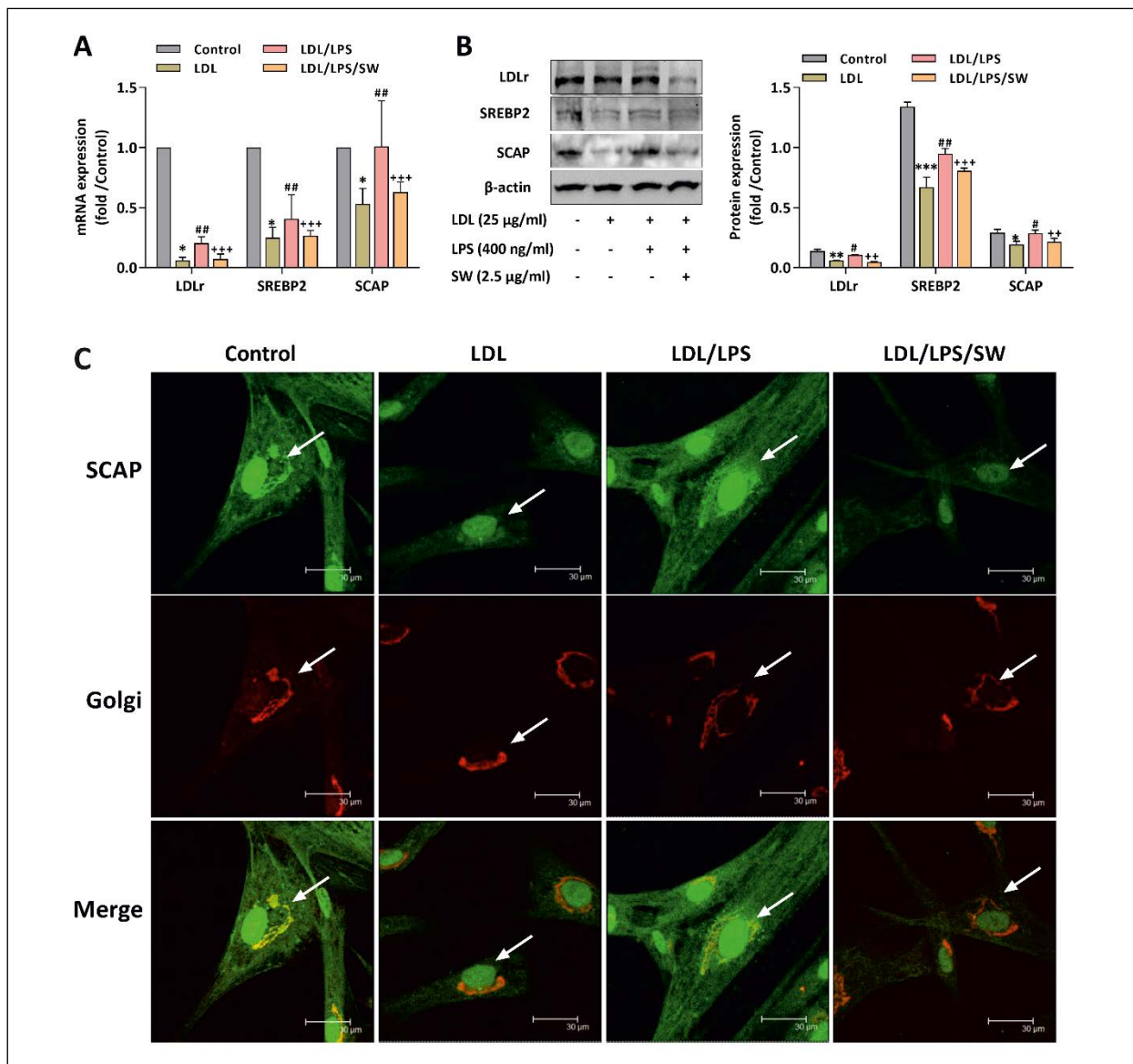
**Figure 4.** GMII inhibitor swainsonine decreases the expression of LDLr, SREBP2, and SCAP as well as the SCAP translocation under inflammatory stress conditions in VSMCs. **A.** Effects of various treatments on mRNA expression of LDLr, SREBP2, and SCAP were detected by qRT-PCR. **B.** Effects of various treatments on expression of LDLr, SREBP2, and SCAP proteins were verified by Western Blot. **C.** The translocation of the SCAP the endoplasmic reticulum to Golgi was evaluated by immunofluorescent staining. Data are expressed as means ± SD. $p < 0.05$ *vs.* control, **##**$p < 0.01$ *vs.* LDL, **+++**$p < 0.001$ *vs.* LDL + LPS

### GMII inhibitor decreases the expression of LDLr, SREBP2, and SCAP as well as the SCAP translocation under inflammatory stress conditions

We measured the expression of the LDLr negative feedback modulation-related proteins to explore the molecular mechanism of GMII regulation in VSMCs-based foam cells under inflammatory stress conditions. By the use of qRT-PCR, we found that LDLs inhibited the expression of LDLr, SCAP, and SREBP2 mRNAs ($p < 0.05$, Fig. 4A). Intriguingly, LPS increased mRNA levels of LDLr, SCAP, and SREBP2 in the presence of LDL ($p < 0.01$), overcoming the suppression induced by LDLs (Fig. 4A). Swainsonine reversed the LPS-induced up-regulation of LDLr, SCAP, and SREBP2 mRNA levels ($p < 0.001$), as shown in Fig. 4A. Western blot analysis demonstrated similar results to qRT-PCR measurements since swainsonine reversed the elevated protein levels of LDLr, SCAP, and SREBP2 induced by LPS ($p < 0.01$, Fig. 4B).

Furthermore, IF staining showed that LDLs inhibited the translocation of SCAP from ER to Golgi

in VSCMs; however, in the presence of LDLs, LPS increased the translocation of SCAP from ER to Golgi. It's worth noting that swainsonine reduced LPS-induced SCAP translocation (Fig. 4C). Taken together, swainsonine inhibited the expression of LDLr, SREBP2, and SCAP as well as the SCAP translocation in LDLs- and LPS-treated VSMCs, implying that GMII may contribute to the formation of VSMCs-based foam cells under inflammatory stress conditions, by up-regulating the SCAP expression, promoting SCAP translocation from ER to Golgi, activating SREBP2 and eventually activating LDLr negative feedback.

## Discussion

Studies over the past years demonstrated various mechanisms of atherosclerosis [20, 21], particularly the formation of foam cells due to an imbalance in intracellular lipid regulation. Furthermore, macrophage-derived foam cells have attracted extensive scholars' attention while VSMCs-derived foam cells got less noticed. Our study found that with the participation of inflammatory factors, GMII can activate the LDLr and promote lipid accumulation by the SREBP2-SCAP pathway to promote the formation of foam cells.

It has been established that the aggregation of LDLs is a primary cause of atherosclerosis [22]. LDLr expression is usually controlled by strict metabolic regulation in a negative feedback system that is dependent on intracellular cholesterol concentration [23]. When cells lack or contain more cholesterol than physiological needs, the up-regulation or down-regulation of 3-hydroxy-3-methylglutaryl-coenzyme-A reductase (HMGCoAR) and LDLr is respectively mediated through a negative feedback mechanism. It is closely controlled by two other proteins, SREBP2 and SREBP-SCAP, which are important for maintaining the balance of cholesterol in cells [24, 25]. As indicated in our study, the expression of LDLr mRNA was restrained by LDLs, suggesting that LDLs trigger negative feedback regulation of LDLr in VSMCs.

Inflammation is an all-important factor in the atherosclerotic process [26]. Inflammatory mediators, secreted by the immune cells, can lead to the early stage of the atherosclerotic process [27]. Some studies have announced that inflammatory cytokines can modify cholesterol-mediated LDLr regulation in mesangial cells, allowing unmodified LDLs accumulation in cells and causing foam cell formation [28, 29]. In our study, when LDLs were present, LPS disrupted the negative feedback regulation of LDLr. LPS increased the expression of LDLr at the mRNA

level and intracellular cholesterol ester content. Previously, studies have shown that intracellular cholesterol accumulation could obstruct mitochondrial function [30] and increase sensitivity to inflammation [31], thus affecting negative feedback regulation of LDLr [32, 33]. Ma *et al.* also reproted that inflammation increased lipid accumulation in VSMCs by disrupting LDLr feedback regulation [34], which further supports our present findings.

GMII, a key glycosyl-hydrolase in the N-linked glycosylation pathway, is an attractive target for inhibition with anti-inflammatory outcomes [10, 36]. It was reported to mediate the glycosylation of SCAP, which regulates cholesterol homeostasis through its interactions with SREBP-1 and -2 [14]. Accordingly, we have investigated whether and how GMII regulates the VSMCs-based foam cell formation by affecting regulation of cholesterol homeostasis. Firstly, we found that LDLs reduced the expression of GMII at the protein level and inhibited the activity of GMII, and that LPS reversed the effect caused by LDLs. Consisting with our results, the exposure of THP-1 macrophages to inflammatory cytokines upregulated the expression of GMII in the presence of LDLs [37]. This evidence implied the participation of GMII in cholesterol metabolism.

Given that foam cell formation is directly related to intracellular cholesterol accumulation [39], swainsonine, a potent inhibitor of GMII, was used for verifying the role of GMII in cholesterol regulation. As expected, swainsonine reversed the LPS-induced increase of intracellular cholesterol content and GMII activity, which suggested that GMII was indeed involved in cholesterol metabolism regulation in some way. In addition, intracellular lipid droplets distribution is an intuitive method to observe lipid accumulation. We found that LDLs increased the number of lipid droplets in VSMCs, which was further enhanced by the LPS treatment. Moreover, swainsonine inhibited LPS-induced lipid droplet accumulation in VSCMs. Therefore, we concluded that GMII may participate in the process of foam cell formation by affecting lipid accumulation.

Subsequently, we investigated the possible mechanisms of GMII regulating foam cell formation by detecting the expression of proteins related to the feedback regulation of cholesterol metabolism. Results of both PCR and western blot showed that swainsonine inhibited the expression of LDLr, SREBP2, and SCAP proteins under inflammatory stress conditions. Mechanically, the feedback regulation of cholesterol metabolism is maintained by the release of SREBPs from cell membranes [42]. As previously reported, the SCAP-SREBP2 complex not only

controls cholesterol biosynthesis but also serves as a signaling hub integrating cholesterol metabolism with pro-inflammatory activity of macrophages [43]. When cells are deprived of intracellular cholesterol, SCAP transfers SREBP2 from the ER to the Golgi, where it is cleaved by two membrane-bound proteases [44]. At the same time, SCAP is glycosylated by the continuous action of GMI, GMII, and GlcNAc transferase I, and then recycled to ER [37]. Then, the N-terminal fragment of SREBP2 (N-SREBP2) is released from Golgi to the nucleus, and binds to sterol regulatory elements in HMGCoAR and LDLr promoters, eventually activating the transcription of genes required for lipid synthesis and uptake [37, 42, 44]. In states of intracellular cholesterol overload, the SCAP-SREBP2 complex remains in ER, and SREBP-2 cannot be processed by the protease in Golgi apparatus. Subsequently, LDLr and HMGCoAR expression were down-regulated and the intracellular cholesterol content was reduced [24]. Considering these evidence and results of our study, we propose a following potential functional mechanism for the VSMCs-based foam cell formation. Inflammatory stress can increase the activity of GMII, which promotes the expression of SCAP and SREBP2, and increases glycosylation of SCAP, as well as translocation of the SCAP from the ER to Golgi apparatus, thereby activating the LDLr expression, increasing cholesterol uptake, and leading to the VSMCs-based foam cell formation. As indicated by immunofluorescent staining, under the action of LDLs, LPS promoted the translocation of SCAP from ER to Golgi, whereas swainsonine inhibited the LPS-induced SCAP translocation to Golgi, which further supported the above mechanism. Similar to our findings, Zhou *et al*. recently reported that the increased activity of GMII promoted complex-type conversion of SCAP N-glycans, which in turn mediated SREBP2 activation, and thereby led to intracellular cholesterol accumulation and foam cell formation in cultured VSMCs [45]. SREBP1, which belongs to the SREBP family with two isoforms (SREBP1-a and SREBP1-c), is another important transcriptional regulator of lipogenesis [46]. SREBP1 could regulate fatty acid synthesis, cholesterol synthesis, and cholesterol uptake [47]. SREBP1, as an inactive precursor, also forms a complex with SCAP (SCAP-SREBP1) in the ER membrane [48]. Consisting with the SCAP-SREBP2 complex, the SCAP-SREBP1 complex is also regulated by the concentration of sterols to activate the transcription of lipogenic genes [49]. Overall, GMII may contribute to the formation of foam cells by promoting the SCAP-SREBPs complex formation and activating LDLr in VSMSc. Unfortunately, in the present study, the expression of SREBP1 was not directly assessed; thus, in further studies, this proposed potential mechanism needs to be verified.

In summary, we demonstrated that LPS-simulated inflammation increased the expression of SREBP2 and SCAP by increasing the expression of GMII. GMII further promoted the translocation of the SCAP complex from ER to Golgi, producing more N-SREBP2. Finally, LDLr was activated by N-SREBP2 and promoted lipid accumulation in VSMCs. These processes together mediated the formation of foam cells. Our research provides a new direction and understanding of the molecular mechanism of atherosclerosis and further provides a new entry point for exploring novel therapeutic strategies.

## Acknowledgements

## Funding

## Author contributions
KZ and QY designed the study, collected and analyzed the data. KZ drafted the manuscript. QY critically reviewed the manuscript. All authors approved the final manuscript.

## Data availability statement
The data that support the findings of this study are available from the corresponding author, QY, upon reasonable request.

## Experimental ethics
Not applicable.

## Conflict of interest
The authors declare that they have no conflict of interest.

## References

1. Ye Q, Chen Y, Lei H, et al. Inflammatory stress increases unmodified LDL uptake via LDL receptor: an alternative pathway for macrophage foam-cell formation. Inflamm Res. 2009; 58(11): 809–818, doi: 10.1007/s00011-009-0052-4, indexed in Pubmed: 19533020.
2. Tall AR, Yvan-Charvet L. Cholesterol, inflammation and innate immunity. Nat Rev Immunol. 2015; 15(2): 104–116, doi: 10.1038/nri3793, indexed in Pubmed: 25614320.
3. Durham AL, Speer MY, Scatena M, et al. Role of smooth muscle cells in vascular calcification: implications in atherosclerosis and arterial stiffness. Cardiovasc Res. 2018; 114(4): 590–600, doi: 10.1093/cvr/cvy010, indexed in Pubmed: 29514202.
4. Yu XH, Fu YC, Zhang DW, et al. Foam cells in atherosclerosis. Clin Chim Acta. 2013; 424: 245–252, doi: 10.1016/j.cca.2013.06.006, indexed in Pubmed: 23782937.

5. Guerrini V, Gennaro ML. Foam Cells: One Size Doesn't Fit All. Trends Immunol. 2019; 40(12): 1163–1179, doi: 10.1016/j.it.2019.10.002, indexed in Pubmed: 31732284.

6. Chistiakov DA, Melnichenko AA, Myasoedova VA, et al. Mechanisms of foam cell formation in atherosclerosis. J Mol Med (Berl). 2017; 95(11): 1153–1165, doi: 10.1007/s00109-017-1575-8, indexed in Pubmed: 28785870.

7. Maguire EM, Pearce SWA, Xiao Q. Foam cell formation: A new target for fighting atherosclerosis and cardiovascular disease. Vascul Pharmacol. 2019; 112: 54–71, doi: 10.1016/j.vph.2018.08.002, indexed in Pubmed: 30115528.

8. Bobryshev YV, Lord RS, Golovanova NK, et al. Phenotype determination of anti-GM3 positive cells in atherosclerotic lesions of the human aorta. Hypothetical role of ganglioside GM3 in foam cell formation. Biochim Biophys Acta. 2001; 1535(2): 87–99, doi: 10.1016/s0925-4439(00)00076-4, indexed in Pubmed: 11341997.

9. Dubland JA, Francis GA. So Much Cholesterol: the unrecognized importance of smooth muscle cells in atherosclerotic foam cell formation. Curr Opin Lipidol. 2016; 27(2): 155–161, doi: 10.1097/MOL.0000000000000279, indexed in Pubmed: 26836481.

10. Shah N, Kuntz DA, Rose DR. Golgi alpha-mannosidase II cleaves two sugars sequentially in the same catalytic site. Proc Natl Acad Sci U S A. 2008; 105(28): 9570–9575, doi: 10.1073/pnas.0802206105, indexed in Pubmed: 18599462.

11. Dunphy WG, Brands R, Rothman JE. Attachment of terminal N-acetylglucosamine to asparagine-linked oligosaccharides occurs in central cisternae of the Golgi stack. Cell. 1985; 40(2): 463–472, doi: 10.1016/0092-8674(85)90161-8, indexed in Pubmed: 3155653.

12. Horton JD, Goldstein JL, Brown MS. SREBPs: activators of the complete program of cholesterol and fatty acid synthesis in the liver. J Clin Invest. 2002; 109(9): 1125–1131, doi: 10.1172/JCI15593, indexed in Pubmed: 11994399.

13. Nohturfft A, Yabe D, Goldstein JL, et al. Regulated step in cholesterol feedback localized to budding of SCAP from ER membranes. Cell. 2000; 102(3): 315–323, doi: 10.1016/s0092-8674(00)00037-4, indexed in Pubmed: 10975522.

14. Yuan Y, Zhao L, Chen Y, et al. Advanced glycation end products (AGEs) increase human mesangial foam cell formation by increasing Golgi SCAP glycosylation in vitro. Am J Physiol Renal Physiol. 2011; 301(1): F236–F243, doi: 10.1152/ajprenal.00646.2010, indexed in Pubmed: 21511699.

15. Karasawa T, Takahashi M. Role of NLRP3 Inflammasomes in Atherosclerosis. J Atheroscler Thromb. 2017; 24(5): 443–451, doi: 10.5551/jat.RV17001, indexed in Pubmed: 28260724.

16. Geovanini GR, Libby P. Atherosclerosis and inflammation: overview and updates. Clin Sci (Lond). 2018; 132(12): 1243–1252, doi: 10.1042/CS20180306, indexed in Pubmed: 29930142.

17. Li J, Huang M, Teoh H, et al. Panax quinquefolium saponins protects low density lipoproteins from oxidation. Life Sci. 1999; 64(1): 53–62, doi: 10.1016/s0024-3205(98)00533-5, indexed in Pubmed: 10027742.

18. Barber RD, Harmer DW, Coleman RA, et al. GAPDH as a housekeeping gene: analysis of GAPDH mRNA expression in a panel of 72 human tissues. Physiol Genomics. 2005; 21(3): 389–395, doi: 10.1152/physiolgenomics.00025.2005, indexed in Pubmed: 15769908.

19. Gamble W, Vaughan M, Kruth HS, et al. Procedure for determination of free and total cholesterol in micro- or nanogram amounts suitable for studies with cultured cells. J Lipid Res. 1978; 19(8): 1068–1070, doi: https://doi.org/10.1016/S0022-2275(20)40693-5., indexed in Pubmed: 731127.

20. Wang R, Wu W, Li W, et al. Activation of NLRP3 Inflammasome Promotes Foam Cell Formation in Vascular Smooth Muscle Cells and Atherogenesis Via HMGB1. J Am Heart Assoc. 2018; 7(19): e008596, doi: 10.1161/JAHA.118.008596, indexed in Pubmed: 30371306.

21. Chistiakov DA, Bobryshev YV, Orekhov AN. Macrophage-mediated cholesterol handling in atherosclerosis. J Cell Mol Med. 2016; 20(1): 17–28, doi: 10.1111/jcmm.12689, indexed in Pubmed: 26493158.

22. Ye Q, Lei H, Fan Z, et al. Difference in LDL receptor feedback regulation in macrophages and vascular smooth muscle cells: foam cell transformation under inflammatory stress. Inflammation. 2014; 37(2): 555–565, doi: 10.1007/s10753-013-9769-x, indexed in Pubmed: 24297394.

23. Kartawijaya M, Han HW, Kim Y, et al. Genistein upregulates LDLR levels via JNK-mediated activation of SREBP-2. Food Nutr Res. 2016; 60: 31120, doi: 10.3402/fnr.v60.31120, indexed in Pubmed: 27211318.

24. Jiang X, Yu J, Wang X, et al. Quercetin improves lipid metabolism via SCAP-SREBP2-LDLr signaling pathway in early stage diabetic nephropathy. Diabetes Metab Syndr Obes. 2019; 12: 827–839, doi: 10.2147/DMSO.S195456, indexed in Pubmed: 31239739.

25. Huang M, Zhao Z, Cao Q, et al. PAQR3 modulates blood cholesterol level by facilitating interaction between LDLR and PCSK9. Metabolism. 2019; 94: 88–95, doi: 10.1016/j.metabol.2019.02.005, indexed in Pubmed: 30831144.

26. Ronsein GE, Vaisar T. Inflammation, remodeling, and other factors affecting HDL cholesterol efflux. Curr Opin Lipidol. 2017; 28(1): 52–59, doi: 10.1097/MOL.0000000000000382, indexed in Pubmed: 27906712.

27. Catapano AL, Pirillo A, Norata GD. Vascular inflammation and low-density lipoproteins: is cholesterol the link? A lesson from the clinical trials. Br J Pharmacol. 2017; 174(22): 3973–3985, doi: 10.1111/bph.13805, indexed in Pubmed: 28369752.

28. Ruan XZ, Varghese Z, Powis SH, et al. Dysregulation of LDL receptor under the influence of inflammatory cytokines: a new pathway for foam cell formation. Kidney Int. 2001; 60(5): 1716–1725, doi: 10.1046/j.1523-1755.2001.00025.x, indexed in Pubmed: 11703589.

29. Zhong S, Zhao L, Li Q, et al. Inflammatory stress exacerbated mesangial foam cell formation and renal injury via disrupting cellular cholesterol homeostasis. Inflammation. 2015; 38(3): 959–971, doi: 10.1007/s10753-014-0058-0, indexed in Pubmed: 25387652.

30. Asalla S, Girada SB, Kuna RS, et al. Restoring mitochondrial function: a small molecule-mediated approach to enhance glucose stimulated insulin secretion in cholesterol accumulated pancreatic beta cells. Sci Rep. 2016; 6: 27513, doi: 10.1038/srep27513, indexed in Pubmed: 27282931.

31. Beloumi D, Blasco A, Muelas R, et al. Inflammatory correlated response in two lines of rabbit selected divergently for litter size environmental variability. Animals (Basel). 2020; 10(9), doi: 10.3390/ani10091540, indexed in Pubmed: 32882827.

32. Assini JM, Mulvihill EE, Sutherland BG, et al. Naringenin prevents cholesterol-induced systemic inflammation, metabolic dysregulation, and atherosclerosis in Ldlr−/− mice. J Lipid Res. 2013; 54(3): 711–724, doi: 10.1194/jlr.M032631, indexed in Pubmed: 23269394.

33. Zhang Y, Ma KL, Liu J, et al. Inflammatory stress exacerbates lipid accumulation and podocyte injuries in diabetic nephropathy. Acta Diabetol. 2015; 52(6): 1045–1056, doi: 10.1007/s00592-015-0753-9, indexed in Pubmed: 25896009.

34. Ma KL, Liu J, Wang CX, et al. Increased mTORC1 activity contributes to atherosclerosis in apolipoprotein E knockout

mice and in vascular smooth muscle cells. Int J Cardiol. 2013; 168(6): 5450–5453, doi: 10.1016/j.ijcard.2013.03.152, indexed in Pubmed: 23972959.

35. Hort MA, Straliotto MR, Netto PM, et al. Diphenyl diselenide effectively reduces atherosclerotic lesions in LDLr -/- mice by attenuation of oxidative stress and inflammation. J Cardiovasc Pharmacol. 2011; 58(1): 91–101, doi: 10.1097/FJC.0b013e31821d1149, indexed in Pubmed: 21558882.

36. Rose D. Structure, mechanism and inhibition of Golgi ǐ-mannosidase II. Curr Opin Struct Biol. 2012; 22(5): 558–562, doi: 10.1016/j.sbi.2012.06.005, indexed in Pubmed: 22819743.

37. Zhou C, Lei H, Chen Y, et al. Enhanced SCAP glycosylation by inflammation induces macrophage foam cell formation. PLoS One. 2013; 8(10): e75650, doi: 10.1371/journal.pone.0075650, indexed in Pubmed: 24146768.

38. Scott DW, Black LL, Vallejo MO, et al. Increased sensitivity of Apolipoprotein E knockout mice to swainsonine dependent immunomodulation. Immunobiology. 2014; 219(7): 497–502, doi: 10.1016/j.imbio.2014.02.011, indexed in Pubmed: 24674240.

39. Orekhov AN. LDL and foam cell formation as the basis of atherogenesis. Curr Opin Lipidol. 2018; 29(4): 279–284, doi: 10.1097/MOL.0000000000000525, indexed in Pubmed: 29746302.

40. Hu YW, Zhao JY, Li SF, et al. RP5-833A20.1/miR-382-5p/NFIA-dependent signal transduction pathway contributes to the regulation of cholesterol homeostasis and inflammatory reaction. Arterioscler Thromb Vasc Biol. 2015; 35(1): 87–101, doi: 10.1161/ATVBAHA.114.304296, indexed in Pubmed: 25265644.

41. Wang Bo, Rong X, Palladino END, et al. Phospholipid remodeling and cholesterol availability regulate intestinal stemness and tumorigenesis. Cell Stem Cell. 2018; 22(2): 206–220.e4, doi: 10.1016/j.stem.2017.12.017, indexed in Pubmed: 29395055.

42. Ye J, DeBose-Boyd RA. Regulation of cholesterol and fatty acid synthesis. Cold Spring Harb Perspect Biol. 2011; 3(7), doi: 10.1101/cshperspect.a004754, indexed in Pubmed: 21504873.

43. Guo C, Chi Z, Jiang D, et al. Cholesterol homeostatic regulator SCAP-SREBP2 integrates NLRP3 inflammasome activation and cholesterol biosynthetic signaling in macrophages.

Immunity. 2018; 49(5): 842–856.e7, doi: 10.1016/j.immuni.2018.08.021, indexed in Pubmed: 30366764.

44. Lee SH, Lee JH, Im SS. The cellular function of SCAP in metabolic signaling. Exp Mol Med. 2020; 52(5): 724–729, doi: 10.1038/s12276-020-0430-0, indexed in Pubmed: 32385422.

45. Zhou C, He Q, Gan H, et al. Hyperphosphatemia in chronic kidney disease exacerbates atherosclerosis via a mannosidases-mediated complex-type conversion of SCAP N-glycans. Kidney Int. 2021; 99(6): 1342–1353, doi: 10.1016/j.kint.2021.01.016, indexed in Pubmed: 33631226.

46. Xu Xu, So JS, Park JG, et al. Transcriptional control of hepatic lipid metabolism by SREBP and ChREBP. Semin Liver Dis. 2013; 33(4): 301–311, doi: 10.1055/s-0033-1358523, indexed in Pubmed: 24222088.

47. Ru P, Guo D. microRNA-29 mediates a novel negative feedback loop to regulate SCAP/SREBP-1 and lipid metabolism. RNA Dis. 2017; 4(1), doi: 10.14800/rd.1525, indexed in Pubmed: 28664184.

48. Han J, Li E, Chen L, et al. The CREB coactivator CRTC2 controls hepatic lipid metabolism by regulating SREBP1. Nature. 2015; 524(7564): 243–246, doi: 10.1038/nature14557, indexed in Pubmed: 26147081.

49. Lounis MA, Bergeron KF, Burhans MS, et al. Oleate activates SREBP-1 signaling activity in -deficient hepatocytes. Am J Physiol Endocrinol Metab. 2017; 313(6): E710–E720, doi: 10.1152/ajpendo.00151.2017, indexed in Pubmed: 28851735.

50. Zheng ZG, Zhu ST, Cheng HM, et al. Discovery of a potent SCAP degrader that ameliorates HFD-induced obesity, hyperlipidemia and insulin resistance via an autophagy-independent lysosomal pathway. Autophagy. 2020 [Epub ahead of print]: 1–22, doi: 10.1080/15548627.2020.1757955, indexed in Pubmed: 32432943.

51. Liu J, Zhang F, Li C, et al. Synergistic activation of human LDL receptor expression by SCAP ligand and cytokine oncostatin M. Arterioscler Thromb Vasc Biol. 2003; 23(1): 90–96, doi: 10.1161/01.atv.0000046229.77566.e5, indexed in Pubmed: 12524230.

52. Abidi P, Zhang F, Li C, et al. Blockage of the ERK signaling pathway abrogates the SCAP ligand-induced transcriptional activation of the LDL receptor gene in HepG2 cells. Int J Mol Med. 2005; 16(5): 779–785, indexed in Pubmed: 16211244.

# INSTRUCTIONS FOR AUTHORS

## MANUSCRPIT SUBMISSION

Folia Histochemica et Cytobiologica accepts manuscripts (original articles, short communications, review articles) from the field of histochemistry, as well as cell and tissue biology. Each manuscript is reviewed by independent referees. Book reviews and information concerning congresses, symposia, meetings etc., are also published.

All articles should be submitted to FHC electronically online at www.fhc.viamedica.pl where detailed instruction regarding submission process will be provided.

## AUTHOR'S STATEMENT

The manuscript must be accompanied by the author's statement that it has not been published (or submitted to publication) elsewhere.

## GHOSTWRITTING

Ghostwriting and guest-authorship are forbidden. In case of detecting ghost written manuscripts, their actions will be taking involving both the submitting authors and the participants involved.

The corresponding author must have obtained permission from all authors for the submission of each version of the paper and for any change in authorship. Submission of a paper that has not been approved by all authors may result in immediate rejection.

## COST OF PUBLICATION

The cost of publication of accepted manuscript is 800 Euro.

## OFFPRINTS

PDF file of each printed paper is supplied for the author free of charge. Orders for additional offprints should be sent to the Editorial Office together with galley proofs.

## ORGANIZATION OF MANUSCRIPT

The first page must include: the title, name(s) of author(s), affiliation(s), short running head (no more than 60 characters incl. spaces) and detailed address for correspondence including e-mail. Organization of the manuscript: 1. Abstract (not exceeding one typed page — should consist of the following sections: Introduction, Material and methods, Results, Conclusions); 2. Key words (max. 10); Introduction; Material and methods; Results; Discussion; Acknowledgements (if any); References; Tables (with legends); Figures; Legends to figures.

In a short communication, Results and Discussion should be written jointly. Organization of a review article is free.

## TECHNICAL REQUIREMENTS

Illustrations (line drawings and halftones) — either single or mounted in the form of plates, can be 85 mm, 125 mm, or 175 mm wide and cannot exceed the size of 175 × 250 mm. The authors are requested to plan their illustrations in such a way that the printed area is eco-nomically used. Numbers, inscriptions and abbreviations on the figures must be about 3 mm high. In case of micrographs, magnification (*e.g.* × 65 000) should be given in the legend. Calibration bars can also be used. For the best quality of illustrations please provide images in one of commonly used formats e.g. *.tiff, *.png, *pdf (preferred resolution 300 dpi). Tables should be numbered consecutively in Arabic numerals and each table must be typed on a separate page. The authors are requested to mark the places in the text, where a given table or figure should appear in print. Legends must begin on a new page and should be as concise as necessary for a self-sufficient explanation of the illustrations. PDF file of each paper is supplied free of charge.

## CITATIONS

In References section of article please use following American Medical Association 9th Ed. citation style. Note, that items are listed numerically in the order they are cited in the text, not alphabetically. If you are using a typewriter and cannot use italics, then use underlining.

**Authors:** use initials of first and second names with no spaces. Include up to six authors. If there are more than six, include the first three, followed by et al. If no author is given, start with the title. **Books:** include the edition statement (ex: 3rd ed. or Rev ed.) between the title and place if it is not the first edition. **Place:** use abbreviations of states, not postal codes. **Journals:** abbreviate titles as shown in *Index Medicus*. If the journal does not paginate continuously through the volume, include the month (and day). **Websites:** include the name of the webpage, the name of the entire website, the full date of the page (if available), and the date you looked at it. The rules concerning a title within a title are *not* displayed here for purposes of clarity. See the printed version of the manual for details. For documents and situations not listed here, see the printed version of the manual.

## EXAMPLES

**Book:**
1. Okuda M, Okuda D. *Star Trek Chronology: The History of the Future.* New York: Pocket Books; 1993.

**Journal or Magazine Article (with volume numbers):**
2. Redon J, Cifkova R, Laurent S et al. Mechanisms of hypertension in the cardiometabolic syndrome. *J Hypertens.* 2009; 27(3):441–451. doi: 10.1097/HJH.0b013e32831e13e5.

**Book Article or Chapter:**
3. James NE. Two sides of paradise: the Eden myth according to Kirk and Spock. In: Palumbo D, ed. *Spectrum of the Fantastic*. Westport, Conn: Greenwood; 1988:219–223.

When the manufacturers of the reagents etc. are mentioned for the first time, town, (state in the US) and country must be provided wheras for next referral only the name of the firm should be given.

**Website:**
4. Lynch T. DSN trials and tribble-ations review. Psi Phi: Bradley's Science Fiction Club Web site. 1996. Available at: http://www.bradley.edu/campusorg/psiphi/DS9/ep/503r.htm. Accessed October 8, 1997.

**Journal Article on the Internet:**
5. McCoy LH. Respiratory changes in Vulcans during pon farr. *J Extr Med* [serial online]. 1999;47:237–247. Available at: http://infotrac.galegroup.com/itweb/nysl_li_liu. Accessed April 7, 1999.